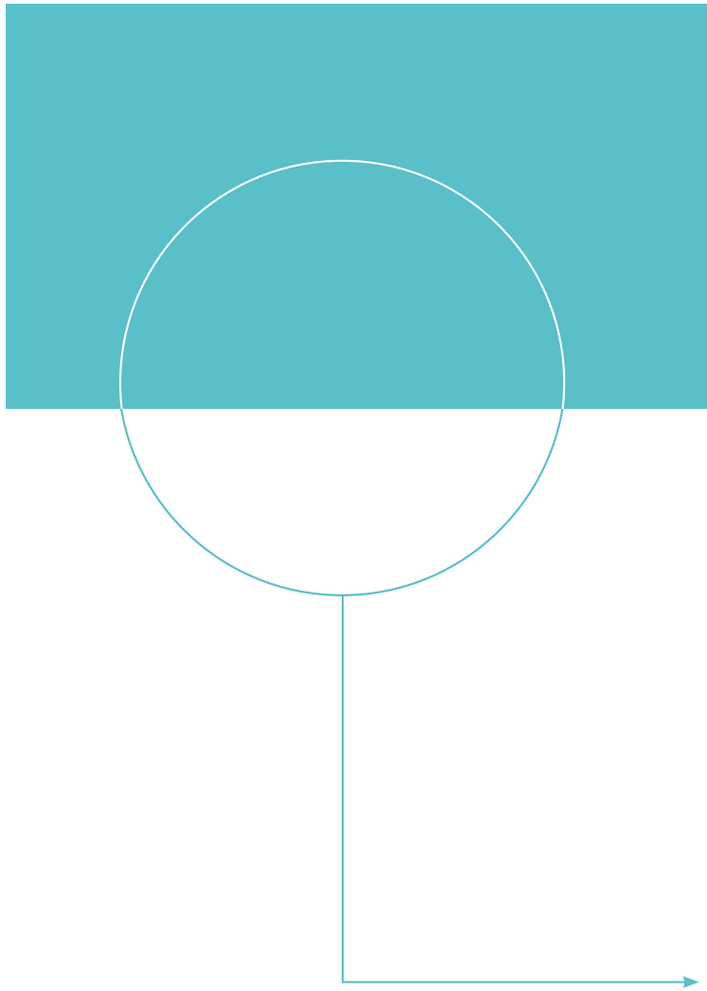

Master's thesis

2021

Joar Solvang

NTNU
Norwegian University of
Science and Technology
Faculty of Engineering
Department of Marine Technology

Joar Solvang

The development of a frequency-domain Multi-Unit Floating Platform model for design optimization.

August 2021

NTNU
Norwegian University of
Science and Technology

NTNU
Norwegian University of
Science and Technology

NTNU

Norwegian University of
Science and Technology

The development of a frequency-domain Multi-Unit Floating Platform model for design optimization.

Joar Solvang

European Wind Energy Master - Offshore Engineering
Submission date: August 2021
Supervisor: Erin Bachynski-Polić
Co-supervisor: Pim van der Male (TU Delft)

Norwegian University of Science and Technology
Department of Marine Technology

European Wind Energy Master

The development of a frequency-domain Multi-Unit Floating Platform model for design optimization.

Student Name:	Joar Solvang
Student number:	537165 (TU Delft), 5056209 (NTNU)
Project duration:	1st February, 2021 – 20th August, 2021
Thesis committee:	Prof. Dr. A. Metrikine, TU Delft,chair
	Dr. E. Bachynski-Polić NTNU, supervisor
	Dr. ir. P. van der Male, TU Delft, superviser

Faculty of Mechanical Engineering, Delft University of Technology

Faculty of Marine Technology, Norwegian University of Science and Technology

An electronic version of this thesis is available at http://repository.tudelft.nl.

August 13, 2021

TU Delft · NTNU

Contents

List of Figures

List of Tables

Nomenclature

Acronyms

COB Centre of Buoyancy

COM Centre of Mass

FEM Finite Element Model

LCOE Levelised Cost Of Energy

LIDAR Light Detection and Ranging

MPM Most Probably Maxima

MRS Multi-Rotor System

MUFP Multi-Unit Floating Platform

NREL National Renewable Energy Laboratory

PSD Power Spectral Density

RAO Response Amplitude Operator

RNA Rotor Nacelle Assembly

TSR Tip Speed Ratio

WEC Wave Energy Converter

Floater Dimension Symbols

$\hat{B}$ Damping Matrix

$\hat{K}$ Stiffness Matrix

$\hat{M}$ Mass Matrix

λ Slenderness

ϕ_{mass} Mass ratio between floater and ballast

ρ Density

COB_x x-coordinate of centre of buoyancy

COB_y y-coordinate of centre of buoyancy

COB_z z-coordinate of centre of buoyancy

D_c Column Diameter

D_h Heave plate diameter

F_{rated} Thrust force on nacelle at rated power.

H_f Floater height

H_h Heave plate height

h_{hub} Hub Height

I Second Moment of Inertia

I_{wp} Waterplane Moment of Inertia

K Effective Buckling Length

L_t Tower Length

L_{cf} Distance between CoM and front column, additional subscript x/y/z refers to axis

L_{cl} Distance between CoM and left column, additional subscript x/y/z refers to axis

L_{cr} Distance between CoM and right column, additional subscript x/y/z refers to axis

M Mass

M_b Total mass of floater ballast

M_f Total un-ballasted mass of system

$M_{b,back}$ Ballast mass in back column

$M_{b,front}$ Ballast mass in front column

$R_{in/out}$ Turbine tower radius at bottom

$r_{in/out}$ Turbine tower radius at top

t Thickness

V Volume

V_t Volume of tower

X_b x-coordinate of the ballast centre of mass

x_c X-axis column separation

X_f x-coordinate of the un-ballasted floaters centre of mass

y_c Y-axis column separation

H_{WX} Floater Displacement Transfer Function

r Radius

Spectra

$\mathrm{F}_w(\omega)$ Aerodynamic Thrust Force PSD

$\mathrm{M}_{w,Z}(\omega)$ Aerodynamic Moment PSD

$\mathrm{S}_{JS}(\omega)$ JONSWAP Spectrum

1 Abstract

The report summarises the development of a frequency domain Multi-Unit Floating Platform (MUFP) model and a parametric design optimization using the model. The model returns the response statistics of a MUFP due to environmental wind and wave loading using input variables of column separation, column diameter and draft. The model is developed with careful consideration to ensure compatibility with gradient-based optimizers. The low fidelity tool is capable of quickly traversing a design space to land on optimal substructure dimensions.

The program uses the input variables to calculate the geometry, buoyancy, mass and stiffness matrices of the MUFP. The design of a mooring system is considered outside the scope of this report. As a result, the stiffnesses in surge, sway and yaw are filled with placeholder stiffnesses.

The hydrodynamic coefficients of the three MUFP columns are calculated in HydroD. Smaller drag components such as bracing are assumed to be less influential and are therefore ignored. To maintain computational efficiency during the optimization, the hydrodynamic coefficients are interpolated using surrogate models.

The rated power of the MUFP is 10 MW, this is generated using two 5 MW turbines. The aerodynamic loading is accounted for by taking the Power Spectral Density (PSD) of a thrust force time series generated for the NREL 5 MW reference turbine in SIMA. The thrust force time series is taken as the sum of two individual SIMA simulations run in a 280m x 200m wind field.

The response statistics of the MUFP are calculated in the frequency domain. This is done by assuming the MUFP motion can be modelled by a Gaussian distribution. The Gaussian distribution is used to derive the zero-crossing periods and the expected number of cycles in a 3-hour timeseries. These values are used to calculate the probability of the maximum wave amplitude. The Most Probable Maxima (MPM) is then found by equating this probability to a Rayleigh distribution.

The MUFP is tested against two load cases at rated wind speeds. The first load case includes uni-directional head-on wind and wave loading. The second load case is designed to test the MUFP weathervaning properties. This is done by simulating head-on wind loading, a 90° wave heading and a 3° yaw misalignment.

The optimization is run using the SciPy SLSQP Minimize function. The objective function is the total steel mass and constraints are set on the static heave displacement in addition to the MPM pitch and roll rotations expected in a 3-hour timeseries. The optimization was run three times. Two solutions were found at the global minimum while the third was found at a less optimal local minimum.

A comparison of the MUFP optimized dimensions is made against a 10 MW WindFloat design. The comparison revealed the optimization solution was considerably smaller than the WindFloat. Although the physical properties of the MUFP do provide benefits such as a reduction in the aerodynamic pitching moment arm, it is concluded that the reduction in size is a result of the calculation process underestimating the MUFP response statistics.

2 Introduction

2.1 Offshore Wind Energy

The threat posed by climate change becomes increasingly apparent with every subsequent environmental record. As one of the major contributors to the crisis, it is clear that the energy sector must rapidly evolve to meet population needs through sustainable, decarbonised energy.

Wind energy has in the past decade shown itself to be a viable alternative to fossil fuels. Technological advancements in the field, exemplified by the dramatic increase in turbine power capacity shown in Figure 1, have driven wind energy into maturity offering investors safe and consistent returns on investment. As a result, the low carbon energy source has clocked an average compound annual growth rate of more than 21% since the beginning of the millennium [2].

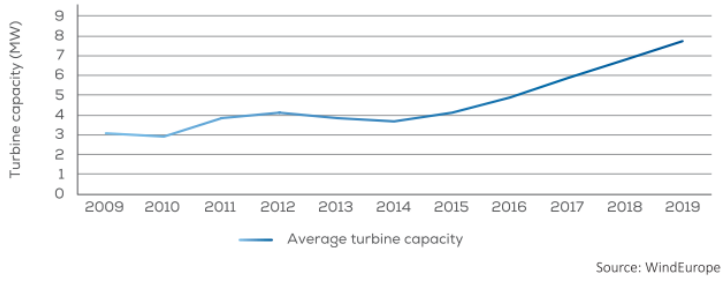

Figure 1: Yearly average of newly installed offshore wind turbine rated capacity.[1]

When the general population is presented with the facts regarding the climate crisis and the need for renewable energy, they respond positively to wind energy as a solution. Despite this, wind farm development often runs into difficulties when consulting local communities. The appearance and noise produced by wind turbines often strikes concern into parties regarding health, quality of life and property value. This so-called NIMBY-ism has become a sticking point for wind energy limiting its deployment in populated areas. [10]

In more recent years developers have been looking to the sea for the future of wind energy. Offshore projects can benefit from relatively close proximity to highly populated areas without inciting NIMBY-ism. The offshore environment also offers higher, more consistent wind speeds. This has allowed for the development of projects on the gigawatt scale. Ongoing developments include the 3.6 GW Dogger Bank wind farm of the cost off the United Kingdom and the 2.4 GW Empire Wind off the cost of New York.

Although the first offshore wind farm was built in Vindeby in 1991, the technology has only taken off in the past few years. In this short amount of time offshore wind energy has proved its potential and is predicted to grow significantly in the coming decades. Current predictions suggest a ten-fold increase in installed capacity from 2018 to 2030, growing between 23 GW to 228 GW [2].

Of the currently installed offshore wind farm capacity, 90% is built in the North Sea or nearby Atlantic Ocean [2]. The North Sea offers particularly favourable conditions, with excellent wind resource and large plots of shallow water. This has allowed businesses to

exploit experience from the Oil & Gas and/or Dredging industries to install fixed bottom wind turbines. A comparison of the currently deployed foundation types is shown in Figure 2. It is worth noting the only non-bottom fixed foundations are the spar, semi-sub and barge foundations.

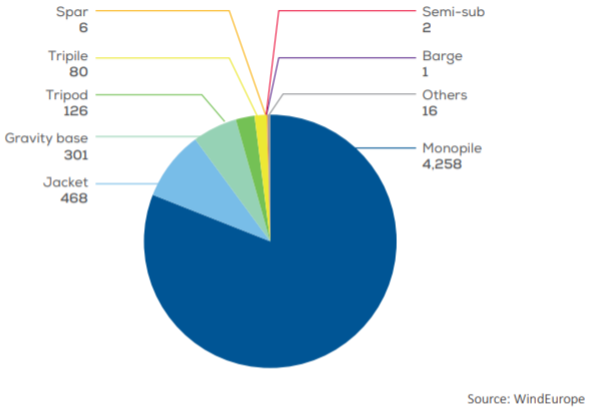

Figure 2: Application of foundation types in Europe's current installed capacity.[1]

As the total installed capacity has increased, developers have been forced to build and adapt designs to suit deeper water. The steady increase in average water depth over the past 20 years is shown in Figure 3. As water depths increase, the strain on design and inflation of cost begin to limit the profitability of a project.

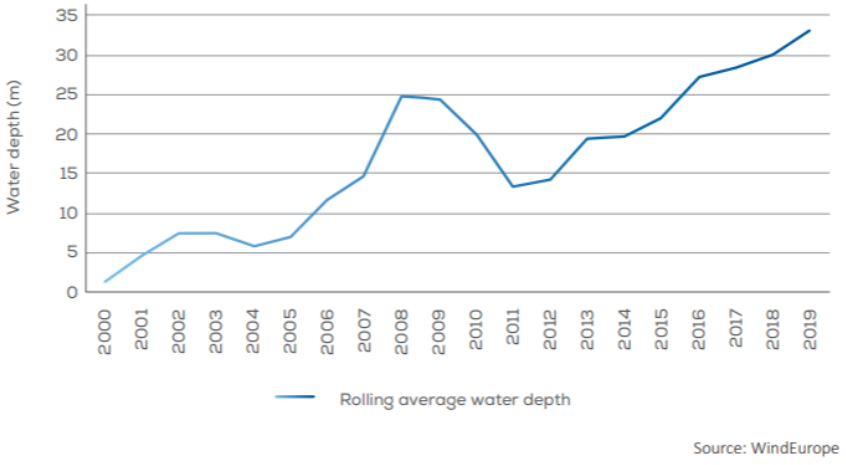

Figure 3: Rolling average water depth for offshore wind installation.[1]

A number of companies have begun exploring alternatives to fixed-bottom foundations and have begun prototyping floating foundations. These floating foundations are moored to the sea bottom and rely on hydrostatic stability to provide a foundation for the turbine. These platforms are being developed with the aim of opening the doors to deeper waters for the wind industry, paving the way to new markets and opportunities.

2.2 Floating Wind Concepts

Among the companies currently prototyping floating platforms are Equinor and Principle Power. In 2017, Equinor developed Hywind Scotland, the world's first floating wind farm off the coast of Scotland. The 30 MW project is supported by Equinor's spar type design and lies at a water depth of between 95m and 120m.

Principle Power are a US based company developing and prototyping their design, WindFloat. A full-scale 2 MW prototype was deployed 5km off the coast of Portugal in 2011 and decommissioned in 2016. Since then, the WindFloat platform has also been used on the WindFloat Atlantic project completed June 2020. The wind farm included the installation of three WindFloat platforms off the coast of Viana do Castelo, Portugal, with each platform supporting a 8.4 MW turbine. The WindFloat platform is also being installed on the 50 MW Kincardine offshore wind farm, which upon completion will become the largest operating floating wind farm in the world [13; 14].

Floating wind foundations can be characterised into three separate groups; Spar-buoy, Semi-submersible and Tension Leg Platforms. The three designs can be seen in Figure 4. The designs will be introduced briefly.

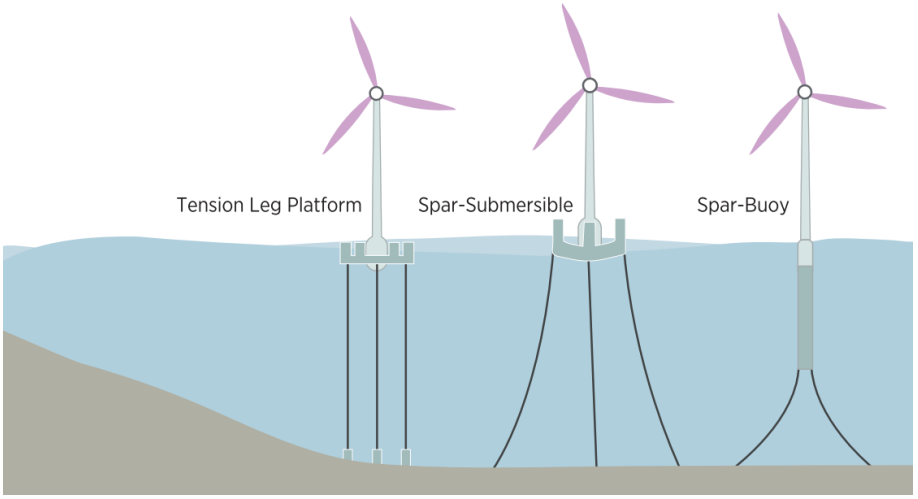

Figure 4: Info-graphic visualising the types of floating platforms.[2]

2.2.1 Spar Buoy

The Spar Buoy foundation consists of a large cylindrical column containing a heavy ballast at the bottom. The ballast causes the centre of gravity to fall far below the centre of buoyancy giving the platform the restoring forces necessary to maintain stability throughout operation [11]. The floater type requires a large draft for stability which can add difficulties in manufacturing and deployment. The Hywind Scotland wind farms spars had a 91m draft and a 14.5 m diameter [12]. This is a considerable length making it difficult to find suitable ports for required manufacturing, installation and maintenance operations.

2.2.2 Semi-Submersible

The semi-submersible design provides the necessary buoyancy and stability through a number of ballasted pontoons instead of the single column used by the spar buoy. The increased size of the platforms cross-sectional area allows for buoyancy to be obtained without the large draft. The inclusion of a moment arm between sources of buoyancy also improves the hydro-static restoring force against pitch which is of particular significance for wind turbines.

2.2.3 Tension Leg Platforms

Tension leg platforms are a tried-and-tested technology in the Oil & Gas industry. The designs were developed for drilling operations conducted in extremely deep water, typically over 1500m, where catenary mooring lines would incur excessive cost and weight. The buoyant semi-submersible platform is held stable by mooring the structure vertically to the seabed using steel tubes or tendons. The vertical mooring lines cause an uplifting force on the anchor requiring a more substantial anchoring system.

2.2.4 Floating Offshore Optimisation

The spar buoy and semi-submersible designs have so far been deemed successful and are nearing market maturity. Hywind Scotland has boasted an average capacity factor of 56% over its first two years of operation. To put this into perspective, the IRENA Future of Wind report predicting capacity factors of 58% being in the top 5% of projects in 2030 [3]. These promising results support the future of floating offshore wind energy.

There are currently a number of ongoing efforts to reduce the LCOE of offshore wind. An example is the utilisation of scale. As briefly mentioned earlier, ongoing construction of fixed bottom offshore wind farms are on the gigawatt scale. It can be expected that floating offshore wind farms will follow a similar explosion of size letting the technology benefit from quantities of scale.

Another design parameter being paid attention to is the mooring configuration. As floating offshore wind is built in deeper water, the mooring cost of the total project begins to take a more significant percentage. This is largely down to the increased length of mooring lines and additional difficulties in installing anchors. Therefore recent papers have begun to explore the opportunities in sharing mooring lines and anchors between turbines [15; 16].

In addition to this, impressive ideas have emerged looking to take advantage of the offshore environment. Naval architects have used weather vaning properties on floating production storage and offloading vessels to reduce unfavourable loading on ships [17]. This characteristic has been adopted by Eolink. Their platform design incorporates weather vaning in order to save cost on the yaw motor and bearing [18].

This weather vaning property has been taken a step further by concepts and companies such as W2Power, Hexicon AB and EnBW. By exploiting the passive trend to weather vane up against the wind, these designs position two turbines on a platform. As the platform weather vanes, these turbines will both be positioned perpendicularly to the wind, which allows for close positioning of turbines without suffering wake loses [4; 5; 19]. These platforms have been named Multi-Unit Floating Platforms (MUFP).

2.3 Multi-Unit Floating Offshore Wind

The Multiple Unit Floating Offshore Wind Farm (MUFOW) design was first mentioned in the Wind Engineering Journal by N. Barltop in 1993 [20]. Barltop theorised that a large offshore structure supporting multiple turbines would offer improved capsize stability, platform motion characteristics, maintenance interfaces and a reduction on installation costs per machine.

The potential offered by MUFOW in the wind industry is also supported by reviewing the scaling properties of wind energy with respect to rotor diameter. By assuming the turbine's tip speed ration (TSR) remains constant for turbines of increasing size, it is possible to review the scaling properties of power, thrust and stress.

It is known from 1-D momentum theory, which will be covered in Section 4.2.1, that the equations for power and thrust are given by Equation (2) and Equation (3) respectively. Given that the area of the turbine is circular, it can be seen that the turbine power output and thrust scale proportionally to r^2.

By assuming that the cost of a wind turbine is proportional to its mass, an approximation for the scaling properties of cost can also be derived. The mass of the structure can be expressed by Equation (4), where ρ_{eq} is an arbitrary wind turbine equivalent density and V is the volume of the structure. The volume can be said to be proportional to r^3. From this simplification it can be concluded that in theory, the cost of a turbine scales at a higher rate than that of power output. This implies that, based on the material cost per unit, there is no justification for building larger turbines.

$$TSR = \frac{R\omega}{U} \tag{1}$$

$$P = \frac{1}{2}\rho C_p A V^3 \implies P \propto r^2 \tag{2}$$

$$T = \frac{1}{2}\rho C_t A V^2 \implies T \propto r^2 \tag{3}$$

$$M = \rho_{eq} V \implies M \propto r^3 \tag{4}$$

Despite this, the trend followed by the industry has so far been in stark contrast. The costs imposed on a wind farm in the manufacturing, installation, maintenance and decommissioning stages of a project contradict the scaling approach outlined above. The cost saving made by opting for smaller turbines would immediately be lost through increased costs in installation time, vessel hire and increased operation and maintenance procedures. Therefore it has been seen as highly advantageous to maximise the power output of each individual turbine.

Another consideration is the structural and material advancements made in manufacturing the turbine blades. The manufacturers have been able to produce lighter, more durable blades which further nullifies the cost estimate approach used above. It is for this reason manufacturers such as Siemens Gamesa and GE have been able to expand turbines capacity to the 12 MW and 14 MW scale respectively.

Much like other technologies, the structural innovations will likely enter a period of diminishing returns. It has therefore been hypothesised that although the industry hasn't abided

by the law of scaling above, there is an optimum turbine capacity which once exceeded will stop being cost effective.

This optimum is where a MUFOW may begin to become favourable. By installing two turbines onto a single platform, a developer has the potential of increasing production and power density while making savings on foundation and mooring costs per unit.

2.4 Report Outline

On this basis there are grounds to further investigate the potential of MUFOW in offering the wind energy industry a path to further reducing the LCOE. This report will comprise the literature review into the state of MUFOW in addition to building and optimizing a MUFP model using gradient based techniques.

The optimization will focus on four variables. The column separation along the x and y axis, annotated x_c and y_c respectively, along with column diameter, D_c, and draft D_r. The optimization will aim to minimize the weight of the structure while maintaining appropriate operating conditions for the turbine. The model will be introduced in Section 5 and the optimization formulation in Section 8.

3 Literature Review

Limited literature investigating MUFOW has been published in recent years which does not reflect the current investment in industry. To capture the current interest in the design the literature review is split into academic papers and market research.

The literature review will be broken down into three areas of interest; multi-purpose offshore platforms, multi-rotor systems and structural considerations. The market research will follow W2Power, Hexicon AB and EnBW who are on the forefront of MUFOW development.

3.1 Academic

3.1.1 Multi-purpose offshore platforms.

A common point of interest amongst academics has been maximising the utilisation of offshore platforms. The cost of manufacturing, installing and maintaining large offshore wind farms is a significant expense and by integrating alternate sources of income into the design, the total return on investment can be increased.

Ambitions implementations of synergies are investigated by the EU funded "Modular Multi-use Deep Water Offshore Platform Harnessing and Servicing Mediterranean, Subtropical and Tropical Marine and Maritime Resources" (TROPOS) research project. The paper outlined the superior environment offered by installations in deep water to the aquaculture industry. It found that the distance to shore decreases pollutants and pathogens detrimental to the quality of aquaculture produce [21]. The paper investigates the so-called "Green & Blue" multi-use floating platform which integrates fish and algae aquaculture into the wind turbines platform. The research project highlighted the opportunity for joint logistics, shared infrastructure and maintenance services in order to drive down installation and operation costs relative to two independently run projects.

Other designs including hybrid renewable energy platforms incorporating both wind energy and wave energy converters have been presented. Wave energy is considered a more predictable source of energy with fewer fluctuations at low frequencies. The diversity in energy sources would therefore return a more stable energy output [22]. This is the basis for the W2Power design which will be introduced under market research. Other researchers have also conducted design and performance validation on the hybrid systems, concluding that the combination is economically feasible.

The dynamic impact of the hybrid designs have also been investigated. The TROPOS project found through experimental scale testing that the motion of the platform experienced additional damping and a longer natural period when incorporating a moon pool in the centre of a two turbine MUFP. The experimental test configuration is shown in Figure 5. The investigation highlights the need to consider the hybrid platforms holistically to capture all sources of excitation and damping which may become critical to the dynamic response of the system as a whole[21].

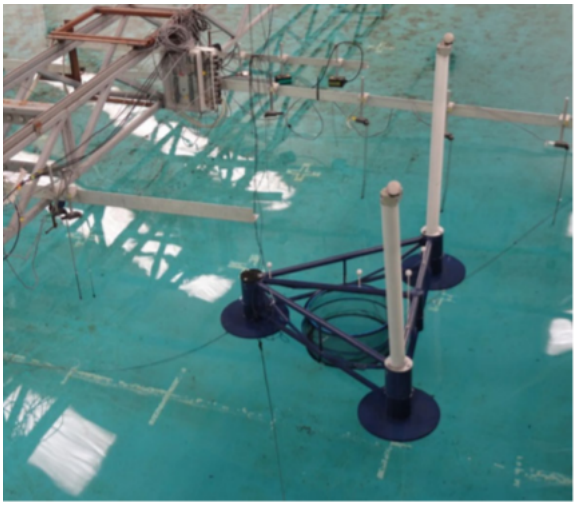

Figure 5: W2Power platform with fish cage installed [21].

Further studies into the dynamics response of a hybrid renewable energy platform are performed by Mayorga et al in 2018. A 15 MW capacity was designed on a platform consisting of two 6 MW turbines and 3 MW of wave energy converter capacity. The wind and wave energy components were designed separately in SeaFEM and calibrated against experimental test tank results. The paper found good alignment against the experimental data. The paper concluded that through development of an adequate control system, the WEC could act as a source of damping for the platform therefore reducing it's response in the heave direction [22].

The research topic is highly applicable to any large offshore development. The dimensions required to support two turbines is likely to be significant. Therefore, the combination of several income sources can pave a way to add economic competitiveness to MUFOW. The collaboration can also be seen as a pathway for other sources of renewable energy, such as wave energy converters, to gain technological maturity.

3.1.2 Multi-rotor systems

Another area of investigation among the academic community is multi-rotor systems. Multi-rotor systems, or MRS, are beneficial due to the scaling properties of wind outlined previously. Through means of standardisation it is possible to achieve the desired capacity for a lower cost using smaller but cheaper turbines. These rotors are placed on a single tower in close proximity of each other. The technique offers advantages over a single rotor however also impose complex interaction mechanisms between the rotors which have required investigation. An investigation into MRS was conducted by Vestas in collaboration with DTU. A front-facing diagram and an image taken from the test facility can be seen in Figure 6.

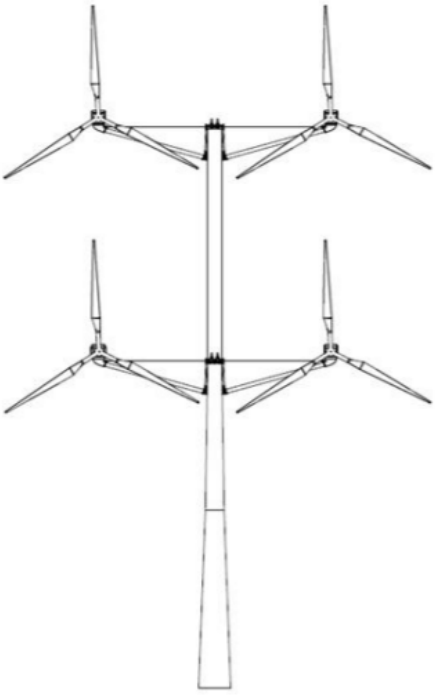

(a) Diagram of the Vestas MRS.[23]

(b) The MRS prototype by Vestas installed at Riso [24]

Figure 6: Multi-Rotor System diagrams.

The MRS demonstrator used four V29-225 kW nacelles mounted on a single frame. The demonstration collected vast amounts of data on each nacelle's response characteristics alongside detailed LIDAR measurements of wind response. The field measurements confirmed the overall power performance at below-rated wind speeds had improved by 1.8% ± 0.2% compared to a single rotor of equivalent area. The wake measurements recorded four distinct wakes in the near wake and a single merged wake in the far wake. The report found that the wake behind the MRS recovered at a distance of 1.03 to 1.44 D_{eq} less than that of a single rotor of equivalent diameter D_{eq}. These favourable results were in agreement with a wind tunnel test run on seven rotors installed on a hexagonal frame. There were no adverse effects on rotor performance with spacing between tips as low as 5% rotor diameter [24].

The additional cost savings of such a system are outlined in a comparison between a single 20 MW rotor and four 5 MW rotors made in "Multi-Rotors; A Solution to 20 MW and Beyond?" by Peter Jameson [25]. A 20 MW turbine was upscaled from a 5 MW turbine assuming any technological advancements made in the build up to a 20 MW turbine would also be applicable to a 5 MW turbine. The report concluded that four 5 MW turbines would cost approximately 80% of a single 20 MW turbine. [25].

These findings support the argument for the future of MUFOW. The improvements found in energy production and wake recovery could have dramatic improvements in the energy density yielded from an offshore wind farm. In addition to this, the cost savings in procuring

smaller turbines could leave developers requiring smaller CAPEX investment.

3.1.3 Structural and dynamic considerations.

The structural and dynamic response of a MUFP is the final topic covered by academic papers. The integrated dynamic response of a two-turbine system brings about additional sources of excitation, damping and complex internal coupling. A number of papers have also begun conducting design optimisations between steel reduction and the dynamic characteristics of a turbine.

A paper on the coupled dynamic analysis of multiple wind turbines on a single large floater by Y.H.Bae exemplified the additional internal coupling. A triangular three-turbine floater was designed in CHARM3D. The triangular platform had a large turbine placed at the front centre followed by two smaller turbines positioned diagonally behind. The forces acting on the three turbines were extrapolated from a FAST simulation run on a single turbine. The author simulated a blade fault in one of the turbines and found it had a significant impact on the side-to-side towerbase bending of another turbine. This report highlighted the importance of addressing the dynamic interaction effects between turbines through normal and fault conditions [26].

A parametric design study into tower inclinations was recently published with interesting results. The paper ran simulations on three turbines. The first was a standard platform with vertical turbine towers, the second had a shorter platform and a tower inclination of 8deg and the last comprised a even shorter platfrom with a tower inclination of 16 deg. A visualisation of the platforms used can be seen in Figure 7. The paper captured the hydrodynamic characteristics of each floater in WAMIT, before applying integrated analysis in OrcaFlex and Aerodyn. It was found that reducing the length of the platform while inclining the turbine towers outwards delivered favourable motion characteristics and concluded that an optimum tower inclination could be found [27].

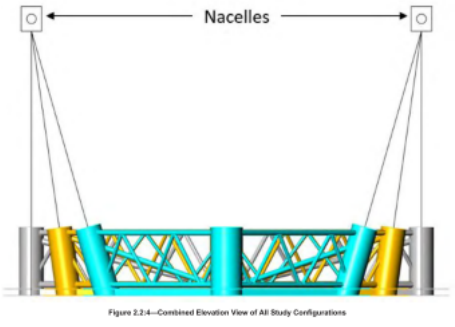

Figure 7: Combined elevation view of all study configurations [27].

A paper investigating the weather vaning property of a MUFP proposed a control system utilising the thrust curve of the turbines. The control system would adapt the tip speed, angle of attack and yaw of its turbine to force the turbine in a desired direction. The paper also concluded that, despite being successful, the system would likely incur additional fatigue damage in the turbine and tower by loading it in ways not initially accounted for by the manufacturer [28].

3.2 Industry

As mentioned, the lack of academic literature does not reflect the ambitions of industry players to secure patents on MUFP designs and the drive to push the floaters to technological maturity. A number of companies who have conducted scaled and full-scale prototype testing and/or are in the process of developing MUFP wind farms include W2Power, Hexicon AB and EnBW.

3.2.1 W2POWER

W2Power is a floating wind and wave power plant developed by the Norwegian company Pelagic Power founded in 2005. The W2Power design incorporates two counter rotating 3.6MW wind turbines and their patented wave energy converters (WEC) onto a semi-submersible. The design was first announced at All-Energy in 2009. Pelagic Power began collaborating with the Spanish marine engineering company EnerOcean the following year, who since 2010, have become the lead developer for the W2Power design [4].

Since then, the company underwent a period of design optimisation and tank testing pushing the design to a technological readiness level (TRL) of 5 by 2015. Following this in 2016, a prototype excluding the WEC was deployed at a 1:6 scale at the sea testing centre at PLOCAN. Since its decommissioning in 2019, the W2Power has become the first MUFP to reach testing in the open sea and the first to reach TRL6 [29]. A photo of the open sea prototype testing can be seen in Figure 8.

The scale testing received funding from the European Union's Horizon 2020 research and innovation programme under the name "Wind integrated platform for 10+ MW power per foundation" (WIP 10+). The results of the testing have delivered lessons learnt in commissioning the floating turbine in addition to returning valuable empirical data to update mathematical models. Lessons learnt on the wind vaning mooring system will also allow the Enerocean to make significant improvements in cost and performance [29].

Figure 8: W2Power prototype test of the coast of Spain. [29]

3.2.2 Hexicon A.B.

Hexicon A.B. are another company investing in the MUFP design. The Swedish company was founded in 2009 and have designed a floater similar to that of W2Power however without the WEC. The company have revealed a number of design improvements which include an incline tower and shorter platform length, the design can be seen in Figure 9. Since its inception, Hexicon A.B. have struck a number of partnership deals and development rights, however are yet to bring a project to fruition [5].

Figure 9: Hexicon AB MUFP design [5]

In 2016, the company applied for consent from local authorities to build a demonstration project located 6km of the coast of Dounreay on the North Coast on Scotland. The consent was approved a year later and a company, Dounreay Trì, was set up to oversee the development by Hexicon. The company shortly went into administration following financial difficulties and has since been on hold. As recently as 2018, Marcus Thor, a Hexicon Project Director had revealed to press their ambition of getting the project back on track. However, Hexicon has since entered a binding agreement to sell their majority interest in the Dounreay Trì project [5; 30; 32].

Despite this, the company have struck two further joint ventures with WunderSight, a renewable energy specialist, and COENS Co, Ltd., a specialist in servicing the oil and gas industry in South Korea. Wunder Hexicon Joint Venture are aiming to conduct a Feasibility Study on a demonstration project at the PLOCAN Testing Facility off the coast of Gran Canaria. The project intends to commission a full scale 10 MW platform mounted with two 5MW wind turbines. The project, named MULTIPLAT2, has received funding from EATIC [31]. The CoensHexicon joint venture has struck a large development agreement with Shell. The joint development venture will see the companies construct 200 MW large offshore 20 km off the city of Ulsan with deployment from 2022 [33].

3.2.3 EnBW: Nezzy^2

Nezzy^2 is the multi-unit floating concept developed by EnBW in collaboration with Aerodyn. The two-turbine platform consists of two towers stemming from the same point but leaning approximately 45deg to either direction. Each turbine is also attached to the platform with guy-wires. An image taken from its prototype testing can be seen in Figure 10.

Figure 10: Nezzy^2 prototype testing. [35]

A Nezzy^2 1:10 scaled prototype has so far undergone initial testing in a flooded gravel pit in Germany without wave loading. The tests were conducted to solely examine the influence of wind on the system. A second test operating in the Baltic sea is currently waiting approval from local authorities. The testing of a full-scale 15 MW model is scheduled to take place off the coast of Chine in late 2021 [34; 35].

3.2.4 Summary

The literature review has shown the opportunities opening to offshore wind as it explores deeper waters. Other industries such as aquaculture are positioned to benefit from the platforms, and by maximising utility, developers can improve their returns on investments. Creating multi-use platforms will cause knock-on effects on damping and natural frequencies which could be negative. MRS have been tried and tested on a number of occasions due to improved scaling properties and lower required investments. The tests have found improved power production and a reduced wake recovery time. MRS have so far not been represented on a commercial scale because they require more extensive maintenance, however the tests are indicative of the potential MRS will hold as the returns on nacelle and blade innovations begin to diminish. MUFP hold additional internal coupling which require research. The static and dynamic equilibrium is dependent on the normal operation of both turbines. The dependency between the turbines requires additional control systems to be developed. For example: in the occurrence of failure in one of the turbines, the imbalance in forces could lead to uneven moment on the platform causing it to displace undesirably.

There is an ongoing drive to develop MUFP in industry with a number of companies

investing heavily. It is clear that despite the early financial hurdles hit by Hexicon A.B., their ambitions have not been subdued. Interest from other companies and the backing of the oil giant Shell adds validity to the technology and its cost savings potential. The scaled and prototype testing by EnerOcean and EnBW seem to have returned successful results and the planning of a full scale 15 MW turbine by EnBW has promising indication on the designs approaching TRL9.

4 Theoretical Background

To analyse a aero-hydro multi-turbine floating platform model the DNVGL software suite is used. The results of this analysis can then be utilized in a gradient based optimization. A simplified model floater is constructed in GeniE, the models hydrodynamic parameters such as added mass are then found in HydroD before frequency domain analysis is conducted. The basic principles behind this software package are outlined below.

4.1 Foundation and Wave Loads

4.1.1 3D Potential Theory

The hydrodynamic analysis conducted in the software suite will for the most part use 3D potential flow. The principles behind the theory are that the flow is assumed to be non-viscous, in-compressible and homogeneous. Under these assumptions the continuity of the flow can be expressed as shown in Equation (5).

$$\frac{\partial u}{\partial x} + \frac{\partial u}{\partial y} + \frac{\partial u}{\partial z} = 0 \implies \nabla \cdot \vec{V} = 0 \tag{5}$$

By assuming zero vorticity, the Laplace equation is also satisfied, Equation (6). A solution to the Laplace equation can be found by applying relevant boundary conditions.

$$\frac{\partial^2 \phi}{\partial x^2} + \frac{\partial^2 \phi}{\partial y^2} = \Delta\phi = \nabla^2\phi = 0 \tag{6}$$

The applied boundary conditions are as follows. For a fixed body in moving fluid, Equation (7) is applied. The boundary condition states that the body surface is impermeable. Therefore the partial derivative of the velocity potential normal to the body surface (n) is equal to zero. If a point on a body is moving with velocity V_B, the boundary condition is set to Equation (8).

$$\frac{\partial \phi}{\partial n} = 0 \tag{7}$$

$$\frac{\partial \phi}{\partial n} = V_B \cdot n \tag{8}$$

The boundary condition set at the free surface is derived from Bernoulli's equation and can be derived from the kinematic boundary condition at $z = 0$ as shown in Equation (9), where z is defined as the free surface elevation, and the dynamic free-surface condition shown in Equation (10). The resulting equation is shown in Equation (11). A more complete derivation of the boundary conditions can be found in Sea Loads on Ships and Offshore Structures by O. M. Faltinsen [36].

$$\frac{\partial \zeta}{\partial t} = \frac{\partial \phi}{\partial z} \tag{9}$$

$$g\zeta + \frac{\partial \phi}{\partial t} = 0 \tag{10}$$

$$\frac{\partial^2 \zeta}{\partial t^2} + g\frac{\partial \phi}{\partial z} = 0 \tag{11}$$

4.1.2 Force & Equations of Motion

The floater's equation of motion stems from Newton's second law: force is equal to mass times acceleration. The source of loading on a floating structure is split up into different parts.

The model can be considered in two circumstances. The first is a situation in which the floater is fixed in its six degrees of freedom while subject to incoming wave loading. The resultant forces on the body are called wave excitation loads. The second situation to be considered is the body being forced to move in its six degrees of freedom through a body of water with no incident waves. The hydrodynamic loads are considered as the added mass, damping and restoring terms.

The velocity potential can then be described by Equation (12) where,ϕ_0, ϕ_D and ϕ_R are the incoming wave velocity potential, diffraction velocity potential and radiation velocity potential.

$$\phi(x, y, z, t) = \phi_0(x, y, z, t) + \phi_D(x, y, z, t) + \phi_R(x, y, z, t) \tag{12}$$

The external force can then be calculated by integrating these velocity potentials over the surface of the body. In addition to this, an extra term derived from Bernoulli's equation is included to account for static pressure. The resulting force equation can be seen in Equation (13). The subscript k denotes the respective degree of freedom.

$$F_{exc,k}(t) = \int_{s_{0,B}} \rho \frac{\partial \phi}{dt} n_k \, dS + \int_{s_{0,B}} -\rho g z n_k dS \qquad k = 1...6 \tag{13}$$

In the second loading case, the body is moved through the water causing out-going waves. The pressure experienced on the body's surface can be integrated over to find the resulting forces on the body. The added mass and damping coefficients can be found from Equation (14) where η is the body's movements in the degrees of freedom [36].

$$F = -A_{kj}\frac{d^2\eta_j}{dt^2} - B_{kj}\frac{d\eta_j}{dt} \tag{14}$$

The forces, added mass and damping terms are all frequency dependent. These calculations are therefore run for the full span of possible loading frequencies. In the context of this report, the above calculation process was run using the HydroD package.

4.2 Aerodynamics

The aerodynamic theory used in this report theory is summarised below, the derivations and theory follow the work presented in Aerodynamics of Wind Turbines [7].

4.2.1 1D Momentum Theory

1D Momentum theory is used to derive equations for a turbines power and thrust values as a function of its axial induction factor. The method simplifies the turbine to a one dimensional actuator disk. The simplified system can be seen in Figure 11. In addition to this a number of assumptions are made about the air flow:

- homogeneous, in-compressible, steady-state flow
- no frictional drag
- infinite number of blades
- uniform thrust over the disk
- non-rotating wake
- pressure jump at the rotor disk with continuous velocity across the rotor disk
- ambient pressure far away the disk.

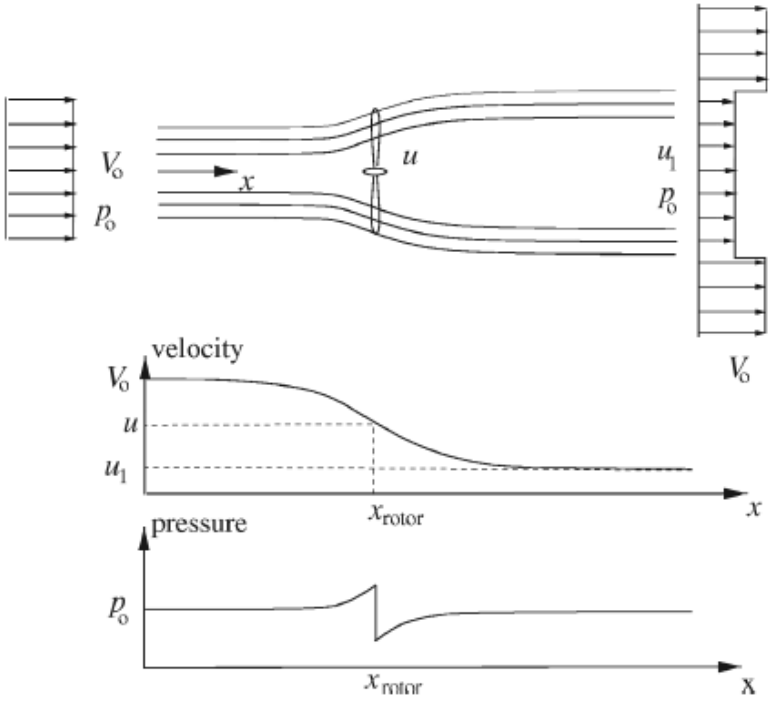

Figure 11: "Streamlines past the rotor and the axial velocity and pressure up- and downstream of the rotor" [7]

The theory assumes conservation of mass and momentum in the flow across the actuator disk. These assumptions are shown in Equations (15) and (16). The subscripts 0 and 1 represent the flow of air into and out of the flow stream respectively. Using these two

equations, Equation (17) can be derived, this expresses thrust as a function of the mass, in flow and outflow velocity.

$$\dot{m} = \rho A_0 v_0 = \rho A_1 v_1 \tag{15}$$
$$T = v_0(\rho A_0 v_0) - v_1(\rho A_1 v_1) \tag{16}$$
$$T = \dot{m}(v_0 - v_1) \tag{17}$$

The assumptions outlined above mean that Bernoulli's equations can be applied to either side of the actuator disk. Bernoulli's equation from the inflow velocity to the velocity immediately before the actuator disk can be seen in Equation (18), while the equation describing the flow of air from immediately behind the actuator disk to the outflow can be seen in Equation (19). Using these equations an expression for the pressure drop across the actuator disc can be found, Equation (20). Considering that thrust on the actuator disc can be described as pressure multiplied by area, another term for thrust can be found in Equation (21).

$$p_0 = \frac{1}{2}\rho v_0^2 = p_A + \frac{1}{2}\rho v_A^2 \tag{18}$$
$$p_B = \frac{1}{2}\rho v_B^2 = p_1 + \frac{1}{2}\rho v_B^2 \tag{19}$$
$$p_A - p_B = \frac{1}{2}\rho v_0^2 - \frac{1}{2}\rho v_1^2 \tag{20}$$
$$T = \frac{1}{2}\rho A(v_0^2 - v_1^2) \tag{21}$$

Combining the two equations for thrust an expression for the velocity before the actuator disk (v_a) can be derived as shown in Equation (22). The equation finds that the flow velocity immediately before the disk is an average of the inflow and outflow velocity.

$$v_a = \frac{1}{2}(v_1 - v_0) \tag{22}$$

Introducing the axial induction factor as shown in Equation (23) enables convenient expressions for the flow velocity at the disk and at the outflow as shown in Equations (24) and (25).

$$a = \frac{v_0 - v_a}{v_0} \tag{23}$$
$$v_A = v_0(1 - a) \tag{24}$$
$$v_1 = v_0(1 - 2a) \tag{25}$$

The power extracted can be derived from the change in kinetic energy between the inflow and outflow. Using this formulation along with the derived expressions for the flow velocity

at the disk and the outflow, namely Equations (24) and (25), the power equation Equation (28) can be derived as a function of the axial induction factor a. A similar process can be repeated for thrust, which obtains Equation (29) [7].

$$P = \frac{1}{2}\rho A v_A (v_0^2 - v_1^2) \tag{26}$$

$$P = \frac{1}{2}\rho A (v_0^2 - (v_0(1-2a))^2) v_0 (1-a)^2 \tag{27}$$

$$P = \frac{1}{2}\rho A v_0^3 4a(1-a)^2 \tag{28}$$

$$T = \frac{1}{2}\rho A V_0^2 4a(1-a) \tag{29}$$

4.2.2 Ideal turbine with wake rotation

The 1D momentum theory assumed a non-rotating wake. In reality the torque generated by the airfoils will cause a rotational velocity in the wake in the opposite direction. The power, thrust and torque exerted on a small annulus on the rotor can be calculated including the rotational wake.

Glauert proved Equation (30), expressing the pressure difference over the rotor as a function of the rotor angular velocity (Ω) and the wake angular velocity (ω).

$$p_B - p_A = \rho(\Omega + \frac{1}{2}\omega)\omega r^2 \tag{30}$$

By integrating the pressure drop over the area of an annulus of width dr, an expression for thrust exerted on the annulus can be found.

$$dT = \rho\left(\Omega + \frac{1}{2}\omega\right)\omega r^2 2\pi r dr \tag{31}$$

$$a' = \frac{\omega}{2\Omega} \tag{32}$$

$$dT = \frac{1}{2}\rho\Omega^2 4a'(1+a')r^2 2\pi r dr = 4a(1-a)\frac{1}{2}\rho v_0^2 2\pi r dr \tag{33}$$

An expression for torque on an rotor can be found from the change in angular momentum in the wake as shown in Equation (34). The incremental load on an annular area of the rotor can be found, as shown in Equation (35).

$$dQ = d\dot{m}(\omega r)r = \rho v_a 2\pi r dr(\omega r)dr \tag{34}$$

$$dQ = 4a'(1-a)\frac{1}{2}\rho v_0 \Omega r^2 2\pi r dr \tag{35}$$

The power generated over the area of an annulus can be found by multiplying the rotors angular velocity and the torque, Equation (36).

$$dP = \Omega dQ \tag{36}$$

Using this method, Equations (33), (35) and (36) are derived for the thrust, torque and power generation of an annulus of a rotor respectively. All three equations are functions of the axial induction factor, angular induction factor and the rotors angular velocity. These equations can then be applied to the Blade Element Momentum Theory to model the turbines response to wind loading [7].

4.2.3 Blade Element Momentum Theory

The Blade Element Momentum Theory is based on the force components acting on an airfoil due to its relative movement through a fluid. The lift, drag and pitching moment coefficients for a given reynolds number are provided by the blade manufacturer. An example of the provided airfoil coefficients is shown in Figure 12.

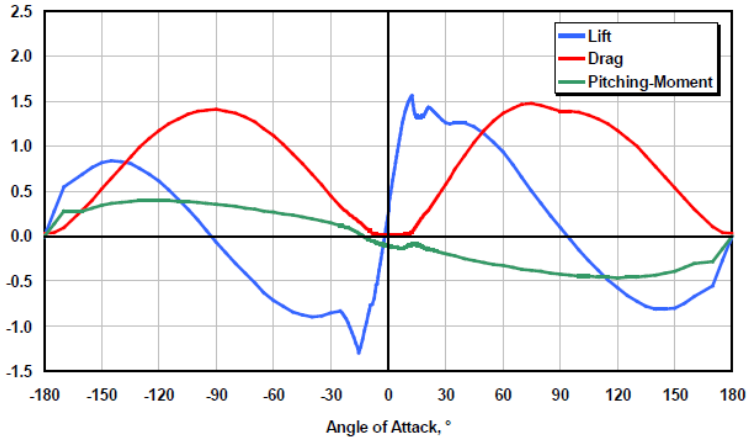

Figure 12: Example airfoil characteristics from the NREL 5 MW blade [38]

The force components acting on an airfoil are represented in Figure 13 as a velocity triangle. The lift component on the airfoil is the driving force behind the rotor torque. The lift acts perpendicularly to the relative inflow velocity, V_{rel}. The relative inflow velocity is the resultant flow of air over the airfoil due to the wind speed, rotor angular velocity and wake angular velocity. In addition to this, the airfoil experiences a drag component acting parallel to the relative inflow velocity.

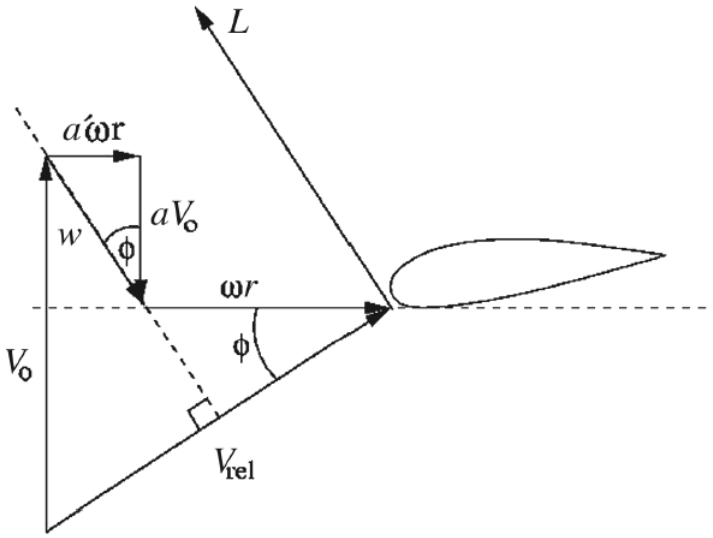

Figure 13: "Velocity triangle showing the induced velocities for a section of the blade" [7]

The force components act at the blade pitch angle ϕ away from the rotor plane. The force component is therefore translated into forces acting normally and tangentially to the rotor plane. This can be seen in Figure 14. The equations for this conversion can be seen in Equation (37) and Equation (38).

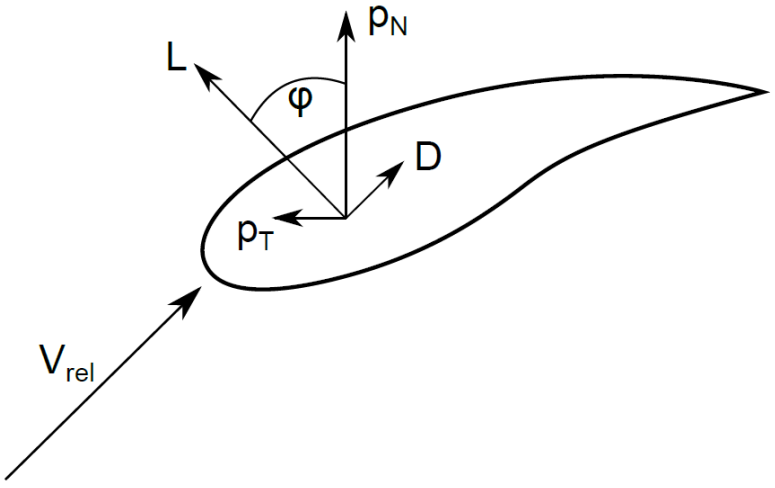

Figure 14: Lift and drag forces and their resultant force normal and tangential to the rotor place [9].

$$p_N = L\cos\phi + D\sin\phi \tag{37}$$

$$p_T = L\sin\phi + D\cos\phi \tag{38}$$

Equation (37) is the equation for the thrust force acting per unit length of a section on a single blade. The thrust acting on an annulus over the whole rotor is shown in Equation (39), where B is the number of blades and dr is the length of the annulus.

$$dT = Bp_N dr \tag{39}$$

The solidity ratio (σ) and the normal coefficient can also be introduced. The solidity ratio, shown in Equation (40), is the proportion of the rotor area covered by the blades. The normal coefficient is the coefficient of lift and drag acting normal to the rotor plane.

$$\sigma = \frac{Bc}{2\pi r} \tag{40}$$

$$C_n = C_l \cos\phi + C_d \sin\phi \tag{41}$$

An equation for the axial induction factor can be derived from the thrust over the annulus shown in Equation (33) and Equation (39).

$$a = \frac{1}{\frac{4sin^2\phi}{\sigma C_n} + 1} \tag{42}$$

The same process can be applied to the forces acting tangentially to the rotor which therefore produce torque. The same calculation process derives Equation (43).

$$a' = \frac{1}{\frac{4sin(\phi)cos(\phi)}{\sigma C_t} + 1} \tag{43}$$

Using this calculation process two expressions for the axial induction factor and the tangential induction factor have been found. Looking at Equation (42) and Equation (43) it is clear these equations are functions of ϕ, C_n and C_t. Each of these variables is also a function of the axial and tangential induction factor, therefore an iterative procedure is necessary to find a solution [7]. The steps to this process are as follows:

1. Initial a and a' estimate
2. Calculate ϕ and consequently α, C_l and C_d
3. Recalculate the values of a and a' using Equations (42) and (43)
4. Repeat until convergence
5. Calculate thrust, torque and power using converged values of a and a'

4.3 Statistical Motion Analysis

The floaters motion response will be derived entirely in the frequency domain. This is done because it offers an computationally effective approach to predicting dynamic responses. The floaters response spectra will be found by applying spectral loading to the system response amplitude operators (RAO). Spectral moments will then be used to extract statistics. The theory outlining this approach will be explained in this section.

4.3.1 Ocean Waves

Techniques for modelling sea surface elevations and wave amplitudes are extensively investigated and documented.

In this report the wave process is modelled through a step-wise approach. Long term sea state statistics are realised through a sum of statistics taken from stationary short-term conditions. A typical realisation of a wave field is defined as shown in Equation (44), where S_{JS} includes both a wave energy spectrum and wave direction function. The function is discretized in frequency and the directional range by ω_j and θ_k respectively where ε_{jk} is the phase angle. The model in the report only considers head-on loading which means the directional wave spectrum can be removed. A further simplified equation for a sea elevation time series can be found by applying Equation (45), returning Equation (46).

Each realisation is by definition both stationary and ergodic considering the sea-states key statistical parameters are maintained throughout.

$$\eta(t) = \sum_{j=1}^{n}\sum_{k=1}^{m}\sqrt{2S_{JS}\left(\omega_j,\theta_k\right)\Delta\omega_j\Delta\theta_k}\cos\left(\omega_j t-\varepsilon_{jk}\right) \tag{44}$$

$$A_j(\omega) = \sqrt{2S_{JS}(\omega)d\omega} \tag{45}$$

$$\eta(t) = \sum_{j=1}^{N} A_j\cos(\omega_j t - k_j x + \epsilon_j) \tag{46}$$

A number of wave energy spectra are available to use, however because long-term sea elevation data from the North-sea is available, the JONSWAP spectrum is used, hence the subscript JS. The definition of the JONSWAP spectrum can be seen in Equation (47) and a visualisation of the spectrum can be seen in Figure 15. Through these definitions the wave loading on the structure is fully defined by statistical quantities, it is therefore possible to derive response statistics which define the floater's movements assuming the system is time invariant.

$$S_{JS}(f) = 0.3125H_s^2T_p\left(\frac{f}{f_p}\right)^{-5}\exp\left(-1.25\left(\frac{f}{f_p}\right)^{-4}\right)\left(1-0.287\ln(\gamma_{JS})\right)\gamma_{JS}^{\exp\left(-0.5\left(\frac{\frac{f}{f_p}-1}{\sigma}\right)^2\right)} \tag{47}$$

$$\sigma = \begin{cases} 0.07, & \text{for } f \le f_p \\ 0.09, & \text{for } f > f_p \end{cases} \tag{48}$$

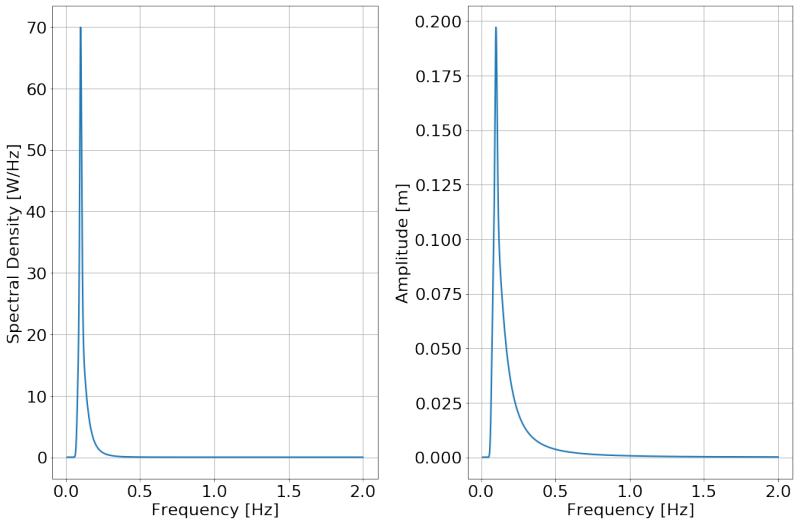

Figure 15: Jonswap spectrum, $\gamma = 3.3$, $T_p = 10$ s, $H_s = 6$.

4.3.2 Wave Elevation

Each wave process can be approximated by a Gaussian distribution as a result of the central limit theorem. A probability distribution taken from a time series is shown in Figure 16 validating this assumption.

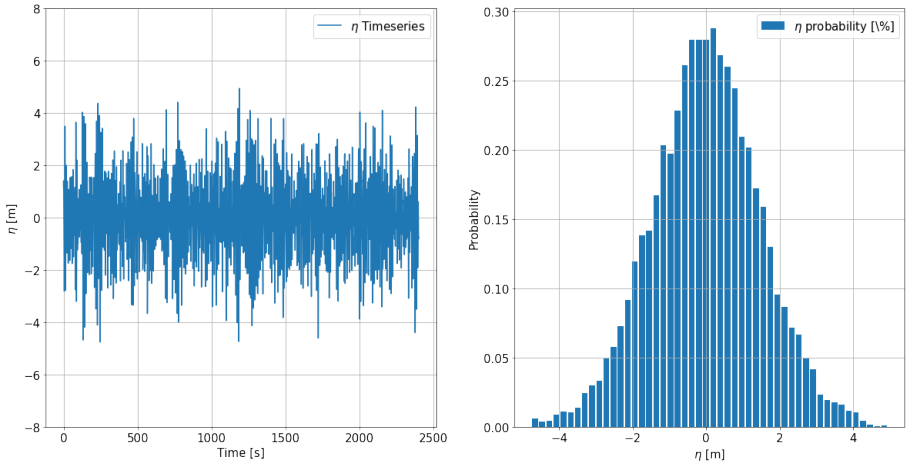

Figure 16: Free surface elevation time series and histogram.

The variance of the wave process can be derived from the wave energy spectrum also called the variance spectrum. This is done by taking the autocovariance function at $\tau = 0$, as seen in Equation (49).

$$\sigma^2 = C_x(0) = \int_0^\infty S_{JS}(\omega) \quad d\omega \tag{49}$$

The Gaussian distribution is shown in Equation (50) as a function of x where the variables σ and μ represent mean and standard deviation.

$$\phi(x) = \frac{1}{\sigma\sqrt{2\pi}} \exp \frac{1}{2} \left(\frac{x-\mu}{\sigma} \right)^2 \tag{50}$$

At this point it is convenient to introduce the concept of spectral moments which simplify the calculation process. Each spectral moment is defined as shown in Equation (51). Reviewing Equation (49) and Equation (51) it can be seen $m_0 = \sigma^2$. Applying this substitution and the known zero mean, Equation (50) can be simplified Equation (52).

$$m_j = \int_{-\infty}^{\infty} S_X(\omega) \cdot \omega^j \quad d\omega \qquad\qquad j = 1...n \tag{51}$$

$$f(x, m_0) = \frac{x}{m_0} \cdot \exp\left(-\frac{x^2}{2 \cdot m_0} \right) \tag{52}$$

The Gaussian probability distribution can be further utilised to find the mean zero-crossing rate. A zero-crossing is defined as the sea elevation X passing the SWL with a positive slope $\dot{X}$. The calculation process initially finds the probability of the process crossing an arbitrary amplitude a with a positive slope. The variables X and $\dot{X}$ are known to be statistically independent, because of this Equation (53) can be derived from the joint-probability function. This derivation is outlined in full by Naess and Moan [42].

$$v^+(a) = \frac{1}{2\pi} \frac{\sigma_{\dot{X}}}{\sigma_X} \exp\left\{ -\frac{1}{2} \left(\frac{a - m_X}{\sigma_X} \right)^2 \right\} \tag{53}$$

By setting the arbitrary amplitude, a, to zero, the average number of times per unit time the process crosses the zero mean is found as seen in Equation (54) . The inverse of this is the mean zero-crossing period and can be seen in Equation (55).

$$v^+(0) = \frac{1}{2\pi} \frac{\sigma_{\dot{X}}}{\sigma_X} \tag{54}$$

$$T_z = \frac{1}{v^+(0)} = 2\pi \sqrt{\frac{m_{r,0}}{m_{r,2}}} \tag{55}$$

From this it is possible to calculate the number of waves N in a wave process realisation of duration T_R by dividing the T_R by T_z as shown in Equation (56). The probability of the maximum wave amplitude during this realisation is equal to the inverse of N_{MPM}, therefore the probability of a wave being smaller than the X_{MPM} is given by Equation (57).

$$N = \frac{T_r}{T_{2,x}} \tag{56}$$

$$P_{MPM} = 1 - \frac{1}{N_{MPM}} \tag{57}$$

4.3.3 Wave Crest

The Gaussian distribution of the wave elevation is a useful tool in deriving expected wave parameters, however the extreme loading and response of the floater is likely to dictate the feasibility of a design. As proved by Naess and Moan, the wave crests are better represented by a normal distribution. The derivation process which proves this assumes a narrow band process where a single peak occurs for ever zero-mean crossing. Therefore the probability distribution of a crest exceeding an arbitrary value a can be defined as shown in Equation (58) and the cumulative distribution function as shown in Equation (59). By substituting Equation (54) into these equations the probability and cumulative probability densities can be found, these can be seen in Equations (60) and (61) respectively.

$$\text{Prob}\left(X_p > a\right) = \frac{v_X^+(a)}{v_X^+(0)} \tag{58}$$

$$\Phi_{X_p}(a) = 1 - \frac{v_X^+(a)}{v_X^+(0)} \tag{59}$$

$$\Phi_{X_p}(a) = 1 - \exp\left(-\frac{1}{2}\frac{a^2}{\sigma_X^2}\right) \tag{60}$$

$$\phi_{X_p}(a) = \frac{a}{\sigma_X^2}\exp\left(-\frac{1}{2}\frac{a^2}{\sigma_X^2}\right) \tag{61}$$

The Rayleigh distribution is therefore used to predict extreme response values of the wave process. In order to validate this assumption the Rayleigh distribution is shown plotted over the wave crest probability distribution derived from the three hour η time series. This is shown in Figure 17. It can be seen that the histogram loosely follows the Rayleigh distribution. A closer fit may be found in a longer time series.

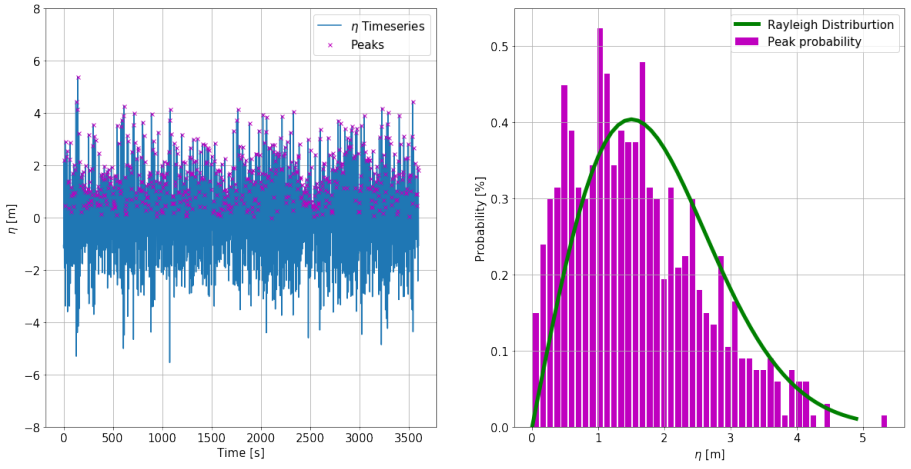

Figure 17: Peaks of the free surface elevation time series and corresponding histogram.

Extreme response values can be found by equating the wave crests probability and $\Phi(x)$. As an example, the X_{MPM} can be found as shown in Equation (63).

$$\Phi(x) = 1 - \exp\left(\frac{-x^2}{2\sigma^2}\right) \tag{62}$$

$$X_{MPM} = \sqrt{2 \cdot m_0 \cdot \ln\left(N_{MPM}\right)} \tag{63}$$

4.3.4 System Response

The spectral moments can also be applied to find the response statistics from a system response spectrum. To calculate the response spectrum $S_X(\omega)$, its relationship with the load spectrum $S_F(\omega)$ must be established. This connection is set out by Moan and Naess and summarised in this report [41]. The calculation process maintains the the system must be modelled as a linear and time invariant.

It is known that the response spectrum $S_X(\omega)$ is defined at the Fourier transform of the autocovariance function $C_X(\tau)$, as shown in Equation (64)

$$S_X(\omega) = \frac{1}{2\pi} \int_{-\infty}^{\infty} C_X(\tau) e^{-i\omega\tau} d\tau \tag{64}$$

While the autocovariance function can be defined as shown in Equation (65), where h_{FX} is an impulse response function of a stochastic load process.

$$C_X(\tau) = \int_0^{\infty} \int_0^{\infty} h_{FX}\left(s_1\right) h_{FX}\left(s_2\right) C_F\left(\tau + s_1 - s_2\right) ds_1 ds_2 \tag{65}$$

By substituting $C_X(\tau)$ into Equation (64) and changing the integration order it, Equation (66) can be derived.

$$S_X(\omega) = \int_0^{\infty} h_{FX}\left(s_1\right) \int_0^{\infty} h_{FX}\left(s_2\right) \cdot \frac{1}{2\pi} \int_{-\infty}^{\infty} C_F\left(\tau + s_1 - s_2\right) e^{-\mathrm{i}\omega\tau} d\tau ds_2 ds_1 \tag{66}$$

By letting $\theta = \tau + s_1 - s_2$ and $d\theta = d\tau$ the following equations can be deduced.

$$S_X(\omega) = \int_0^{\infty} h_{FX}\left(s_1\right) \int_0^{\infty} h_{FX}\left(s_2\right) \cdot \frac{1}{2\pi} \int_{-\infty}^{\infty} C_F(\theta) e^{-\mathrm{i}\omega\theta} d\theta e^{\mathrm{i}\omega(s_1 - s_2)} ds_2 ds_1 \tag{67}$$

$$= \int_0^{\infty} h_{FX}\left(s_1\right) e^{\mathrm{i}\omega s_1} ds_1 \int_0^{\infty} h_{FX}\left(s_2\right) e^{-\mathrm{i}\omega s_2} ds_2 \cdot S_F(\omega) \tag{68}$$

$$= H_{FX}(-\omega) H_{FX}(\omega) S_F(\omega) \tag{69}$$

Because it is known that $e^{-ex} = e^{ex}$ and that $h_{FX}(t)$ is a real function. The simple connection between response spectrum and load spectrum can be proven.

$$S_X(\omega) = |H_{FX}(\omega)|^2 \cdot S_F(\omega) \tag{70}$$

4.4 Sequential Least Squares Programming - SLSQP

Function optimization is an expansive research field where a wealth of optimization code is freely available online. Depending on the requirements of the optimization and the nature of the objective function, constraints and design variables, some algorithms will be more suited than others.

In this report the aim is to minimize a continuous scalar objective function subject to constraints and bounds. In addition to this, it is desirable to minimize the time and computational requirements of the optimization. It is therefore decided to use the gradient based Scipy SLSQP minimise function. The reason for this decision is that the optimizer is compatible with both constraints and bounds and offers reduced computational power compared to gradient-free optimization methods.

At their core, all gradient-based optimization techniques consist of similar sub-routines. At each iteration of an optimization the optimizer must determine a search direction and a step size. The search direction is determine by the derivative of the objective function. Depending on your chosen optimizer this may include first and second order derivatives. The step size is then determined by conducting a line-search along the search direction, once a point is found that satisfies certain decent requirements the iteration is complete.

The SLSQP is composed of a series of sub-routines to determine gradient, search direction and step size. The method used in SciPy SLSQP is a slightly altered version of Lawson and Hanson's 'Non-Negative Least Squares Problem' (NNLS) solver. The NNLS method is obtained from the 'Linear Least Square Formulation" (LSEI) which is found to be equivalent to the general quadratic programming problem (QP) [43]. The differences in methodology behind the NNLS and QP are likely due to implementation practicalities. Therefore the theory behind QP will closely reflect the SciPy SLSQP calculation process. The theory behind QP is explained in full in Engineering Design Optimization by J. Martin and A. Ning, while a summary if presented below [44].

4.4.1 Quadratic Programming

Quadratic programming is a concept on which a lot of optimizers are based. In its most basic form, that is to say without the inclusion of equality or in-equality constraints, sequential programming is comparable to a Newton's line search.

The Newton's line search approximates the objective function using quadratic model. The search direction and step size are found by solving the quadratic model for a stationary point.

Consider the Taylor expansion of an objective function as shown in Equation (71). In this equation $x^{(k)}$ is an iteration start point and $s^{(k)}$ is the step required to minimize the function. $H^{(k)}$ is annotation for the function Hessian, a matrix of second order derivatives. As Newton's method approximates the function as a quadratic, higher order terms are neglected. The minimum of the objective function will occur where the derivative of the function is zero.

$$f\left(x^{(k)}+s^{(k)}\right)=f^{(k)}+\nabla f^{(k)^T}s^{(k)}+\frac{1}{2}s^{(k)^T}H^{(k)}s^{(k)}+\ldots O(f^{(n,k)}) \tag{71}$$

By taking the derivative, as seen in Equation (72), the step size approximation can calculated as shown in Equation (73). This procedure is carried out iteratively until convergence.

$$\frac{\mathrm{d}f\left(x^{(k)}+s^{(k)}\right)}{\mathrm{d}s^{(k)}} = \nabla f^{(k)} + H^{(k)}s^{(k)} = 0 \tag{72}$$

$$s^{(k)} = -H^{(k)^{-1}}\nabla f^{(k)} \tag{73}$$

This is the core principle behind the SLSQP method, however additional complexities are incorporated into the model to improve efficiency. The objective function Hessian is often unknown and costly to calculate, as a result the SLSQP method uses Quasi-Newton Methods to approximate the objective function Hessian.

Quasi-Newton Methods approximate the second order terms of the Hessian using first order derivatives. The process can be seen in Equation (74) and is equal to the change in first order derivatives per unit variable. By running this calculation on each of the design variables, an approximation of the Hessian is found, annotated $\boldsymbol{B}$. This introduces the secant condition. The secant condition states that $\boldsymbol{B}$ multiplied by step size $s^{(k)}$ must be equal to the change in gradients between the two points. This is shown in Equation (75) [44].

$$f''^{(k+1)} = \frac{f'^{(k+1)} - f'^{(k)}}{\left(x^{(k+1)} - x^{(k)}\right)} f'^{(k+1)} - f'^{(k)} \tag{74}$$

$$B^{(k+1)}s^{(k)} = \nabla f^{(k+1)} - \nabla f^{(k)} \tag{75}$$

The secant condition leaves us with n equations, where n is the number of variables. However the positive definite $n \cdot n$ matrix $\boldsymbol{B}$ will have $n(n+1)/2$ unknown variables. There is therefore a requirement to add additional restraints on the system.

It is known that $\boldsymbol{B}$ is positive definite, therefore the secant condition is only possible if the predicted curvature is positive along the step. As shown in Equation (76). Despite this, the approximate Hessian is still indeterminate.

$$s^{(k)^T}\left(\nabla f^{(k+1)} - \nabla f^{(k)}\right) > 0 \tag{76}$$

The method therefore chooses the approximation $\boldsymbol{B}^{(k-1)}$. As there are a large number of approximations which satisfy Equation (75), the method settles on the approximation closest to the previous solution $\boldsymbol{B}^{(k-1)}$. Finding which Hessian approximation is closest to the previous approximation leads to an optimization problem itself [44]. Fortunately, this optimization has a analytical solution.

Depending on the chosen quasi-Newton method small variations in the rest of the derivation will occur. Because the BFGS method is most similar to that of the SLSQP, its derivation will be used. The key difference in the BFGS quasi-Newton method is that the method solves directly for the inverse of the Hessian rather than the Hessian itself. This is best

shown in Equation (77) with the new variable V being equal to the inverse of H. The benefit of this is that it removes the need to calculate an inverse matrix.

$$s^{(k)} = -H^{(k)^{-1}} \nabla f^{(k)} = -V^{(k)} \nabla f^{(k)} \tag{77}$$

Using the new variable V, the analytical solution to the Hessian optimization can be seen in Equation (78).

$$V^{(k+1)} = \left[I - \frac{s^{(k)} y^{(k)^T}}{s^{(k)^T} y^{(k)}} \right] V^{(k)} \left[I - \frac{y^{(k)} s^{(k)^T}}{s^{(k)^T} y^{(k)}} \right] + \frac{s^{(k)_5 (k)^T}}{s^{(k)^T} y^{(k)}} \tag{78}$$

$$\tag{79}$$

4.4.2 Equality Constraints

The aforementioned theory follows the simplest case. As mentioned previously, the optimization problem in the report required the inclusion of constraints and bounds. Adding constraints to the problem requires a revision of the optimality conditions. The theory for an equality constraint is presented first because it is the basis on which inequality constraints are founded.

Consider a simple optimization problem as shown in Equation (139). In an unconstrained system a local minimum is the smallest value in the design space vicinity. The optimality condition can be shown in Equation (81), this can only be possible if the gradient in every search direction is positive. In an unconstrained system, a point can only satisfy this condition if its gradient is zero. In other words, if the point displays any slope a smaller value must exist and the point cannot be considered a minimum. This is not always the case for a constrained system [44].

$$\begin{array}{ll} \text{minimize} & f(x) \\ \text{subject to} & Ax + b = 0 \\ & Cx + d \leq 0 \end{array} \tag{80}$$

$$f\left(x^* + p\right) \geq f\left(x^*\right) \tag{81}$$

In an equality constrained system, the search direction is no longer free to descend in any direction. Any step must satisfy the constraint, in this case $Ax + b = 0$. The conditions for which this is true can be seen by considering the Taylor expansion of an arbitrary equality constraint $h_j(x)$ as shown in Equation (82). It is known that any two feasible points must equal zero, therefore the gradient between two feasible points must also equal zero. In other word, in an equality constrained system, the search direction p must act perpendicularly to the equality constraint gradient. This adds another optimality condition to the system. For a point to be considered a constrained minimum, Equation (81) must be true where the search direction satisfies Equation (83).

$$h_j(x+p) \approx h_j(x) + \nabla h_j(x)^T p + O(h_j) \tag{82}$$
$$\nabla h_j(x)^T p = 0 \tag{83}$$

By expanding these optimality conditions to problems with higher dimensions it can be proved that for a constrained minimum, the gradient at the minimum must be equal to the gradient of the constraint. This is because a difference in gradient would suggest another point which doesn't satisfy Equation (81). Therefore, at an optimum, the gradient of the objective function must be equal to a linear combination of the constraint gradients. This condition can be written out as shown in Equation (84). Where the variable λ is an unknown $1 \times n$ Lagrange multiplier.

$$\nabla f\left(x^*\right) = -\sum_{j=1}^{n_h} \lambda_j \nabla h_j\left(x^*\right) \tag{84}$$

The full set of optimality conditions can be derived from the Lagrangian function. The lagrangian function is defined as shown in Equation (85). The Lagrangian stationary points are potential minima for the constrainted problem.

$$\mathcal{L}(x, \lambda) = f(x) + \lambda^T h(x) \tag{85}$$

This is explained by taking the partial derivatives of the function with respect to the design variable x and the Lagrange multipliers λ. The analytical solution of which can be found in Equation (86). The first partial derivative can be seen to be equal to the optimality condition shown in Equation (84), while the second is equal to Equation (83).

$$\begin{array}{ll} \frac{\partial \mathcal{L}}{\partial x_i} = \frac{\partial f}{\partial x_i} + \sum_{j=1}^{n_h} \lambda_j \frac{\partial h_j}{\partial x_i} = 0, & i = 1, \ldots, n_x, \\ \frac{\partial \mathcal{L}}{\partial \lambda_j} = h_j = 0, & j = 1, \ldots, n_h. \end{array} \tag{86}$$

It is therefore possible to convert an constrained problem to an unconstrained problem through the use of the Lagrange Multipliers and the Lagrangian equation.

4.4.3 Inequality Constraints

Inequality constraints are incorporated into the Largrangian function in a similar way to equality constraints. The difference between the two method is the process used to distinguish whether or not an inequality constraint is active.

The relationship between the objective function gradient and the linear combination of inequality constraint gradients can be written similarly to the equality constraints. This can be seen in Equation (87), where g_j represents the inequality constraint.

$$\nabla f\left(x^{*}\right)=-\sum_{j=1}^{n_g}\sigma_j\nabla g_j\left(x^{*}\right) \tag{87}$$

The difference arises through the addition of the slack variable s. The slack variable is used to determine whether or not an inequality constraint is active. The slack variable is included in the constraint as shown in Equation (88). The slack variable is defined so that Equation (88) holds true when the inequality is active, and false when the inequality is inactive. The new inequality constraint can then be included in the Lagrangian equation as shown in Equation (89).

$$g_k+s_k^2=0 \tag{88}$$

$$\mathcal{L}(x,\lambda,\sigma,s)=f(x)+\lambda^T h(x)+\sigma^T\left(g(x)+s^2\right) \tag{89}$$

The Lagrangian stationary points including the inequality constraint still maintains it's significance of representing potential minima, however the partial derivative now includes partial derivatives with respect to the inequality Lagrange multiplier σ and slack variable s. The partial derivative of the inequality Lagrange multiplier operates under the same significance as its equality counterpart. However, the partial derivative of the slack variable, also named the complementarity condition, indicates whether or not each of the inequality partial derivatives is active or in-active. The conditions are called the Karush–Kuhn–Tucker conditions [44].

$$\begin{aligned}
\frac{\partial f}{\partial x_i}+\sum_{j=1}^{n_h}\lambda_j\frac{\partial h_j}{\partial x_i}+\sum_{k=1}^{n_g}\sigma_k\frac{\partial g_k}{\partial x_i}=0, &\qquad i=1,\ldots,n_x\\
h_j=0, &\qquad j=1,\ldots,n_h\\
g_k+s_k^2=0, &\qquad k=1,\ldots,n_g\\
\sigma_k s_k=0, &\qquad k=1,\ldots,n_g\\
\sigma_k\geq 0, &\qquad k=1,\ldots,n_g
\end{aligned} \tag{90}$$

5 Model

This section will detail the data pipeline which builds the MUFP's transfer functions from four design variables. These design variables are the distance between the front and back columns (x_c), the distance between the back columns (y_c) in addition to the column diameters (D_c) and draft (Dr).

The overall goal of the code is to return response metrics for a system design based on a small number of input variables. The system will resemble the floater shown in Figure 18. These response metrics will feed into the Scipy SLSQP optimizer.

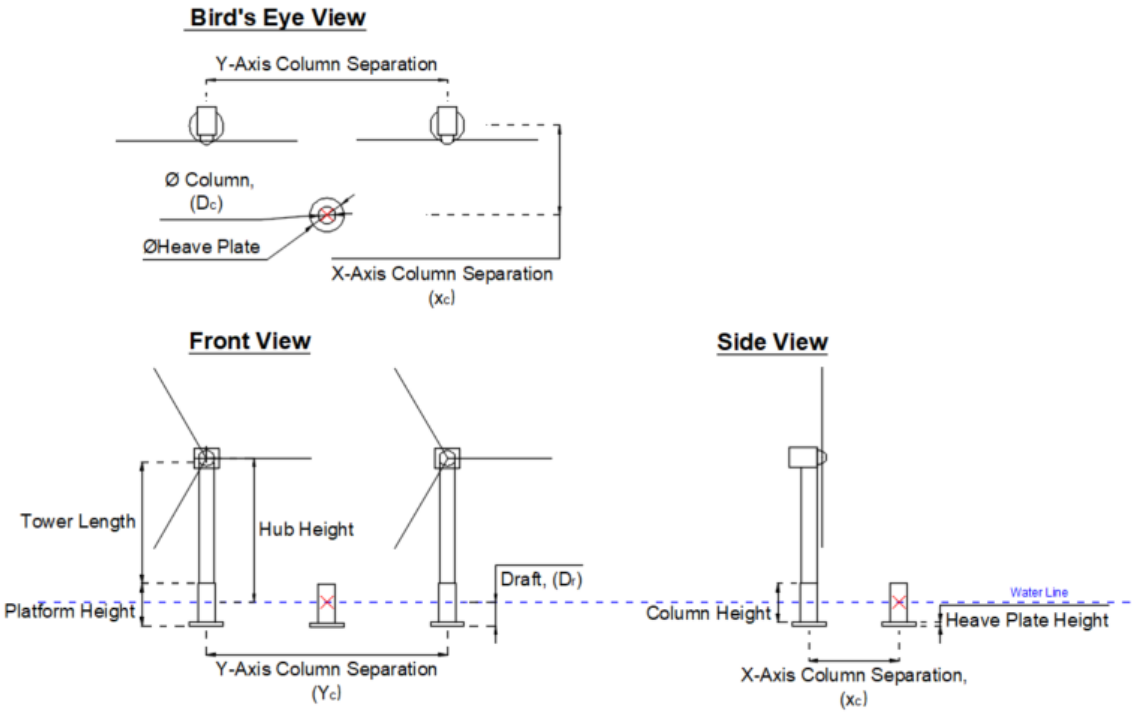

Figure 18: MUFP Design. Origin is marked with the red cross.

The code is broken down into individual files and classes as shown in Figure 19. The document will explain each box in chronological order, or the order shown in Figure 19.

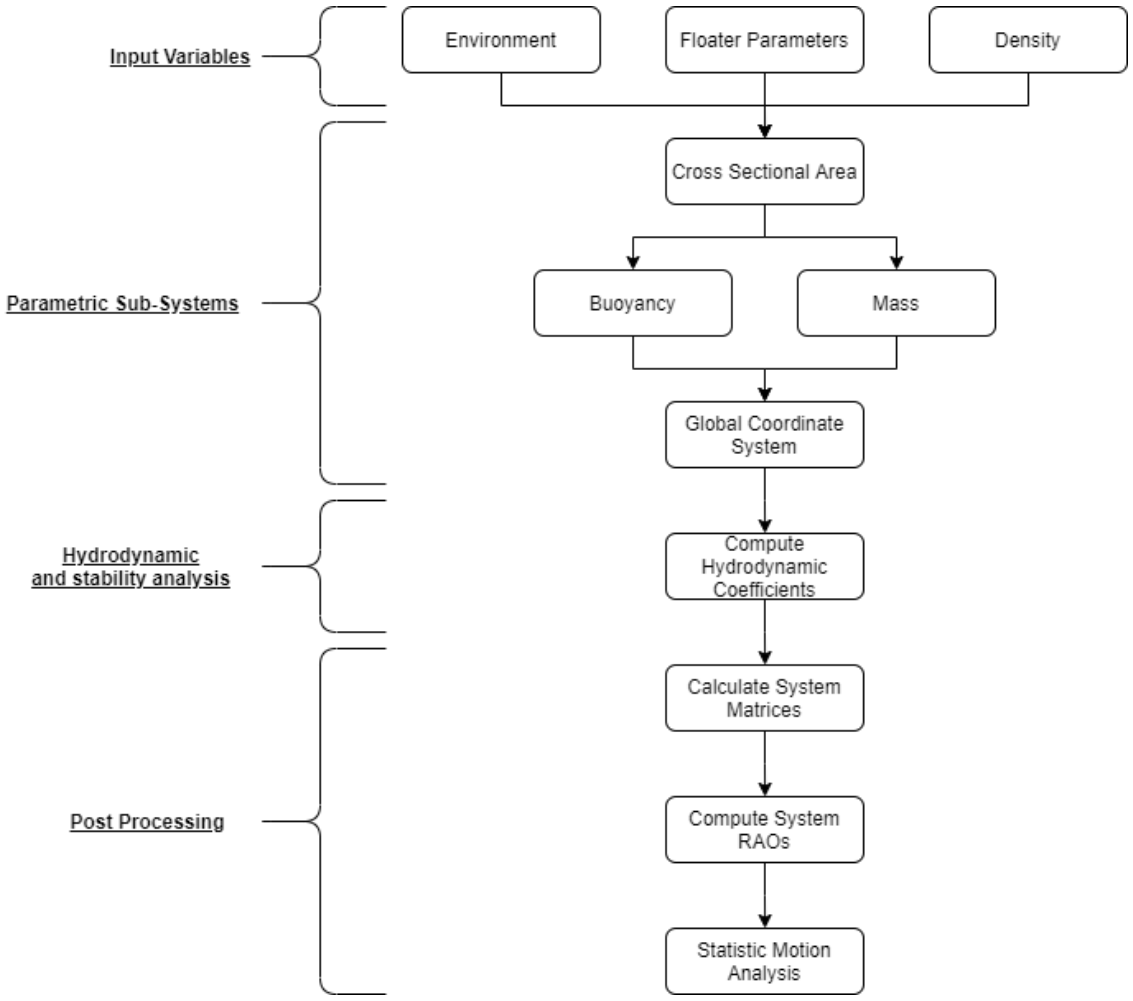

Figure 19: Data pipeline visualisation.

5.1 Input Variables

The system input variables is the name given to the Environment, Floater Parameters and Density functions. These functions are a combination of fixed environmental conditions, fixed floater parameters and the optimization free variables.

5.1.1 Environment & Density

The Environment and Density classes solely define quantities for gravity and the densities of steel, sea water and concrete. These are taken as 9.80665 $[m/s^2]$, 8500 $[kg/m^3]$, 1025 $[kg/m^3]$ and 2500 $[kg/m^3]$ respectively.

5.1.2 Floater Parameters

This class defines all fixed design variables. These fixed variables are defined as shown in Table 1. The class also takes the free variables as an argument.

Table 1: Fixed input variables.

Parameter	**Value**	**Unit**
Heave Plate Diameter	20	m
Heave Plate Height	2	m
Hub Height	85	m
Hub Spacing	142.1	m
Draft	14	m
Floater Height	25	m
Steel Thickness	0.07	m

5.2 Parametric Sub-Systems

In this document a sub-system will be defined as a function or group of functions which further define the floater using the system input variables. The parametric subsystems are named **Area**, **Buoyancy**, **Mass** and **Global Coordinate System**.

5.2.1 Cross Sectional Area

The **Area** class defines the cross-sectional areas of the floater columns using the floater dimensions. This is done trivially using the equation of a circle.

5.2.2 Buoyancy

The **Buoyancy** class calculates the buoyancy of each component along with the aggregated buoyancy of the floater. This is done by taking the volume of the heave plates and submerged columns multiplied by the density of water. The buoyancy of bracing is currently not considered.

5.2.3 Mass

The **Mass** class calculates and defines the floater's component masses. Firstly the class defines additional parameters in order to fully dimension the floater. The turbine masses are defined as shown in Table 2. These masses are taken from the NREL 5 MW reference turbine [38].

Table 2: Turbine Masses [38]

Component	**Mass**	**Unit**
Hub	5.6780×10^{4}	kg
Nacelle	2.4000×10^{5}	kg
Rotor	1.1000×10^{5}	kg

The tower diameter, taper and thickness are currently set equal to the dimensions of the NREL 5 MW reference turbine tower [38]. Considering the hub separation must remain constant as the column separation decreases, the length and the tower must be calculated as a function of y_c. The length of the tower is calculated by taking the Pythagoras of the hub height (h_{hub}) and the difference between the column and hub y-axis positioning,

annotated y_c and y_h respectively as shown in Equation (91). The volume of the tower is calculated using the volume equation for a tapered cylinder as shown in Equation (92). In this equation, R indicates the radius at the bottom of the tower, and r represents the radius at the top of the tower, while the subscripts *in* and *out* indicate the inside and outside radius of the cylinder. Finally the tower mass is simply calculated using Equation (93). The tower dimensions defined in this class can be seen in Table 3.

Table 3: Turbine tower dimensions

Parameter	**Value**	**Unit**
R_{in}	2.960	m
R_{out}	3.000	m
r_{in}	1.932	m
r_{out}	1.935	m

$$L_t = \sqrt{\left(\frac{y_h - y_c}{2}\right)^2 + h_{hub}^2} \tag{91}$$

$$V_t = \frac{\pi}{3} \cdot L_t \cdot \left(R_{out}^2 + r_{out}^2 - R_{in}^2 - r_{in}^2 + R_{out} \cdot r_{out} - R_{in} \cdot r_{in}\right) \tag{92}$$

$$M_t = V_t \cdot \rho_{steel} \tag{93}$$

The **Mass** subsystem also calculated the weight of the bracing between each of the columns. The design of structural steel in the offshore environment is an iterative procedure in which steel is dimensioned based on hydrodynamic and hydrostatic loads, which are in turn determined by the dimensions of the steel.

Therefore a simplified dimensioning process is developed which computes a bracing design based on the optimization design variables at high speed. It is important to bear in mind that the intention of the optimization is to determine high level design decisions rather than produce a detailed design.

It is decided that the horizontal bracing members will lie 7 m above and below the water line. The length of the horizontal members is calculated as the distance between the columns. Therefore the length of bracing between the back columns is equal Equation (94) and the bracing between the front and back columns is equal to Equation (95).

$$L_{b1} = y_c - D_c \tag{94}$$

$$L_{b2} = \sqrt{x_c^2 + \frac{y_c}{2}^2} - D_c \tag{95}$$

The next step is allocating diagonal members to support the horizontal members. The lengths of these members largely depends on the number "K" bracing bays designed into the section. For this optimization the number of bays is determined as the smallest number which is able to maintain acceptable weld angles. This angle will depend on the manufacturer however, in this report, the limit is set to 30°.

The number of "K" bracings, labeled N_{bays}, is found by increasing the number included in the design until the welding criteria is met. This is shown in Equation (96) where h_b is the height between the top and bottom horizontal member. The first number to achieve this is the chosen number of "K" bracings in the floater design.

$$\theta = \arctan\left(\frac{h_b}{\frac{L_{b,i}}{2 \cdot N_{bays}}}\right) > 30^\circ \tag{96}$$

Using this method, the length of all bracing members can be calculated. Due to the horizontal bracing members being positioned parallel to one other, each diagonal member in a section of bracing will be of equal length. There are therefore only 4 variations of bracing length used in the design. These members will undergo an initial dimensioning based on a slenderness rule of thumb.

Due to the length of each of the members the most likely form of failure will be buckling. Therefore the diameter of each member will most likely be governed by its slenderness λ which is defined as shown in Equation (97). Where K is the effective buckling length coefficient, r_g is the radius of gyration and L is simply the member length.

$$\lambda = \frac{KL}{r_g} \quad \text{Where:} \quad \lambda = 100 \quad \& \quad K = 1 \tag{97}$$

As a rule of thumb the value of λ can be taken as 100 for horizontal members and 80 for diagonal members, while K can conservatively be set equal 0.8. The radius of gyration is defined as shown in Equation (98) and is a function of the member's second moment of inertia and cross-sectional area.

$$r_g = \sqrt{\frac{I}{A}} \tag{98}$$

Each member's second moment of inertia and cross-sectional area can be found using Equations (99) and (100). By substituting the value of D_i for the outer diameter minus two times the member thickness, and then saying $t^2 \approx 0$, a simplification can be made. Similarly Equation (99) can be simplified by making the same substitution and truncating any term with t to a power of two or higher. This approximation is based on t being small.

$$I = \frac{\pi}{64}\left(D_{\mathrm{o}}^4 - D_{\mathrm{i}}^4\right) \approx \frac{\pi}{8} D^3 t \tag{99}$$

$$A = \frac{\pi}{4}\left(D_{\mathrm{o}}^2 - D_{\mathrm{i}}^2\right) \approx \pi D t \tag{100}$$

Using these approximations, a simplified equation of r_g can be derived, as shown in Equation (101).

$$r_g \approx \frac{D}{2\sqrt{2}} \tag{101}$$

Substituting this back into Equation (97) leaves us with Equation (102) which can be used as a quick approximation for a member diameter.

$$D = \frac{K \cdot L}{\lambda} \cdot 2\sqrt{2} \tag{102}$$

Another rule of thumb can be used to determine the thicknesses of the member. Manufacturing limits during the cold rolling of large steel cylinders typically require the the ratio between diameter and thickness to lie in the region prescribed in Equation (103). The lower region can be expected for members expected to experience high fatigue damage. It is therefore chosen to determine the thickness of the horizontal members using a ratio of 30 while diagonal members at a ration of 45.

$$24 < \frac{D}{t} < 60 \tag{103}$$

This calculation process in implemented in the code. In order to investigate the relationship between column separation and bracing mass, a cut through the design space is taken. This can be seen in Figure 20. The function was called for a floater design spanning 30 m $< x_c$ $<$ 100 m. It can be seen that the relationship is effectively continuous with a small jump seen at 88 m. It is therefore not expected to compromise the optimization's requirement of a continuous function.

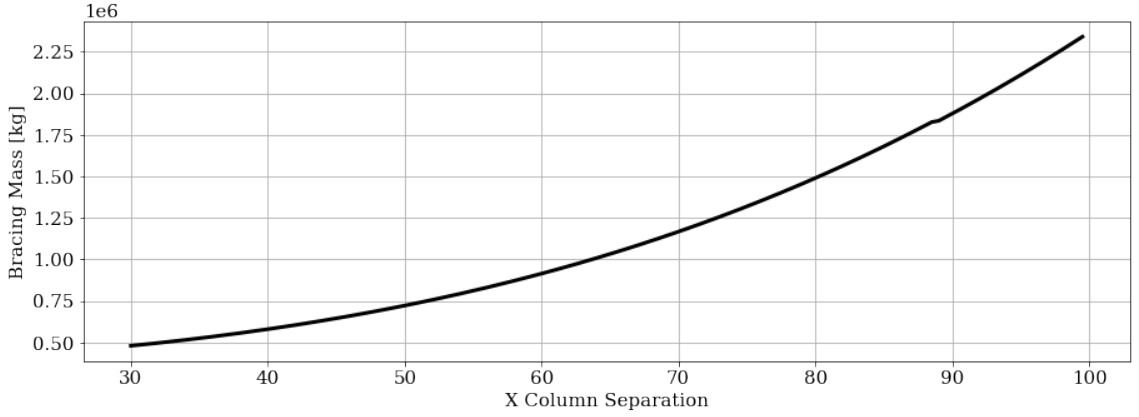

Figure 20: Bracing mass as a function of the x_c column separation.

The **Mass** class then calculates the required ballasting in the system by subtracting the weight of the un-ballasted floater from the total buoyancy.

5.2.4 Global Coordinate System

The system centre of mass, radius of gyration and product of inertia are calculated in this class. This is done by allocating the masses and buoyancy of the system into a global coordinate system and taking a weighted average of the coordinates. The origin of the coordinate system is taken at the centre of the front column on the still water level, this is visualised in Figure 18.

The sub system collects the mass components into a DataFrame. The mass of the columns and heave plates are placed at their respective centre points, determined by the input design variables. The tower mass z coordinate is allocated at the hub height divided by 2.3. This is to account for the non-uniform mass distribution over its length. A similar approach is taken when determining the y coordinate, this is calculated using Equation (104), where y_c and y_h are y coordinates of the column and hub respectively.

A weighted average of the x, y and z coordinates is then taken to determine the un-ballasted platform COM. An extract is shown in Table 4. In this example inputs of 60 m, 80 m, 12 m and 14 m are used for the x and y spacing, column diameter and draft, respectively.

$$y_t = y_c + \left(\frac{y_h - y_c}{2.3}\right) \tag{104}$$

Table 4: Extract of unballasted system masses

Component	x [m]	y [m]	z [m]	Mass [t]
Front Column	0.00	0.00	-0.50	580.2
Back Left Column	-60.00	-40.00	-0.50	580.2
Back Right Column	-60.00	40.00	-0.50	580.2
Front Heave Plate	0.00	0.00	-13.00	381.1
Back Left Heave Plate	-60.00	-40.00	-13.00	381.1
Back Right Heave Plate	-60.00	40.00	-13.00	381.1
Left RNA	-60.00	-71.05	85.00	406.8
Right RNA	-60.00	71.05	85.00	406.8
Left Tower	-60.00	-53.50	36.96	342.5
Right Tower	-60.00	53.50	36.96	342.5
Left xy Bracing	-30.00	-20.00	0.00	214.6
Right xy Bracing	-30.00	20.00	0.00	214.6
Back Bracing	-60.00	0.00	0.00	307.1
Centre of Mass	-46.22	0.00	15.38	5118.6

The allocation of ballast between the front and back columns is calculated with the objective of aligning the COM with the COB in the x and y plane. The calculation process simplifies the floater into two masses: the un-ballasted floater and the ballast. The COM of the un-ballasted floater is known, therefore the COM of the ballast can be placed to offer an equal mass distribution around the COB. The floater is symmetric around the x-axis, therefore the COM and COB already positioned at $y = 0$.

In order to calculate the x-coordinate, the distance along the x-axis between the un-ballasted floater COM and its COB is calculated. Using this distance along with a ratio between the floater mass and the ballast mass, the required positioning of the ballast's COM along the x-axis needed to align the ballasted floater COM with its COB is computed. This process is shown in Equations (105) and (106), where M_f and M_b are the un-ballasted floater mass and ballast mass respectively. X_b, X_f and COB_x are the x-coordinate of the ballast COM, un-ballasted floater COM and COB.

$$\phi_{mass} = \frac{M_b}{M_f} \tag{105}$$

$$X_b = COB_x - \frac{COB_x - X_f}{\phi_{mass}} \tag{106}$$

$$\tag{107}$$

The ballast is then allocated to the front and back columns to create an equal ballast mass distribution around X_b. The moment arms to the front and back columns are calculated using Equations (108) and (109) respectively. Ballast proportional to each moment arm is then allocated to the front and back columns, as shown in Equations (110) and (111)

$$L_1 = x_{c,1} - X_b \tag{108}$$

$$L_2 = L_1 - x_c \tag{109}$$

$$M_{B,front} = \frac{L_2}{x_{spacing}} \cdot M_{b,tot} \tag{110}$$

$$M_{B,back} = M_{b,tot} - M_{B,front} \tag{111}$$

Using this calculation the final mass distribution of the floater can be seen in Table 5. The corresponding centre of mass and buoyancy along with their corresponding weight and buoyancy can be seen in Table 6.

Table 5: Extract of system masses

Component	x [m]	y [m]	z [m]	Mass [t]
Front Ballast	0.0	0.00	-13.45	859.2
Back Left Ballast	-60.0	-40.00	-13.96	63.8
Back Right Ballast	-60.0	40.00	-13.96	63.8
Front Column	0.0	0.00	-0.50	580.2
Back Left Column	-60.0	-40.00	-0.50	580.2
Back Right Column	-60.0	40.00	-0.50	580.2
Front Heave Plate	0.0	0.00	-13.00	381.1
Back Left Heave Plate	-60.0	-40.00	-13.00	381.1
Back Right Heave Plate	-60.0	40.00	-13.00	381.1
Left RNA	-60.0	-71.05	85.00	406.8
Right RNA	-60.0	71.05	85.00	406.8
Left Tower	-60.0	-53.50	36.96	342.5
Right Tower	-60.0	53.50	36.96	342.5
Left xy Bracing	-30.0	-20.00	0.00	214.6
Right xy Bracing	-30.0	20.00	0.00	214.6
Back Bracing	-60.0	0.00	0.00	307.1

Table 6: Floater centre of mass and buoyancy

Component	x [m]	y [m]	z [m]	Force [MN]
Centre of Mass	-40	0.0	10.71	59.87
Centre of Buoyancy	-40	0.0	-8.21	59.87

This calculation process is found to be effective in designs where the total required ballasting is equal to at least the weight of a single tower and RNA. This is because the buoyancy distribution of all three columns is the same, therefore in order to align the COB with the COM in the z-axis, each column needs to contribute equal parts to the mass distribution in the x-y plane.

Bearing this in mind, there are scenarios which require special attention. The first is where the floater possesses a mass-buoyancy equilibrium but is ballasted with less mass than is required to align the COM with the COB. The second is design combinations which do not possess a mass-buoyancy equilibrium.

In the first case the design is still feasible, however the misalignment will create a static pitch motion which needs to be considered in the motion characteristics.

The second scenario will result in a static heave displacement and a new draft equilibrium. Any designs with a static heave displacement cannot be considered. This is because any improvement in weight estimates for these designs will be a result of a reduced free-board rather than reduced draft. A reduction in free-board will also result in a reduction in hub height. These two variables are kept constant for all designs and will not be considered in the optimization, this is because the free board is a necessary buffer against dynamic

motions in heave and can be determined by interfaces with O&M procedures. In addition to this, the hub height is an important parameter for turbine manufacturer both for energy production and blade tip clearance.

Because of this, an investigation into the static pitch and heave displacements of floater designs is undergone. The results of which are presented in Section 7.3.

5.2.5 Radius of Gyration

The radius of gyration is calculated by finding the second moment of inertia of the floater. This is done by taking a weighted average of each components second moment of inertia as shown in Equation (112). The radius of gyration is then found using Equation (113) where r_r is the components perpendicular distance to the floaters COM. The calculated values for the same example used previously can be seen in Table 7. It is assumed each mass component acts as a point mass, this assumption is made because the distance between each mass component and the MUFP COM is large. It can therefore be assumed that $I << M \cdot r^2$ which simplifies the terms in the parallel axis theorem.

$$I_i = \sum_{r=1}^{n} M_r \cdot r_{r,i}^2 \cdot \frac{M_r}{M_t} \qquad for \quad i = xx, yy, zz \tag{112}$$

$$r_i = \sqrt{\frac{I_i}{M}} \qquad for \quad i = xx, yy, zz \tag{113}$$

Table 7: Radius of gyration

Component	x [m]	y [m]	z [m]	Mass [t]	I_{xx} $[kgm^2]$	I_{yy} $[kgm^2]$	I_{zz} $[kgm^2]$
Front Ballast	40.00	0.00	-24.16	859.2	1.88×10^9	5.02×10^8	1.37×10^9
Back Left Ballast	-20.00	-40.00	-24.67	63.8	6.43×10^7	1.41×10^8	1.28×10^8
Back Right Ballast	-20.00	40.00	-24.67	63.8	6.43×10^7	1.41×10^8	1.28×10^8
Front Column	40.00	0.00	-11.21	580.2	1.00×10^9	7.29×10^7	9.28×10^8
Back Left Column	-20.00	-40.00	-11.21	580.2	3.05×10^8	1.00×10^9	1.16×10^9
Back Right Column	-20.00	40.00	-11.21	580.2	3.05×10^8	1.00×10^9	1.16×10^9
Front Heave Plate	40.00	0.00	-23.71	381.1	8.24×10^8	2.14×10^8	6.10×10^8
Back Left Heave Plate	-20.00	-40.00	-23.71	381.1	3.67×10^8	8.24×10^8	7.62×10^8
Back Right Heave Plate	-20.00	40.00	-23.71	381.1	3.67×10^8	8.24×10^8	7.62×10^8
Left RNA	-20.00	-71.05	74.29	406.8	2.41×10^9	4.30×10^9	2.22×10^9
Right RNA	-20.00	71.05	74.29	406.8	2.41×10^9	4.30×10^9	2.22×10^9
Left Tower	-20.00	-53.50	26.25	342.5	3.73×10^8	1.22×10^9	1.12×10^9
Right Tower	-20.00	53.50	26.25	342.5	3.73×10^8	1.22×10^9	1.12×10^9
Left xy Bracing	10.00	-20.00	-10.71	214.6	4.61×10^7	1.10×10^8	1.07×10^8
Left xy Bracing	10.00	20.00	-10.71	214.6	4.61×10^7	1.10×10^8	1.07×10^8
Left xy Bracing	-20.00	0.00	-10.71	307.1	1.58×10^8	3.52×10^7	1.23×10^8
Radius of Gyration [m]					42.42	51.20	47.92

5.2.6 Product of Inertia

The product of inertia is calculated using Equation (114) where x_r, y_r, z_r represent the components distance in the x, y and z plane to the floaters COM.

$$
\begin{aligned}
I_{xy} &= \sum_{r=1}^{n} M_r \cdot x_r \cdot y_r \\
I_{yz} &= \sum_{r=1}^{n} M_r \cdot y_r \cdot z_r \\
I_{xz} &= \sum_{r=1}^{n} M_r \cdot x_r \cdot z_r
\end{aligned}
\tag{114}
$$

5.3 System Matrices

To ensure agreement between the desired HydroD simulation and executed simulation, the mass and stiffness matrix are calculated manually. The HydroD simulation is run centered at the still water level below the COB.

5.3.1 Mass Matrix

The mass matrix is constructed using Equation (115). Using the same example input variables used previously, namely 60 m, 80 m, 12 m 14 m for x_c, y_c, D_c and D_r respectively, an example mass matrix can be calculated, as seen in Equation (116).

$$
\hat{\boldsymbol{M}} = \begin{bmatrix}
M & 0 & 0 & 0 & M \cdot z_g & 0 \\
0 & M & 0 & -M \cdot z_g & 0 & 0 \\
0 & 0 & M & 0 & 0 & 0 \\
0 & -M \cdot z_g & 0 & I_{xx} & 0 & -I_{xz} \\
M \cdot z_g & 0 & 0 & 0 & I_{yy} & 0 \\
0 & 0 & 0 & -I_{zx} & 0 & I_{zz}
\end{bmatrix}
\tag{115}
$$

$$
\hat{\boldsymbol{M}} = \begin{bmatrix}
6.252 \times 10^6 & 0 & 0 & 0 & 5.682 \times 10^7 & 0 \\
0 & 6.252 \times 10^6 & 0 & -5.682 \times 10^7 & 0 & 0 \\
0 & 0 & 6.252 \times 10^6 & 0 & 0 & 0 \\
0 & -5.682 \times 10^7 & 0 & 1.198 \times 10^{10} & 0 & -8.330 \times 10^{11} \\
5.682 \times 10^7 & 0 & 0 & 0 & 1.741 \times 10^{10} & 0 \\
0 & 0 & 0 & -8.330 \times 10^{11} & 0 & 1.543 \times 10^{10}
\end{bmatrix}
\tag{116}
$$

5.3.2 Stiffness Matrix

The MUFP's stiffness in heave, pitch and roll is calculated analytically. The MUFP's stiffness in surge, sway and yaw are dependent on the mooring system. It is decided that the MUFP mooring system is outside the scope of the report, these stiffnesses are therefore accounted for using placeholder stiffnesses.

The heave stiffness is simply calculated as the additional water weight displaced per unit of heave. This equation is shown in Equation (117).

$$K_3 = 3 \cdot \rho_w \cdot A_c \cdot g \tag{117}$$

The stiffness terms in roll and pitch requires a longer calculation process. Firstly, the water plane moment of inertia is calculated using Equation (118). This equation sums the water plane moment of inertia of each of the columns about the COM using the parallel axis theorem. The water plane moment of inertia is then input into Equation (119) which calculates the distance between the COB and the metacentre. The distance between the COG and the metacentre is then calculated using Equation (120). Using Equation (121), the stiffness terms in roll and pitch can be calculated.

$$I_{wp,4/5} = \sum_{i=1}^{n} I_{c,i} + A_i h_i^2 \tag{118}$$

$$BM_{4/5} = \frac{I_{wp,4-5}}{V} \tag{119}$$

$$GM_{4/5} = BM_{4,5} + (z_b - z_g) \tag{120}$$

$$K_{4/5} = \rho_w \cdot g \cdot V \cdot GM \tag{121}$$

5.4 Hydrodynamic Coefficients

The MUFP's hydrodynamic coefficients are then simulated using the DNVGL suite. A finite element model (FEM) of the MUFP is generated in GeniE using a JavaScript input file. The FEM generated in GeniE only includes the three columns, any smaller drag components such as bracing are for the time being ignored as it is believed the inertia components of the large columns will dominate the response. The FEM model is then passed into HydroD, where the model's hydrodynamic coefficients are calculated. The process of generating and running these simulations is automated into the data pipeline.

Example outputs from the hydrodynamic analysis are plotted in Figures 22 to 24. Each plot shows influences of a split force. A split force occurs when a floater's columns experience opposite loading as a result of their positioning along a wave length. An illustration of this can be seen in Figure 21. The positioning of the columns along the wave length means each column experiences the in-coming waves at a different phase. At certain frequencies, the phase difference between the columns causes them to experience equal and opposite loading. When this occurs, the net force acting on the floater is low, while the internal loads are high.

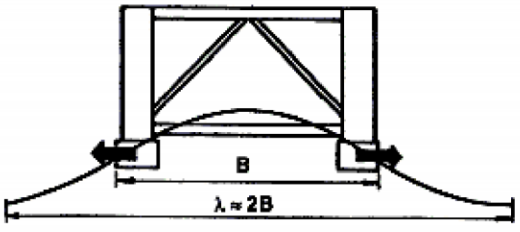

Figure 21: Diagram depicting split force between columns [39].

To highlight the influence of this, each plot includes pink and cyan dashed lines that are drawn at wave lengths which are factors of the column separation. The pink is calculated using y_c and the cyan using x_c, note that frequencies at which these lines overlap appear purple. At these frequencies, and in the case of head-on loading, the front and back columns experience the wave at the same phase. As a result, there is no split force at these frequencies and the forces acting on each of the columns is purely constructive. The calculation used to find these frequencies is based on Airy-wave theory and can be seen in Equation (122). Only frequencies calculated to be between 0.5 rad/s and 2.5 rad/s are plotted to minimise clutter.

$$\left.\begin{aligned} L_{w,i} &= \frac{x}{i} \\ k_{w,i} &= \frac{2\pi}{Lw,i} \\ \omega^2 &= g \cdot k_{w,i} \cdot \tanh\left(k_{w,i} \cdot h\right) \end{aligned}\right\} \text{for i = 1...20, where } x = x_c \text{ and } y_c \tag{122}$$

5.4.1 Added Mass

To start, the translation-translation plots in Figure 22 are considered. It can be seen that the heave value of added mass remains steady irrespective of frequency, while coupling terms between the translations are insignificant. What is interesting is the large fluctuations in the A_{11} and A_{22} between 0.9 rad/s and 3 rad/s. The peaks can first be seen to align with the y_c "in-phase" frequencies, however past 1.5 rad/s the peaks can be seen to align more with the x_c "in-phase" frequencies.

A review of the rotation-rotation plots show little variation in the roll and pitch degrees of freedom. It can also be seen that coupling terms are again negligible. The yaw degree of freedom shows a similar trend to that seen for the surge and sway plots in the previous graph, with peaks occurring at "in-phase" loading frequencies.

The plot showing the rotation-translation coupling terms reveals a strong coupling between surge-pitch and sway-roll. Both these plots show peaks at around 1 rad/s before easing into a trough and leveling off beyond 2.5 rad/s. This trend is again similar to the relationships shown in the previous plots. What is interesting in this graph is the yaw-sway coupling term. The plot shows large fluctuations about 0 $kg \cdot m^2$. The plot is also shown to consistently equal 0 $kg{\cdot}m^2$ when loading is in-phase with the x_c column separation, however tends to display peaks in y_c in-phase loading.

The last plot shows the translation-rotation coupling. This plot is identical to the previous. This is to be expected due to the symmetry of the matrices.

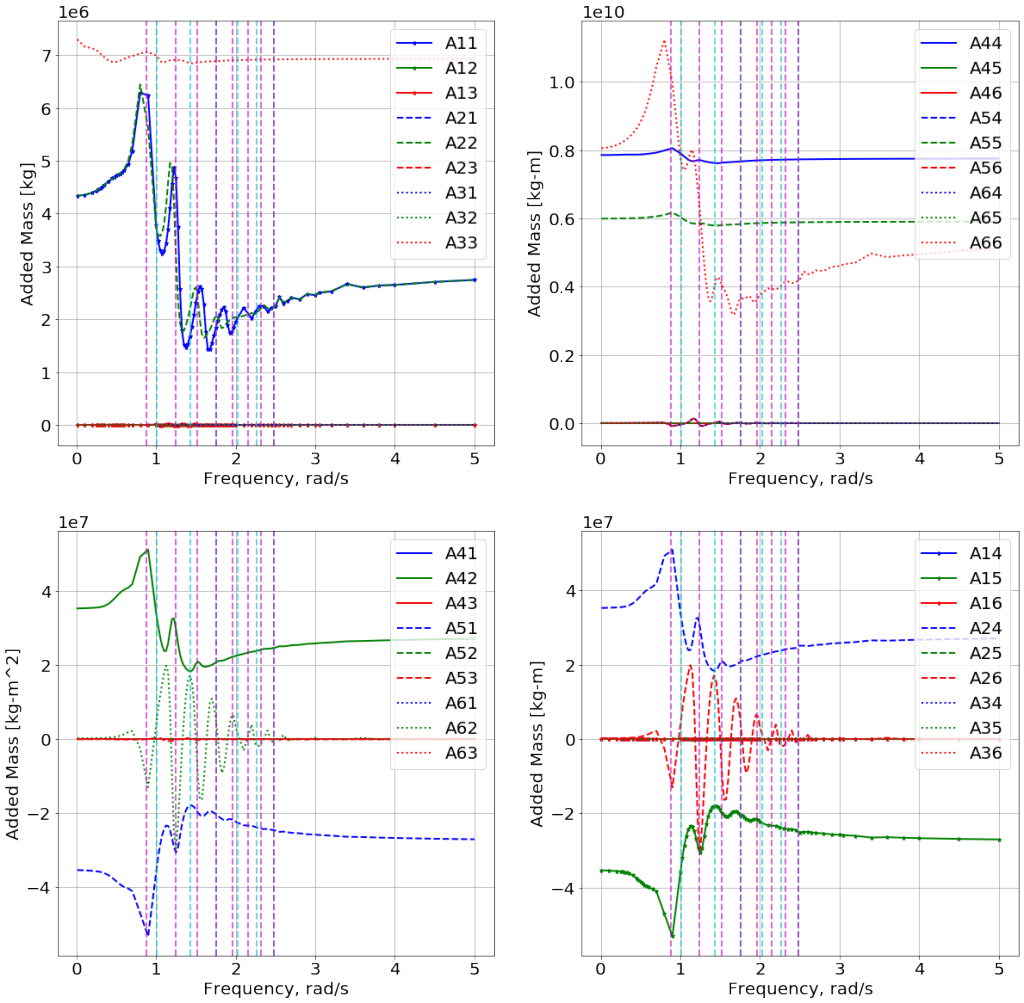

Figure 22: HydroD added mass output. (In-phase y_c = pink, in-phase x_c = cyan)

5.4.2 Damping

A review of the translation-translation plots in Figure 23 shows that the surge-surge and sway-sway damping value start from 0.5 rad/s before entering a peak, and tailing off towards 5 rad/s. Within this trend, the damping displays peaks and troughs. In the 1 rad/s to 1.5 rad/s region, the peaks coincide with the y_c in-phase frequencies while the troughs align with the x_c in-phase frequencies. When approaching 2 rad/s, this relationship becomes less pronounced as the peaks and troughs fall between the frequencies. Past 2 rad/s the inverse trend is shown, where peaks occur at x_c in-phase frequencies and troughs at y_c in-phase frequencies. Damping in heave is shown to be relatively small compared to the values in surge and sway. The drop to zero damping for all plots is currently an unexplained phenomena.

Looking at the plots displaying the rotation-rotation damping values it is clear yaw hold the most significant value. The damping values for pitch-pitch and roll-roll are less influenced by the phases and are an order of magnitude smaller than that of yaw-yaw. A small quantity of roll-sway coupling can also be seen. This is shown to oscillated about 0.

The rotation-translation in the bottom left of Figure 23 shows a similar trend to that of the rotation-translation added mass plots. A clear roll-sway and pitch-surge coupling is displayed. The pitch-surge plot displays a maximum negative damping peaking at 1.05 rad/s before decreasing. A small peak is shown at approximately 1.5 rad/s at a in-phase frequency however remains relatively unaffected. The roll-sway displays a similar trend however shows a stronger influence of in-phase loading. The roll-sway displays a peak at approximately 1.05 rad/s before trailing off, unlike pitch-surge a small peak is shown at each in-phase frequency. This relationship between the yaw-sway coupling is striking. The coupling term displays large oscillations about 0 kgm/s. The peaks and troughs of these oscillations coincide with both the x_c and y_c in-phase frequencies however do not show a clear dependence on either the x_c and y_c in-phase frequencies.

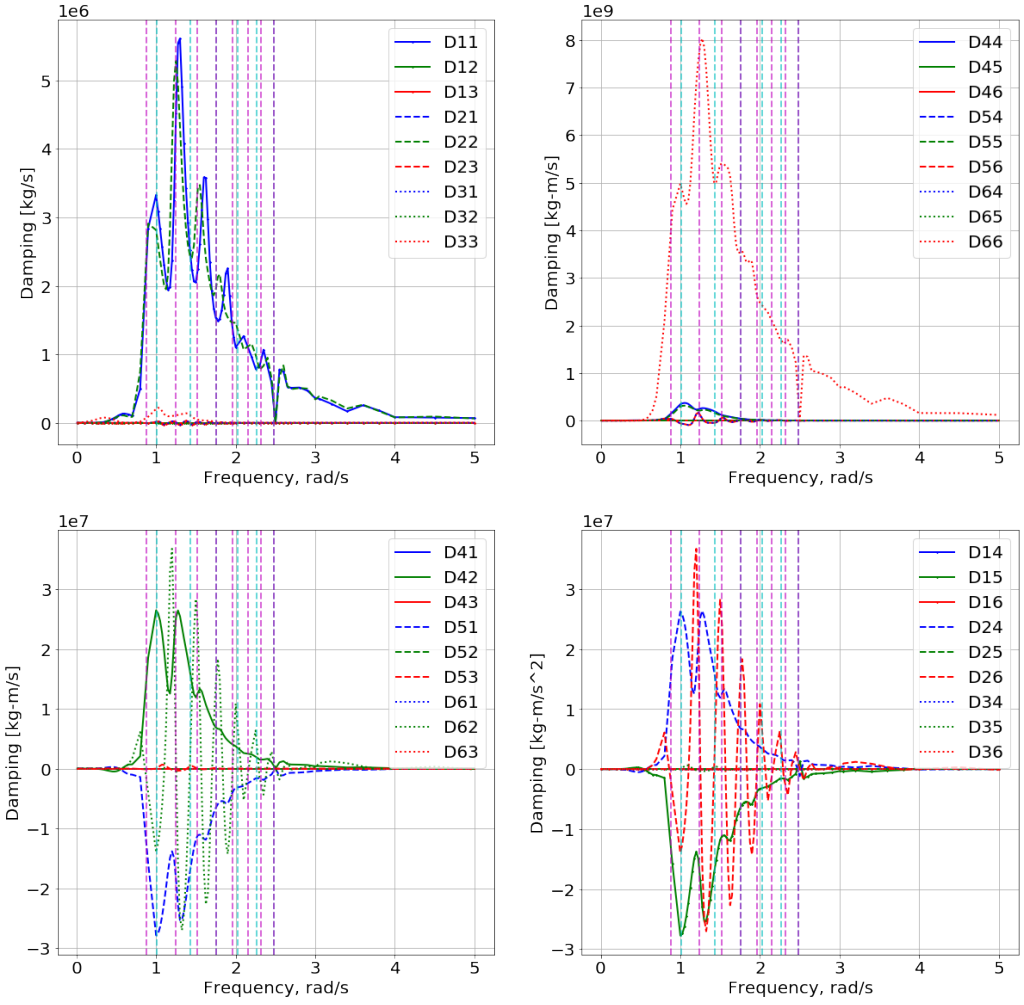

Figure 23: HydroD potential flow damping output. (In-phase y_c = pink, in-phase x_c = cyan)

5.4.3 Excitation

The final output is the excitation force on the floater as a function of frequency. This can be seen in Figure 24. It can clearly be seen that the force is highly influenced by the

in-phase loading. plots show distinct peaks at the x_c in-phase frequencies and troughs at the y_c in-phase frequencies.

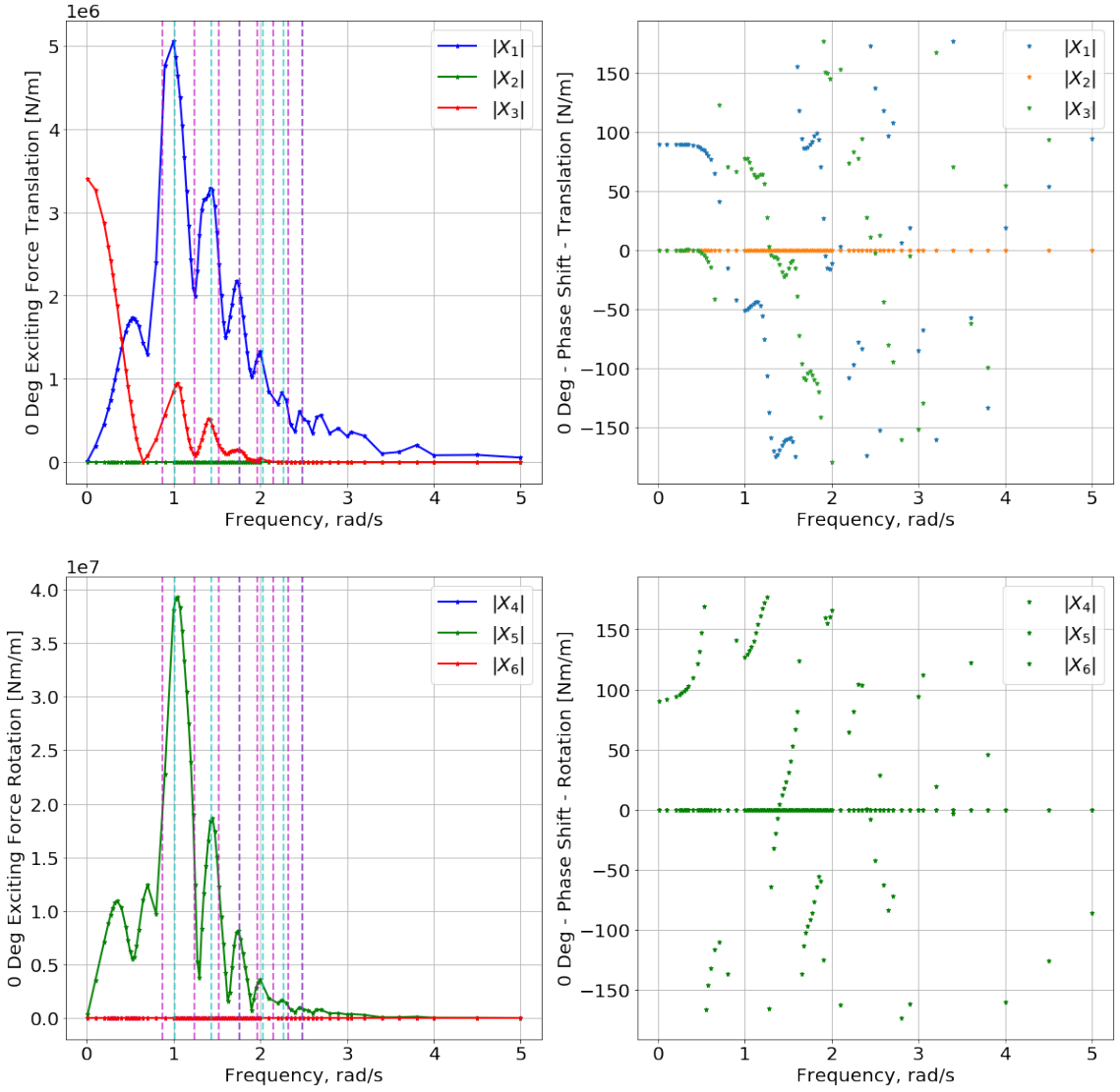

Figure 24: HydroD excitation force output. (In-phase y_c = pink, in-phase x_c = cyan)

5.5 Interpolating Hydrodynamic Coefficients

In order to improve computational efficiency it is decided that rather than running a unique HydroD simulation for each iteration of the optimization, the hydrodynamic coefficients of the floater would be calculated at interval throughout the design space. The optimizer would then be able to load pre-existing simulations and interpolate between them. The hydrodynamic simulations can therefore be used as a surrogate model.

HydroD simulations are run for all design combinations in a discretized grid. This grid is defined by intervals of 10 m in x_c and y_c, every 1 m for column diameter and every 2m for draft. The hydrodynamic coefficients are then found for a point within the discretized

grid through a four way linear interpolation using the 16 surrogate models surrounding the design.

The interaction between wave length and column separation has implications for the accuracy of interpolating between HydroD separations. An example interpolation is shown in Figure 25. Figure 25 displays hydrodynamic coefficients calculated by interpolating between surrogate models in addition to a HydroD simulation. The hydrodynamic coefficients were calculated for a design with input variables: x_c = 55m, y_c = 55 m, D = 12.5 m, Dr = 13.5m.

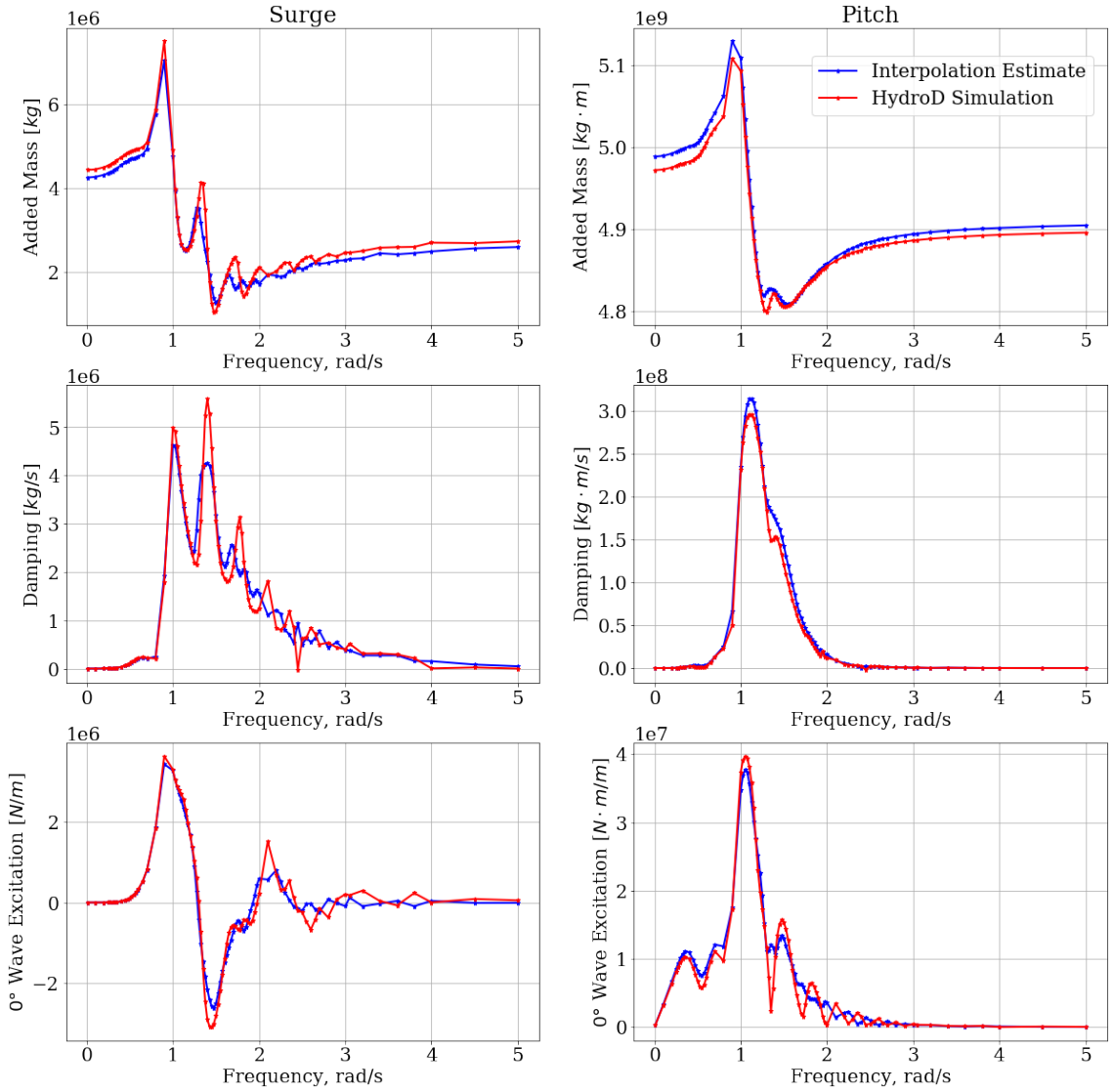

Figure 25: Comparison between interpolated hydrodynamic coefficients and HydroD output.

Overall it can be seen that interpolating between surrogate models gives a good estimate of the hydrodynamic coefficients at a fraction of the computational time. What is evident is that the peaks and troughs between the simulations are not captured in the interpolation

process. The differences in peaks is shown to be most pronounced between 1.5 rad/s and 2 rad/s. With the knowledge that the system natural frequencies will lie below this frequency range, it is not foreseen that this will have an influence on the model.

5.6 Critical Damping

The use of a potential flow solver only considers inviscid damping. A simple approximation for viscous damping is to add 5% critical damping to the system. Published model test data on the WindFloat, a semi-submersible of comparable geometry to the MUFP, found the necessary fraction of critical damping needed to align experimental data with numerical models to lie between 7% and 12 %. The 5% estimate is therefore likely to provide conservative rigid body motions [49].

In order to add this to the system, critical damping is found using Equation (123), where $\bar{A}$ is the added mass at the smallest HydroD frequency evaluation, in this case 0.01 rad/s. 5% of this critical damping is added to the the potential flow damping as shown in Equation (124).

$$c_{crit}(\omega) = 2\sqrt{\bar{K} \cdot \left(\bar{M} + \bar{A}\right)} \tag{123}$$

$$\bar{B}(\omega) = \bar{B}(\omega) + \frac{1}{20} \cdot c_{crit}(\omega) \tag{124}$$

5.7 Aerodynamic Damping

The aerodynamic damping exerted on the floater by the two turbines needs to be accounted for. The aerodynamic damping can be approximated by the change in thrust force applied by the turbines for small changes in wind speed while maintaining all control system parameters [48].

This technique is implemented by running simulations on the NREL 5MW turbine in FAST for a range of wind speeds. For each wind speed, two additional simulations are run at $\pm 0.25 m/s$ while maintaining the turbine's control parameters. These simulations were run by Erin Bachynski-Polić [48]. The thrust force for each simulation can be seen in Figure 26.

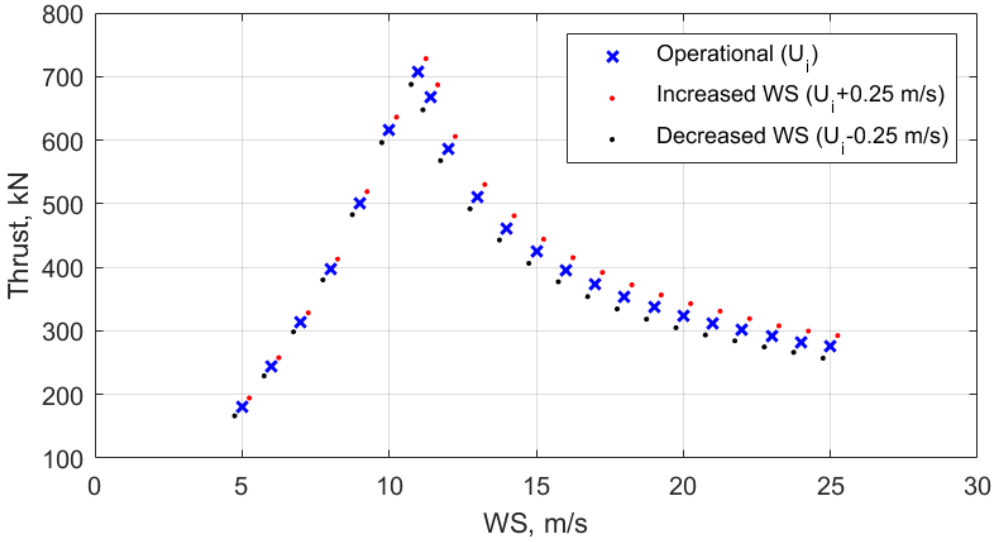

Figure 26: Thrust force for aerodynamic damping calculations and aerodynamic damping ratio for the NREL 5 MW land-based turbine [48]

This report follows the frequency domain testing of a MUPF at rated wind speed which will be explained in more detail in Section 6.1.1. The change in thrust force per unit wind speed ($\frac{dF_t}{dU}$) at 11.4 m/s is found to be $7.88 \times 10^4 N$. This damping as applied to the surge, pitch and yaw degrees of freedom as shown in Equation (125).

$$\boldsymbol{B_{aero}} = \begin{bmatrix} 2 \cdot \frac{dF_T}{dU} & 0 & 0 & 0 & 2 \cdot \frac{dF_T}{dU} \cdot h_{hub} & 0 \\ 0 & 0 & 0 & 0 & 0 & 0 \\ 0 & 0 & 0 & 0 & 0 & 0 \\ 0 & 0 & 0 & 2 \cdot \frac{dF_T}{dU} \cdot h_{hub}^2 & 0 & 0 \\ 2 \cdot \frac{dF_T}{dU} \cdot h_{hub} & 0 & 0 & 0 & 0 & 0 \\ 0 & 0 & 0 & 0 & 0 & 2 \cdot \frac{dF_T}{dU} \cdot y_{rna}^2 \end{bmatrix} \tag{125}$$

5.8 Equations of Motion

Using the HydroD outputs paired with the hand calculations for the system mass and stiffness matrices, all components of the floaters equations of motion are known. This can be expressed as shown in Equation (126).

$$(\mathbf{M}+\mathbf{A}(\omega))\ddot{x} + \mathbf{B}(\omega)\dot{x} + \mathbf{K}x = \mathbf{F}(\omega) \tag{126}$$

By assuming a sinusoidal response and deriving the corresponding functions for velocity and displacement, as shown in Equation (127), the equations of motions can be converted into the frequency domain. This is shown in Equation (128).

$$\begin{aligned} x =& X \cdot \sin(\omega t) \\ \dot{x} =& X\omega \cdot \cos(\omega t) \\ \ddot{x} =& -X\omega^2 \cdot \sin(\omega t) \end{aligned} \tag{127}$$

$$-(\mathbf{M}+\mathbf{A}(\omega)) \cdot X \cdot \omega^2 + i\mathbf{B}(\omega) \cdot X \cdot \omega + \mathbf{K} \cdot X = \mathbf{F}(\omega) \tag{128}$$

5.9 Mechanical Transfer Function

The system transfer function denoted by H_{FX} is shown in Equation (130). This equation retains the real and imaginary components of the loading. The absolute value of the transfer function is therefore taken when plotting RAOs.

$$Y = -(\mathbf{M} + \mathbf{A}(\omega)) \cdot \omega^2 + i\omega \cdot \mathbf{B}(\omega) + \mathbf{K} \tag{129}$$

$$H_{WX} = Y^{-1}\mathbf{F} \tag{130}$$

As an exercise to validate the calculation process, the transfer function derived above is used to plot the MUFP's Response Amplitude Operator (RAO) in each of the degrees of freedom. These plots are compared against the HydroD generated RAOs. The comparison can be seen in Figure 27. It can clearly be seen that the two calculation processes share agreement with small differences occurring at resonance frequencies. These discrepancies will be a result of small differences in mass and stiffness.

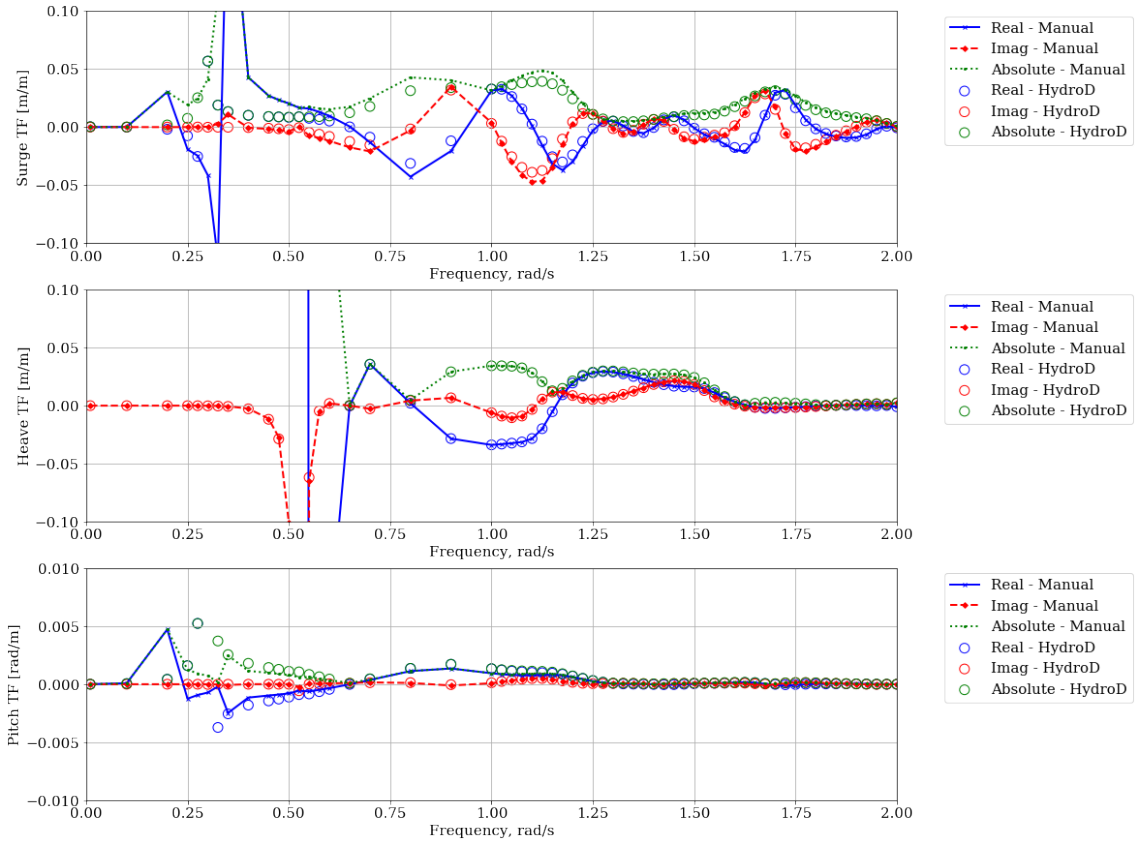

Figure 27: HydroD RAO output and transfer function.

6 Loading Scenarios

The MUFP configuration is tested against two dynamic loading scenarios including wind and wave excitation design to mimic realistic load cases for a weathervaning platform.

6.1 Hydrodynamic Loading

The wave excitation is applied using the JONSWAP spectrum, the theory of which is described in Section 4.3.1. The significant wave height, time period and the scaling parameter γ are taken as $H_s = 6.5$ m, $T_p = 14$ s and $\gamma = 3.3$. These values were taken based on a report published by Lin Li et al. in which sea-states with a 50 year return period were calculated based on joint environmental data [45]. The data corresponded to a site positioned in the North Sea off the Norwegian coast. The parameters were taken as the largest significant wave height and longest time period observed at wind speeds equal to 11.4 m/s. The decision was based on the knowledge that the eigenfrequencies of the system lie in the low frequency range, this combination will therefore act as the worst-case loading scenario.

6.1.1 Aerodynamic Force Spectrum

The aerodynamic loading on a MUFP requires the consideration of two turbines. The two turbines will experience the same wind field but at different points. It is therefore expected that although large low frequency fluctuations will be felt by the two turbines simultaneously, smaller high frequency fluctuations will not.

To investigate this dynamic a large wind field of dimensions 280m x 200m is generated in TurbSim. The wind field is generated using a mean wind speed of 11.4 m/s and a Kaimal distribution. Using this wind field, two individual SIMA simulations are run. In the first the turbine is placed at the coordinates of the floater's right turbine, and in the second it is placed at the coordinates of the floater's left turbine. The two thrust force time series can be seen in Figure 28.

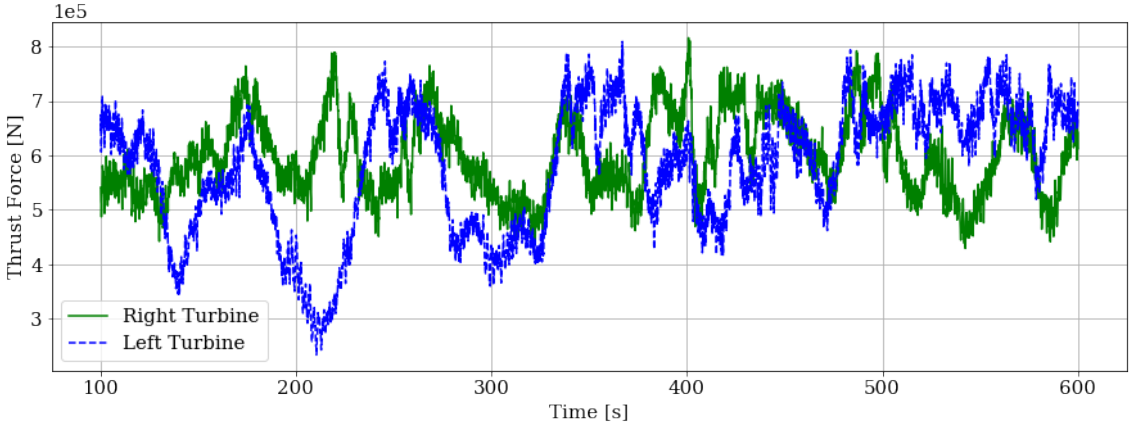

Figure 28: Wind force time series generated in SIMA.

It can be seen that both time series fluctuate about a constant thrust force while displaying smaller high frequency fluctuations unique to each turbine.

In order to investigate interference between the two turbines, the Power Spectral Density (PSD) of the sum of the two thrust force time series is taken, this is compared against the PSD of a single thrust force time series multiplied by two. The results to this are shown in Figure 29. In this report the SciPy Welch function is used to obtain the PSDs.

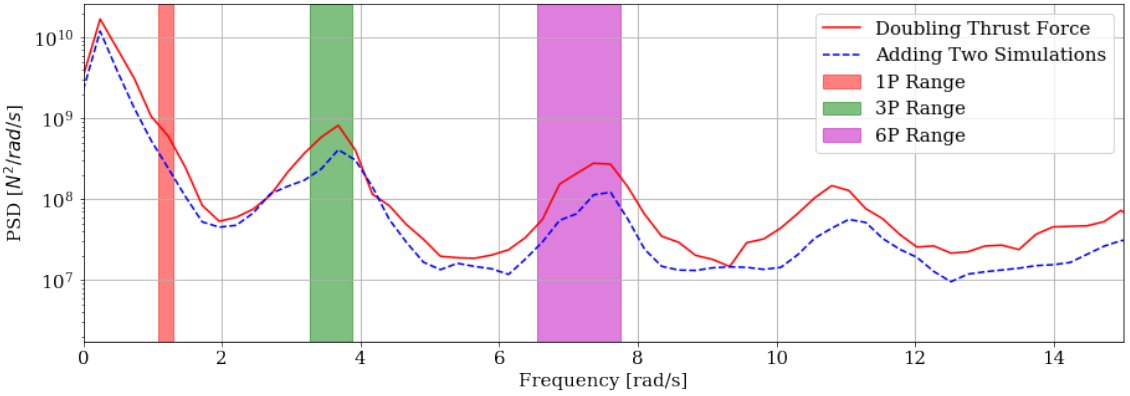

Figure 29: Wind force power spectral density.

It can be seen that the two calculation methods follow a similar trend, both plots show the majority of energy lying in the low frequency range with peaks occurring periodically as frequency increases. Using the rotor rotational speed time series calculated by SIMA, it can be seen that these peaks correspond with the blade passing frequencies. These regimes are highlighted in Figure 29.

A comparison between the plots shows that the two plots diverge at higher frequencies. This shows that the low frequency energy such as wind gusts is felt similarly between the turbines while thrust force generated from high frequency energy is more prone to experiencing destructive interference.

Ultimately, the majority of the floaters rigid body response will be dictated by excitation of the platform in the 0 rad/s to 5 rad/s region and at the floaters natural frequencies. Therefore the divergence in plots in the high frequency ranges will not translate to any observable changes to the model response output. However, under a more advanced model including components with higher natural frequencies this observation may influence fatigue calculation.

6.1.2 Aerodynamic Moment Spectrum

The two turbine design also induces a moment about the z-axis (M_z). Each turbine acts at a distance of 71.05 m from the center of mass in the y-axis. Each turbine inflicts a moment on the floater in opposite directions however the force time series acting on each turbine is not equal. As a result of this, the floater will experience excitation due to a net moment.

The calculation of this net moment uses the same SIMA simulations as used for the thrust force time series. The moments acting on the floater are found by multiplying the force time series by each of the turbine's y coordinates. The net moment time series acting on the system is found by summing the two moments. All three time series can be seen in Figure 30a. The PSD of the net moment time series can be seen in Figure 30b.

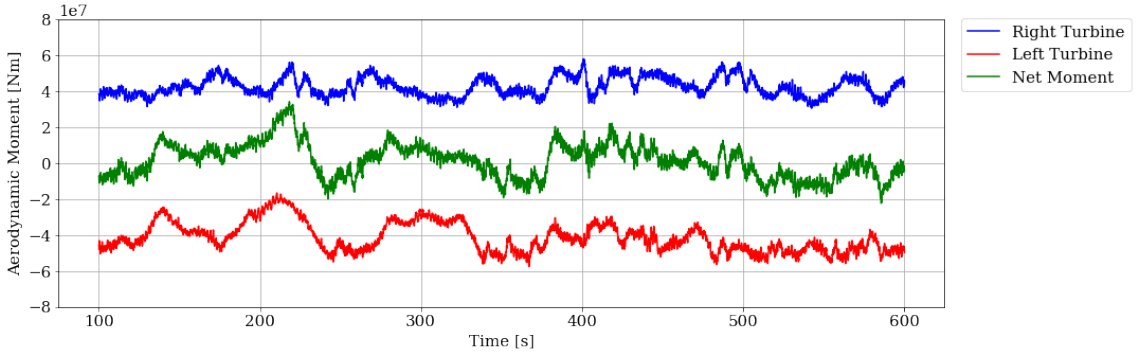

(a) The left and right turbine moment (M_z) time series plotted alongside the net moment time series.

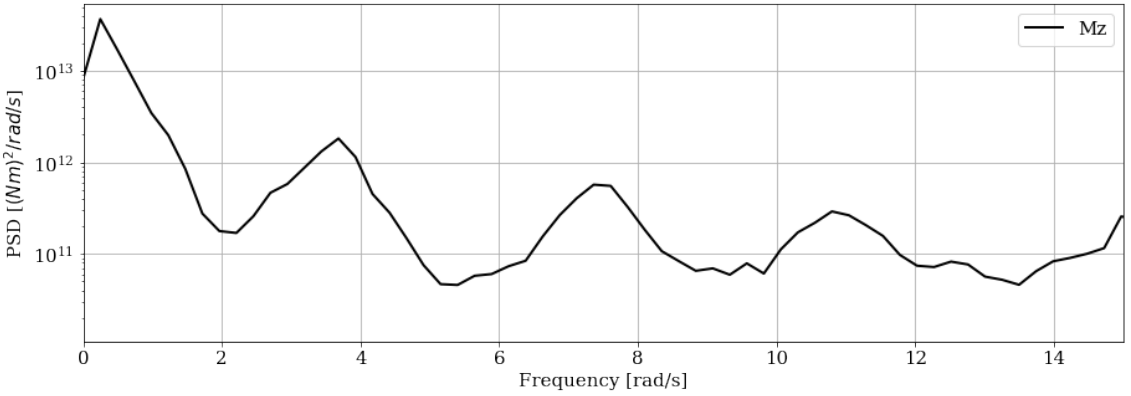

(b) The power spectral density of the net moment time series.

Figure 30: The M_z timeseries and PSD at rated wind speed.

6.1.3 Aerodynamic Transfer Functions

The aerodynamic transfer function is found using a similar process to the one used for the wave loading. The transfer function per unit force is found using Equation (131), where Y is defined as shown in Equation (129) and F is defined in Equation (132).

$$H_{WX}(\omega) = Y(\omega)^{-1} \cdot F \tag{131}$$

$$F = \begin{bmatrix} 1 \\ 1 \\ 1 \\ h_{hub} \\ h_{hub} \\ 1 \end{bmatrix} \tag{132}$$

6.2 Dynamic Load Cases

A visualisation of the two load cases used to mimic realistic load cases for a weathervaning platform can be seen in Figure 31.

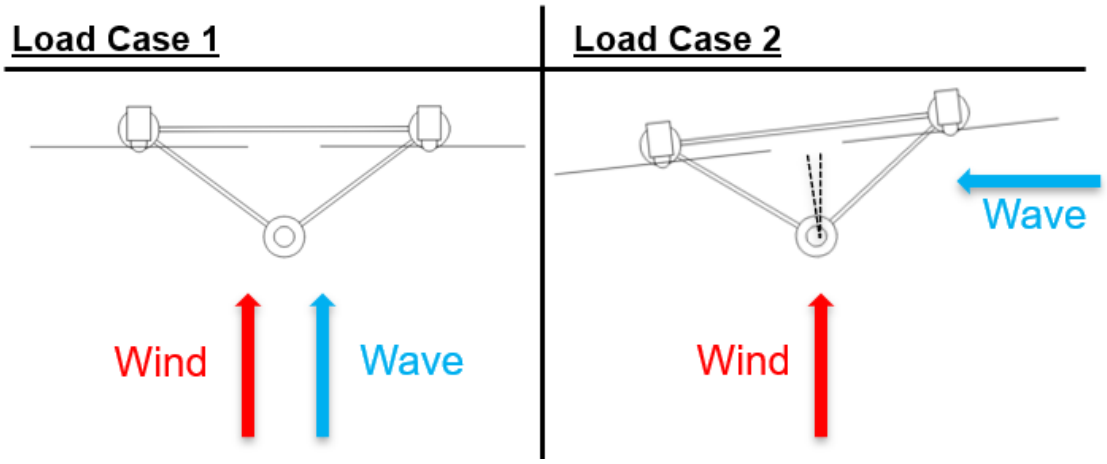

Figure 31: Model load cases.

In the first scenario, the structure is excited head-on using uni-directional wind and wave loading. The MUFP response spectrum due to hydrodynamic loading is calculated using Equation (70), where the JONSWAP load spectrum is multiplied by the MUFP RAOs in surge, heave, pitch and yaw squared. The response spectrum of the floater due to aerodynamic loading is calculated by multiplying the aerodynamic thrust force PSD by the floater's aerodynamic transfer function in surge and pitch squared. Finally, the response spectrum in yaw is found by multiplying the aerodynamic moment PSD by the MUFP yaw RAO squared. The hydrodynamic and aerodynamic load spectra for load case one, labelled $S_{H1}(\omega)$ and $S_{A1}(\omega)$ respectively, can be seen in Equation (133)

$$S_{H1}(\omega) = \begin{bmatrix} S_{JS}(\omega) \\ 0 \\ S_{JS}(\omega) \\ 0 \\ S_{JS}(\omega) \\ S_{JS}(\omega) \end{bmatrix} \quad S_{A1}(\omega) = \begin{bmatrix} F_w(\omega) \\ 0 \\ 0 \\ 0 \\ F_w(\omega) \\ M_{w,z}(\omega) \end{bmatrix} \tag{133}$$

The second scenario aims to test the floaters response to perpendicular wave loading with a slight yaw misalignment. This load case aims to mimic sea states in which the direction of the wind-waves lag behind a directional changes in the wind. In this scenario the turbines are imagined to hold a 3 ° yaw relative to the wind.

The response spectra of the platform due to hydrodynamic loading are calculated by applying the JONSWAP spectrum to the MUFP RAOs in sway, heave, roll and yaw. The aerodynamic loading is applied to the surge, pitch and yaw degrees of freedom in the same way it was accounted for in load case one, however load case two also includes the perpendicular component of the aerodynamic thrust force in the sway and roll degrees of freedom. The hydrodynamic and aerodynamic load spectra for load case two, labelled $S_{H2}(\omega)$ and $S_{A2}(\omega)$ respectively, can be seen in Equation (134)

$$S_{H2}(\omega) = \begin{bmatrix} 0 \\ S_{JS}(\omega) \\ S_{JS}(\omega) \\ S_{JS}(\omega)) \\ 0 \\ S_{JS}(\omega) \end{bmatrix} \quad S_{A2}(\omega) = \begin{bmatrix} F_w(\omega) \\ F_w(\omega) \cdot \theta \\ 0 \\ F_w(\omega) \cdot \theta \\ F_w(\omega) \\ M_{w,z}(\omega) \end{bmatrix} \tag{134}$$

7 Design Space

The next section will discuss the optimization design space. This will include justification of the optimization bounds and constraints in addition to a review of the floater's motion characteristics as a function of its design variables. Special consideration will be paid to ensuring that the interface between the model and the optimizer remains robust throughout the design space.

7.1 Bounds

The data pipeline for the model is reliant on the existence of pre-existing surrogate models to interpolate hydrodynamic coefficients from. The design space in which the optimizer can operate therefore needs to be determined beforehand.

The first variable bound is the column diameter. The column diameter ranges were determined based on the parametric study on tower inclination and column separation conducted by I. Udoh [27]. The published paper reviews column diameters ranging from 10m to 12m for a similar floater design. Using this as a guide, it was decided this paper would review column diameters ranging from 11m to 13m.

The draft bounds were determined based on the mass buoyancy equilibrium. Using the column diameters above, it was calculated that the floater could be buoyant with drafts as low as 8m. The upper bound was determined to be 16m. Drafts beyond this point would require excessive ballasting to reach equilibrium, something which is indicative of a bad design.

Lastly, the column separation bounds were set between 30m and 90m. A review of the stiffness parameter in pitch using combinations of column diameter and draft found that column separations below approximately 40m separation held negative stiffness and were therefore unstable. It is therefore known that the optimum spacing based on the column diameter and draft bounds cannot lie below this lower bound. The upper bound was set under the assumption that column separations beyond this distance would be an inefficient use of resources leaving the system with excessive stiffness in pitch and roll.

7.2 Constraints

The objective function of the optimization is to minimise the weight of steel in the system. The logical approach of the optimizer is therefore to reduce all design variables to their lower bounds to the detriment of the response characteristics.

In order to ensure the optimizer solution maintains suitable operating conditions under environmental loading, two inequality constraints are placed on the pitch and roll response of the floater. The wind turbine operating conditions would ultimately be determined by the turbine manufacturer and may vary, however a commonly used estimate sets this limit to 10° rotation [46; 47]. This constraint is set on the sum of the static rotation and the most probably maxima (MPM) rotation in pitch and roll.

A final inequality constraint is set on the static heave displacement. This inequality constraint ensures that the static heave displacement does not fall below zero.

7.3 Static Displacement

As mentioned previously, the design space includes variable combinations which do not satisfy the mass-buoyancy equilibrium. A configuration which does not satisfy this equilibrium cannot be considered in the optimization. The static heave of a floater is calculated in Equation (135).

$$x_3 = \frac{m \cdot g - b \cdot g}{K_{3,3}} \tag{135}$$

This calculation is run for 9 cuts through the design space, the results to this are presented in Figure 32. As expected, the magnitude of static heave increases as the column separation increases. This is because the increased bracing causes the floater mass to surpass its buoyancy. The presence of static heave displacement can be seen in all combinations of column diameter and draft.

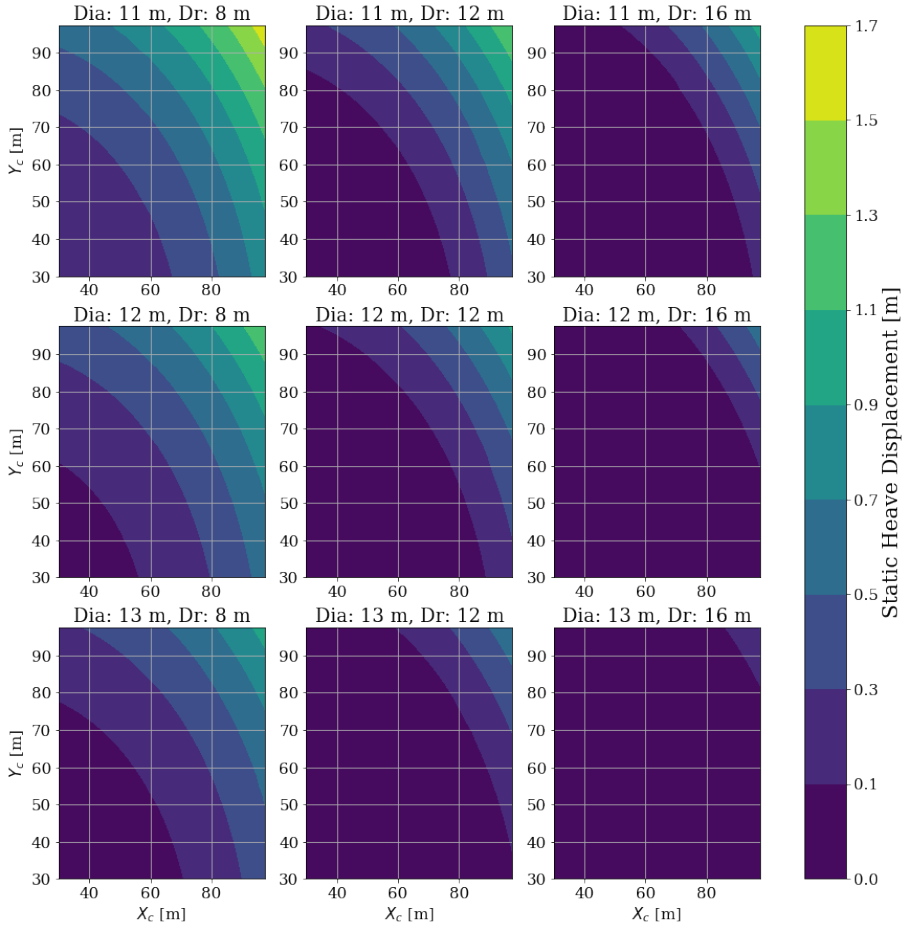

Figure 32: Static heave displacement contour plots

The static pitch rotation can be calculated using Equation (136). The static pitch rotation is presented for 9 cuts through the design space. This is shown in Figure 33. In order to

maintain readability of the contour plot scale, any static rotation calculated above 20 degrees is capped to 20 degrees. Any rotation higher than this is indicative of a configuration being unstable or on the brink of instability.

$$x_{s,5} = \frac{B \cdot (COM_x - COB_x)}{K_{5,5}} \tag{136}$$

What is most striking about Figure 33 is how stark the contrast between stable and unstable regions is. This is shown by the rapid increases in static pitch rotation at approximately 40m column separation in the x axis. This indicates that a static pitch deflection is only of significance for floater configurations with very low pitch stiffness.

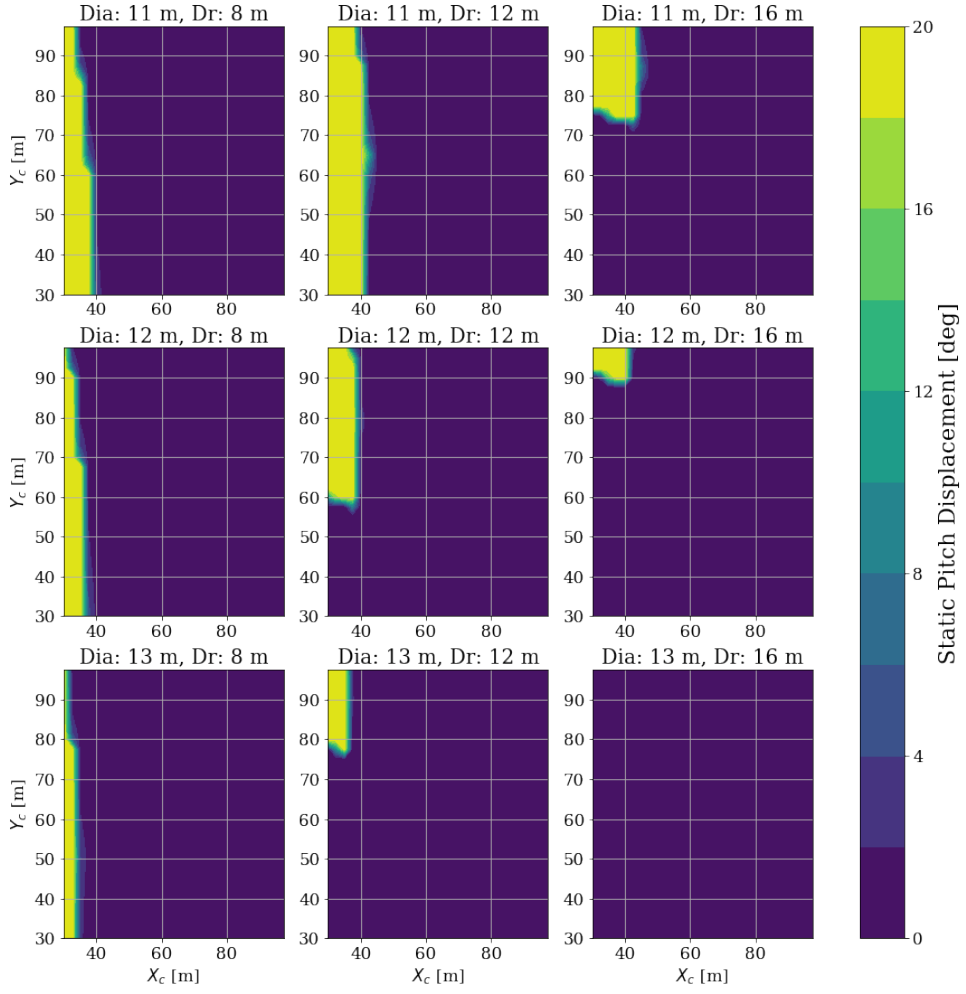

Figure 33: Static pitch displacement contour plots

It can also be seen that large y_c has a negative influence on the static pitch behaviour of a design. This is because increasing the value of y_c increases the bracing mass at the back of the platform and as a result, the platform's un-ballasted COM moves further back. The increased un-ballasted mass reduces the required ballasting meaning that at the extremes,

the configuration is unable to correct itself resulting in a moment arm between the COM and COB.

In the context of the report, is is clear static pitch is of little importance. It can be seen that the rotation is only a problem where the floater is unstable. Any configuration in proximity of large static pitch deflection will not be able to maintain appropriate operating conditions under aerodynamic loading.

7.4 Negative Stiffness

The design space also contains variable combinations resulting in negative restoring forces in pitch and roll. This is exemplified in Figure 34, where the restoring force in pitch is plotted as a function of x_c. As the column separation decreases, the MUFP metacentre lowers and the restoring force is reduced. Once the metacentre falls below the centre of mass the floater becomes unstable. The stiffness calculation process is conducted assuming small angle deflections, therefore as the stiffness turns negative that calculation loses its physical significance.

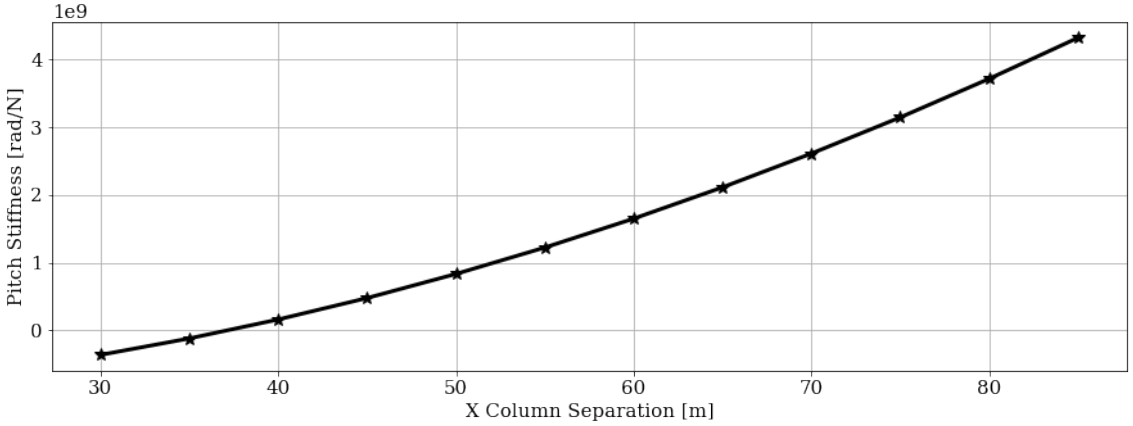

Figure 34: Hydrostatic stiffness in pitch as a function of x_c.

The influence of this instability on the calculation process is shown by the floaters mechanical transfer function in pitch for increasing x_c in Figure 35. The plot reveals two peaks for values of x_c above 34 m. Each of the peaks is located at the eigenfrequency in pitch and surge.

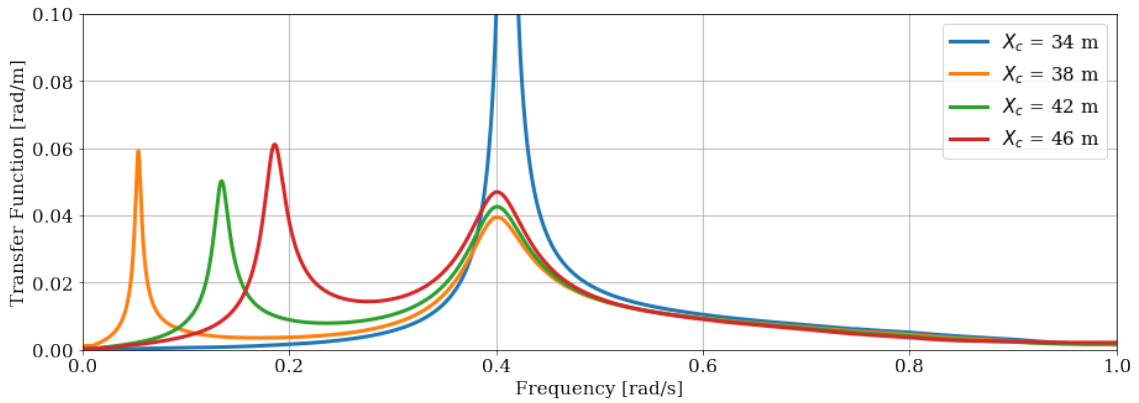

Figure 35: Wave excitation transfer function in pitch under head-on loading for increasing x_c.

As the pitch stiffness decreases the pitch eigenfrequency tends to smaller values. Once the stiffness turns negative the natural frequency becomes imaginary. Therefore, much like the stiffness, the eigenfrequency loses its physical significance. As a result, the unstable x_c plot only shows a single peak corresponding the to surge natural frequency.

At these extremes the physical significance of the calculation process breaks down with the linear approximations no longer able to model the floater's true motion. The pitch/roll mechanical transfer functions experience no excitation at the non-existant pitch and roll eigenfrequencies which results in a smaller response spectrum and reduced spectral moments. The calculation process therefore returns small MPM values capable of passing the optimization constraints.

The impact of this can be seen in Figure 36 for a MUFP defined by $y_c = 60$m, $D = 12$m and $D_r = 14$m. As the value of x_c falls below 37m, the pitch stiffness turns negative and the MPM rotation in pitch is dramatically reduced.

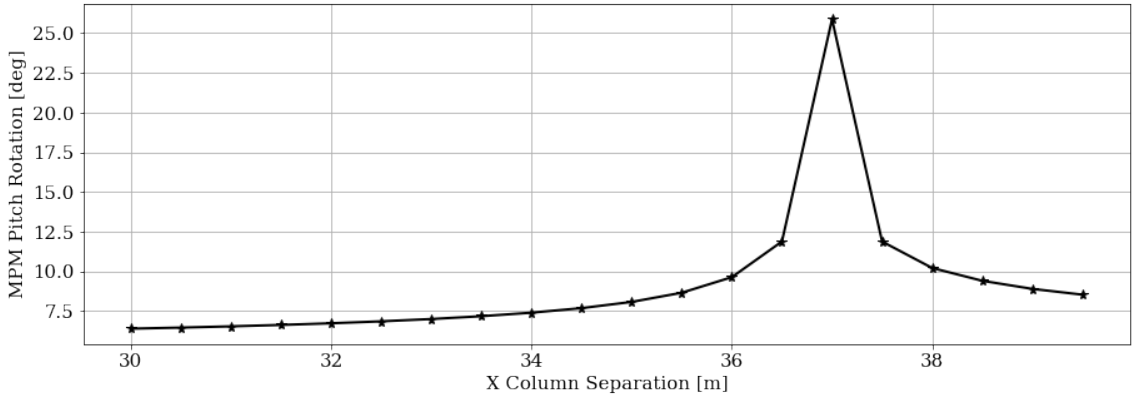

Figure 36: MPM Pitch rotation as a function of x_c as the MUFP passes into instability.

This observation requires adjustments to the model to artificially penalise unstable design configurations in order to improve the interface between the optimizer and the model. The correction is required to offer the optimizer a slope back to the stable region while

satisfying the SLSQP requirement for the MPM constraint function to be continuous and twice differentiable.

The correction implemented is shown in Equation (137). The correction is imposed on designs just before they reach instability. The correction ensures the optimizer is given a continuous function which increases the value of the MPM as the optimizer approaches the lower bound. The consequent pitch stiffness as a function of x_c can be seen in Figure 37

$$\begin{array}{ll} \text{For} & K_{5,5} < 1 \times 10^7 \\ K_{5,5} & = 1 \times 10^7 - 5 \times 10^6 \cdot \left(\frac{60 - x_c}{30}\right) \end{array} \tag{137}$$

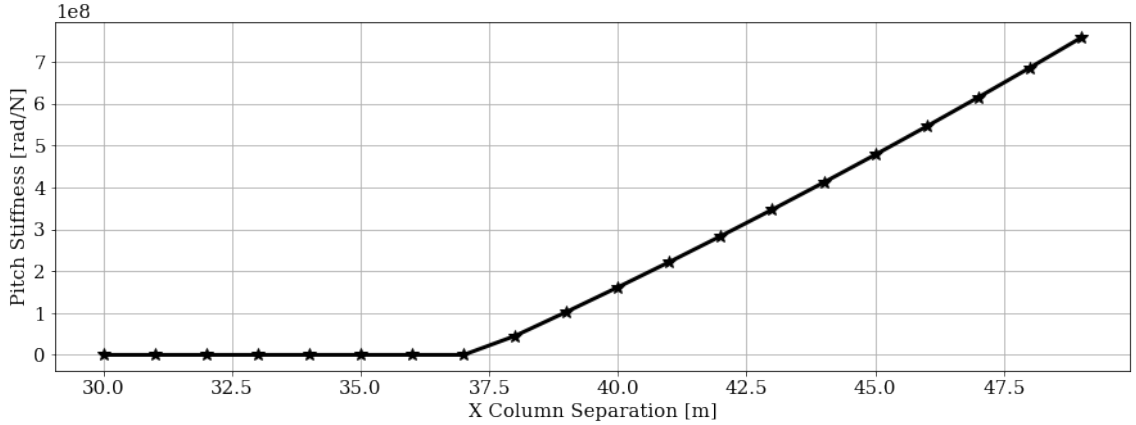

Figure 37: Floater stiffness including correction as a function of x_c

The MPM in pitch as a function of x_c using this correction can be seen in Figure 38. The plot shows that the correction alters the design space in the unstable region. Using this correction allows the SLSQP optimizer to correctly judge an unstable design as being unsuitable.

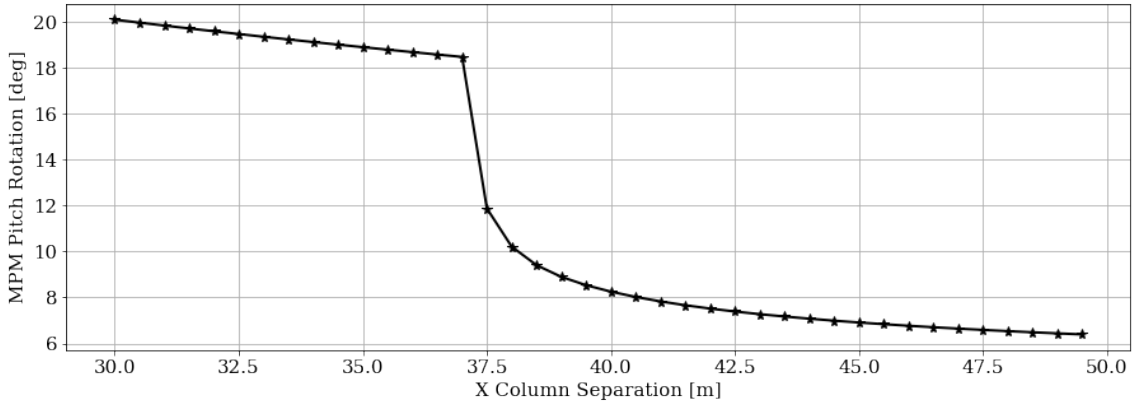

Figure 38: MPM rotation in pitch due to load case 1 using stiffness correction.

The justification for this correction is also applicable to the floater's response in roll under

the second load case. A similar correction is applied however the introduction of the correction is lowered by a factor of 10 (Equation (138)).

$$\begin{array}{ll} \text{For} & K_{4,4} < 1 \times 10^6 \\ K_{4,4} & = 1 \times 10^6 - 5 \times 10^5 \cdot \left(\frac{60 - x_c}{30}\right) \end{array} \tag{138}$$

7.5 Response Spectra

7.5.1 Column Separation

The dynamic response of the floater under the load conditions can be reviewed by following the calculation process outlined in Section 4.3. In this section the response spectra and MPM of a 3 hour time simulation is presented for cuts through the design space under wind and wave excitation.

The first cut through the design space looks at the MPM pitch rotation for a floater of dimensions $y_c = 70m$, $D_c = 12m$ and $D_r = 14m$ under increasing x_c. The calculation process is conducted using the first load case situation, namely with head-on wind and wave loading. The MPM pitch rotations for each design configuration can be seen in Figure 39.

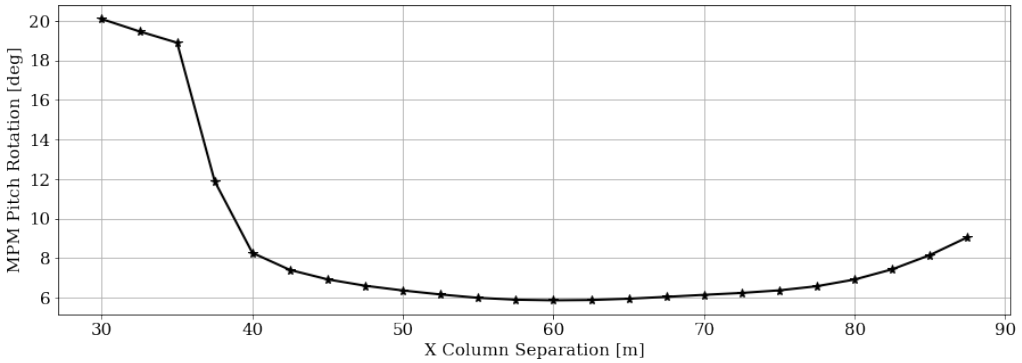

Figure 39: MPM rotation in pitch due to load case 1.

Figure 39 shows three regions of interest. Starting from $x_c = 30m$ it can be seen that the model returns a MPM pitch of approximately 20 °where it is known the restoring force correction is active. This value falls steadily until $x_c = 38m$, after which the MPM pitch begins to decrease. The pitch MPM then remains relatively stable before rising near x_c upper bound.

To better understand the relationships between the x_c variable and the pitch MPM, the response spectrum calculated based on wind and wave loading for a range of x_c values is plotted in Figure 40. What is particularly revealing is the positioning of the eigenfrequency. At low separations the eigenfrequency lies in the aerodynamic excitation range. Then, as the value of x_c increases, the eigenfrequency increases out of this region and into the excitation ranges of the JONSWAP spectrum. As a result, the value of MPM begins to increase as the value of x_c reaches its upper bound.

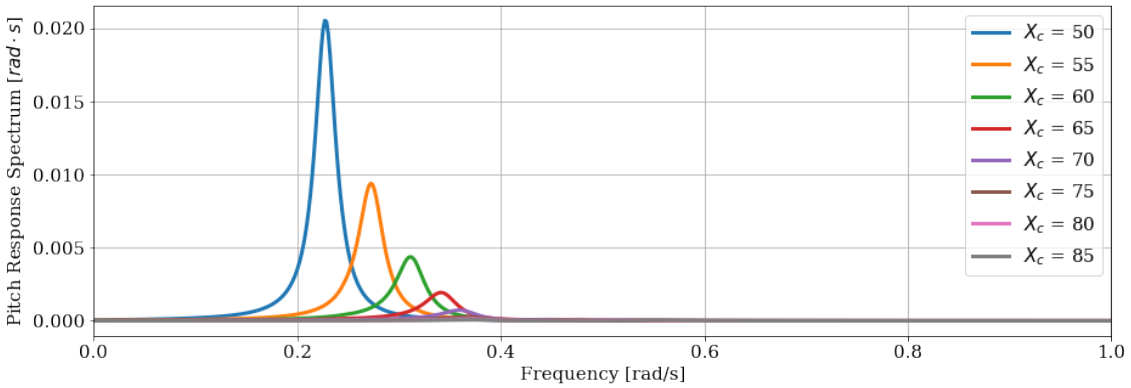

(a) Pitch response spectrum found from aerodynamic loading.

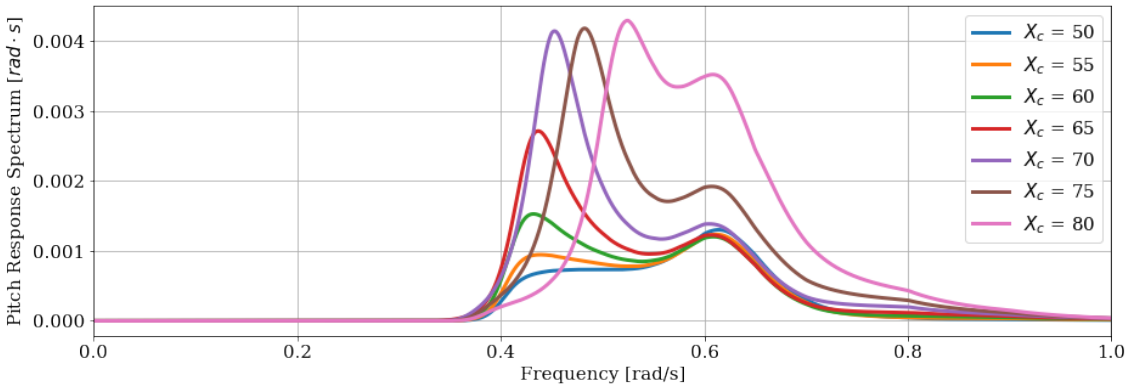

(b) Pitch response spectrum calculated from the JONSWAP spectrum.

Figure 40: Pitch response spectrum under wind and wave loading.

A similar exercise is conducted for the roll MPM and the y_c variable. This is seen in Figure 41 where response spectra corresponding to a number of y_c separations are plotted. It can be seen in the $y_c = 55$ m plot that the roll response is influenced by three eigenfrequencies. This is because the mass distribution of the system in the x-z plane leads to a significant mass coupling term in Ixz. This coupling term is often called the "nose low/high product of inertia" in aerospace engineering. The result of this coupling term is that the sway, roll and yaw eigenfrequencies are present in the roll response.

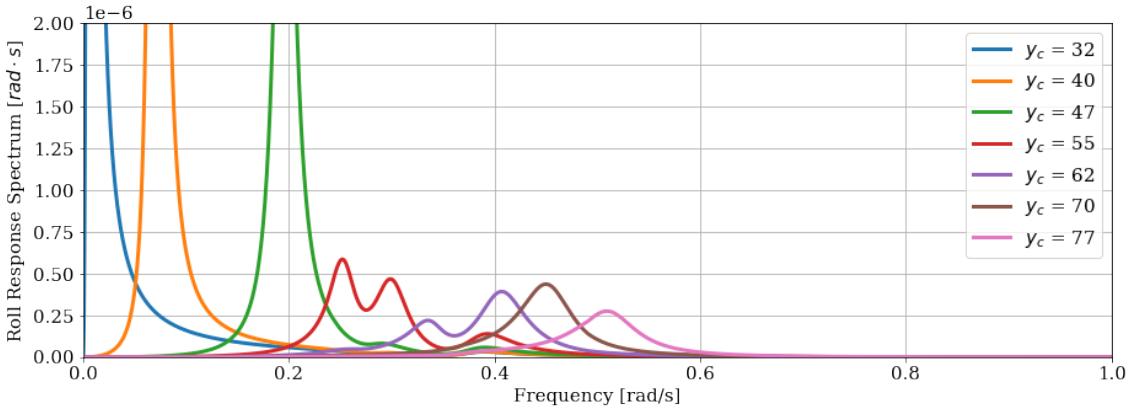

(a) Roll response spectrum found from aerodynamic loading.

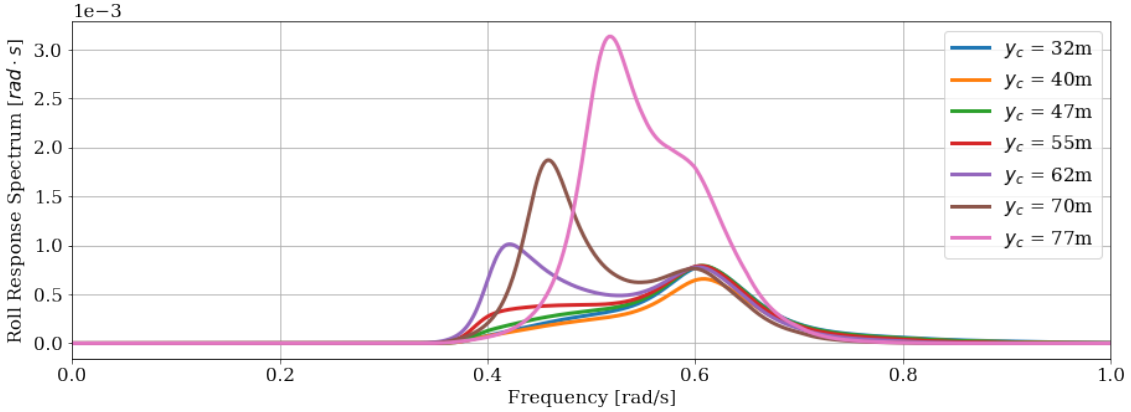

(b) Roll response spectrum calculated from the JONSWAP spectrum.

Figure 41: Pitch response spectrum under wind and wave loading.

A review of the MUFP's eigenfrequencies extracted at corners of the design space is presented in Table 8. A comparison between the first and fourth row can be used as an indication of the relationship between y_c and the sway, roll and yaw eigenfrequencies. It can be seen that the roll eigenfrequency is the most influenced by y_c. Much like the relationship between the pitch eigenfrequency and x_c, the roll eigenfrequency is positioned in the aerodynamic loading frequencies for low values of y_c and in the JONSWAP loading frequencies for high values of y_c.

Table 8: Floater natural frequencies.

Design (x_c, y_c, D_c, D_r)	Natural Frequency [rad/s]					
	Surge	Sway	Heave	Roll	Pitch	Yaw
(40m, 40m, 11m, 12m)	0.264	0.274	0.511	0.098	0.163	0.316
(90m, 90m, 13m, 16m)	0.265	0.265	0.515	0.383	0.426	0.151
(90m, 40m, 13m, 16m)	0.264	0.266	0.511	0.012	0.468	0.178
(40m, 90m, 13m, 16m)	0.265	0.265	0.513	0.462	0.129	0.194

In comparison to this, the sway eigenfrequency remains relatively unchanged at approxi-

mately 0.265 rad/s, while the yaw eigenfrequency passes from 0.316 rad/s to 0.194 rad/s as the value of y_c increases from 40m to 90m. It is therefore known that although the yaw eigenfrequency might fall into the more severe aerodynamic loading frequencies at large column separations, neither eigenfrequencies will dominate the response of the floater.

The consequences of this can be seen by taking the roll MPM as a function of y_c as shown in Figure 42. It can be seen that the plot shows a similar relationship to that shown in Figure 39, at low values of y_c the roll eigenfrequency is positioned in the most severe aerodynamic excitation frequencies. As the separation increases, the floater's roll natural frequency moves out of this region and into the JONSWAP spectrum.

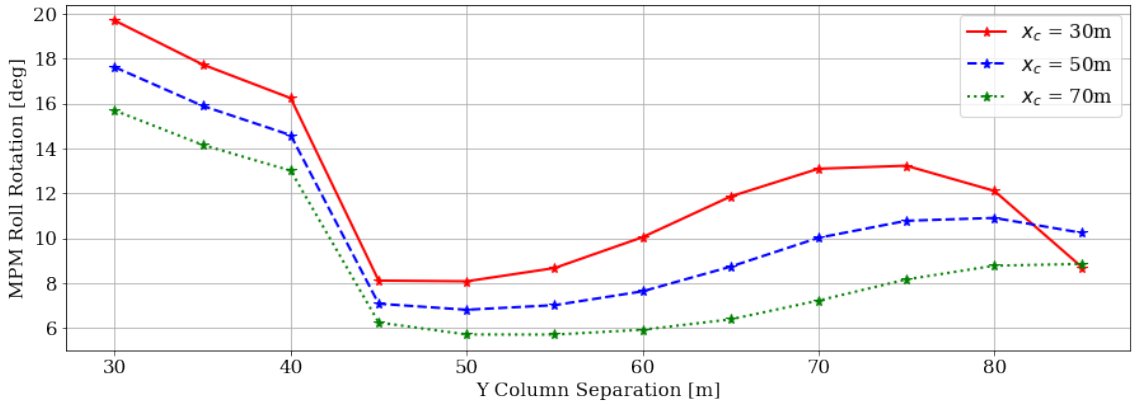

Figure 42: MPM rotation in roll due to load case 2 using the stiffness correction.

7.5.2 Column Diameter and Draft

The influence of column diameter and draft is investigated by calculating the MPM at 9 cuts through the design space. Each cut displays the MPM pitch deflection as a function of x_c and y_c for combinations of column diameter and draft. The results to this process for pitch in the first load case can be seen in Figure 43. In order to improve readability of the plot, any MPM pitch rotation above 20° is capped to 20°.

Each of the plots in Figure 43 shows the same trend as the one dimensional cut discussed previously - large MPM pitch rotations occurring at x_c situated close to the optimization bounds. However, the positioning of the 10° constraint boundary is shown to vary depending on the column diameter and draft.

Using the middle column of the grid as an example, the increase of 2m to the column diameter for a design with 12m draft move this constraint from approximately x_c = 55m and y_c = 55m to x_c = 50m and y_c = 30m. In addition to this, reviewing the bottom row of the grid, it can be seen that a 8 m increase in draft moves the pitch constraint from x_c = 70m and y_c = 65m to x_c = 35 m and y_c = 30m.

It can also be seen that the pitch MPM decreases as a function of y_c. This relationship can be explained by the floater's eigenfrequencies. The pitch RAO, as seen in Figure 35, displays two peaks corresponding with the pitch and surge eigenfrequencies. As the value of y_c increases the total mass of the structure climbs. As a result of this, the surge natural frequency decreases to a region subject to less excitation from JONSWAP spectrum.

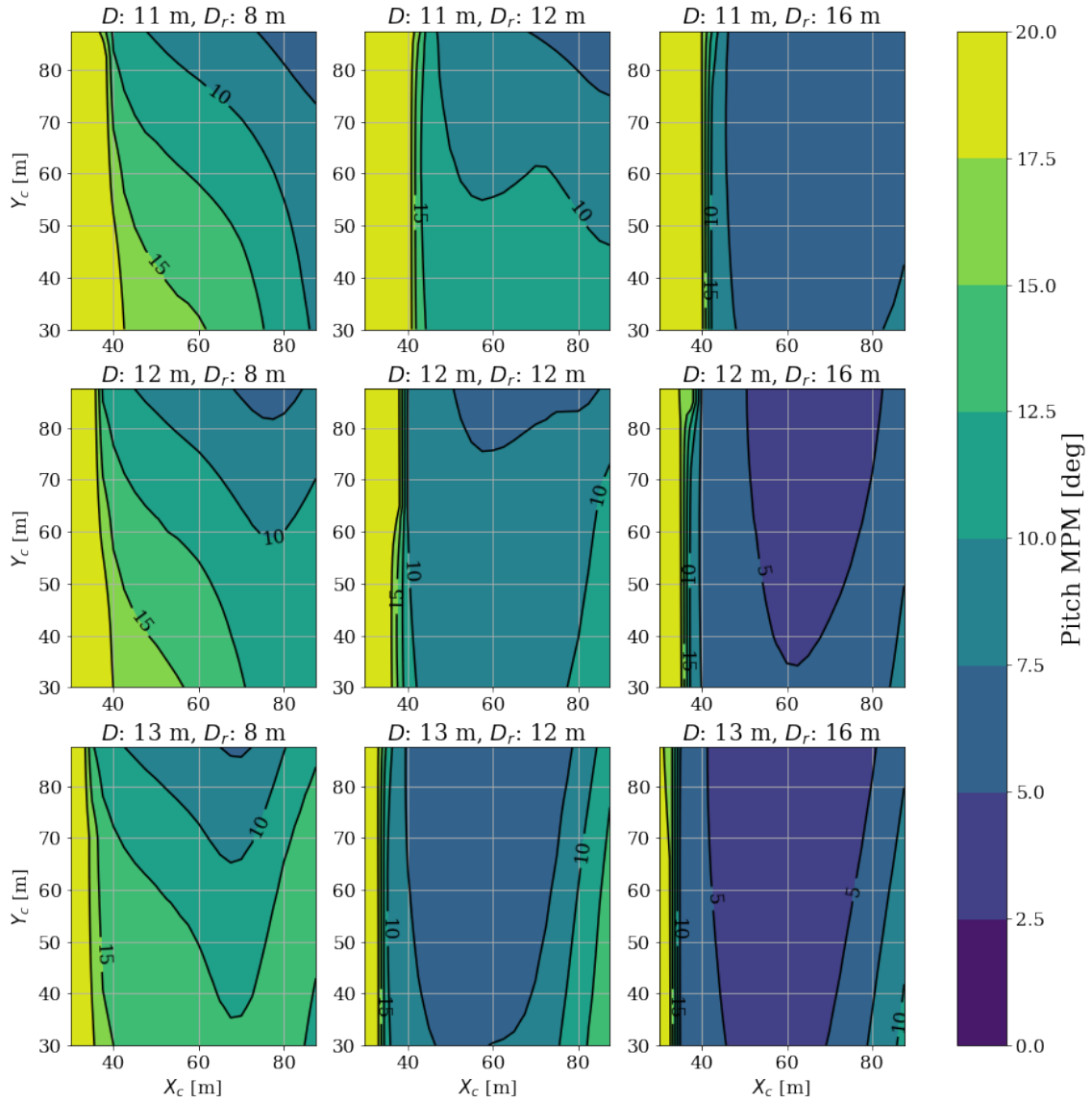

Figure 43: The mpm in pitch under load case 1 for 9 cuts through the design space.

A similar exercise is conducted for roll in the second load case, the results of which can be seen in Figure 44. Figure 44 shows again that low values of y_c places the roll eigenfrequency in low frequency wind excitation, while high values of y_c places the roll eigenfrequency in JONSWAP spectrum.

The plot also reveals a significant influence by x_c. This is clearly exemplified in the middle plot in Figure 44. The reason for x_c being more influential in the roll MPM calculation in comparison to y_c in the pitch MPM calculation is because x_c adds more mass per unit length. This means the system eigenfrequencies are more sensitive to changes to x_c.

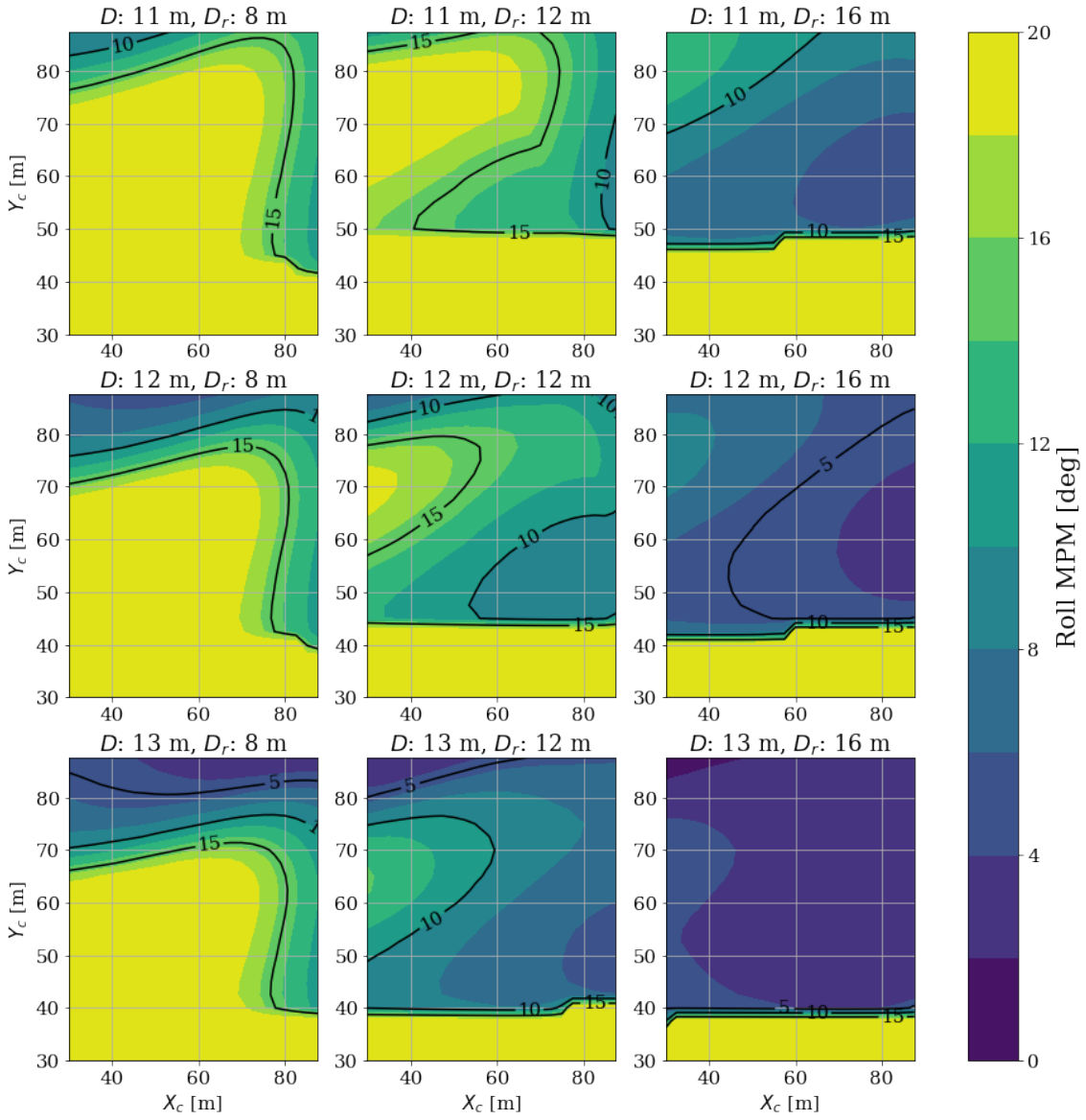

Figure 44: The mpm in roll under load case 1 for 9 cuts through the design space.

8 Optimization

The design space corrections creates a robust interface between the model input variables and the output response statistics. As a result the SciPy SLSQP Minimize function can be utilized to find the design space minimum.

The objective function is defined as shown in Equation (139). The diameter and draft input variables to the optimization were scaled by a factor of 10, and the tolerance criteria for conversion was set at 1. The tolerance for values of x_c and y_c is therefore a meter, while the tolerance for diameter and draft is 0.1 m. It is decided that due to the low fidelity of the model, any accuracy beyond this would have little significance and cause the optimization to run significantly longer.

$$\begin{array}{ll} \text{minimize} & M_{steel}(x_c, y_c, D_c, D_r) \\ \text{with respect to} & x_c \in [30m, 90m], \\ & y_c \in [30m, 90m], \\ & D \in [11m, 13m], \\ & dr \in [8m, 16m], \\ \text{subject to} & MPM_4 < 10^\circ \\ & MPM_5 < 10^\circ \\ & \eta_3 = 0m \end{array} \tag{139}$$

The SciPy SLSQP Minimize function is an external function and it is therefore not possible to access the sources code. The consequences of this is that the optimization is significantly less efficient. The function requires the constraints to return scalar values, because of this a new iteration of the simulation must be run for each constraint evaluation despite a single simulation returning all necessary constraints in matrix form. This immediately doubles the require computational time.

Another inefficiency is the requirement to load a new surrogate model for each iteration of the simulation. In the event the optimizer takes a small step, it is likely the model will remain defined by the same surrogate models as the previous step. In this case, a large computational time saving could be made by passing the saved surrogate model between iterations. The loading of the surrogate model is the most time consuming procedure in the model, removing the requirement to do this for each simulation would therefore reduce the computational time by a further 60%.

8.1 Results

The optimization was run successfully three times requiring computational times ranging from one to approximately four hours. The solution of the optimization can be seen in Table 9. The second and third optimization solution found similar minima while the first solution is found to possess a y_c considerable higher. A review of the optimization constraints found that the solutions satisfied the the MPM rotation constraint in roll and pitch to one decimal place in addition to the static heave constraint.

Table 9: Optimizer solution and run statistics.

Optimization	Run 1	Run 2	Run 3
Starting Point [m]	[90,90,12.0,13.0]	[45,60,11.0,15.0]	[70,45,13.0,12.0]
Iterations	14	3	9
Function Evaluations	86	24	64
Optimum Location [m]	[41.79, 75.45, 12.90, 9.49]	[41.79, 47.55, 11.62, 13.25]	[41.98, 44.44, 11.98, 12.65]
MPM Pitch [°]	10.00	9.33	8.93
MPM Roll [°]	10.00	9.54	10.02
Static Heave [m]	0	0	0
Steel Weight [kg]	4.60×10^6	4.46×10^6	4.44×10^6

To add context to the solution, a review of the design space around each of the solutions is conducted. The MPM rotation in pitch and roll as a function of x_c and y_c around the first solution is plotted in Figures 45a and 45b. It can be seen that the solution lies on the border of the pitch and roll constraints. The optimization was therefore unable to further reduce the input variables. A look at the cuts through the design space presented in Figure 44 reveals that the optimization solution is positioned at a local minima in which the roll natural frequency lies above the JONSWAP spectrum. As a result, this optimization found a minima different from the other solutions.

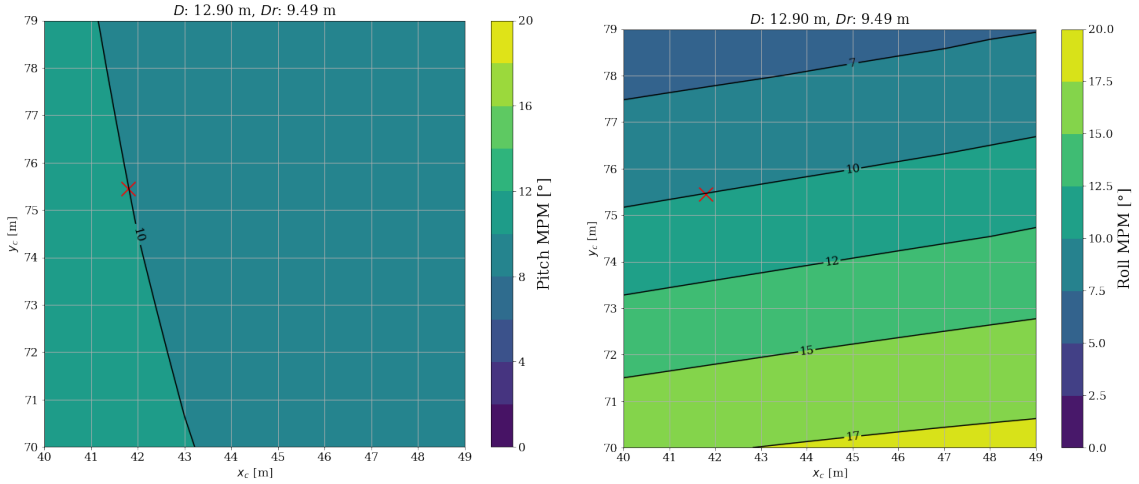

(a) MPM Pitch as a function of x_c and y_c for D_c = 12.9 m and D_r = 9.49 m.

(b) MPM Roll as a function of x_c and y_c for D_c = 12.9 m and D_r = 9.49 m.

Figure 45: MPM Pitch and Roll rotations as a function of x_c and y_c for D_c = 12.9 m and D_r = 9.49 m.

A similar design cut is taken about the second solution. This can be seen in Figures 46a and 46b. In this instance it is clear that although the solution lies in the proximity of both the MPM pitch and roll rotation constraints, the design space reveals that each of the x_c and y_c design variables could be reduced by over a meter. It is also known that the static heave displacement cannot have influenced this solution because the reduction in weight caused by a shortening of the x_c and y_c variables cannot have an adverse effect on the static weight-buoyancy equilibrium.

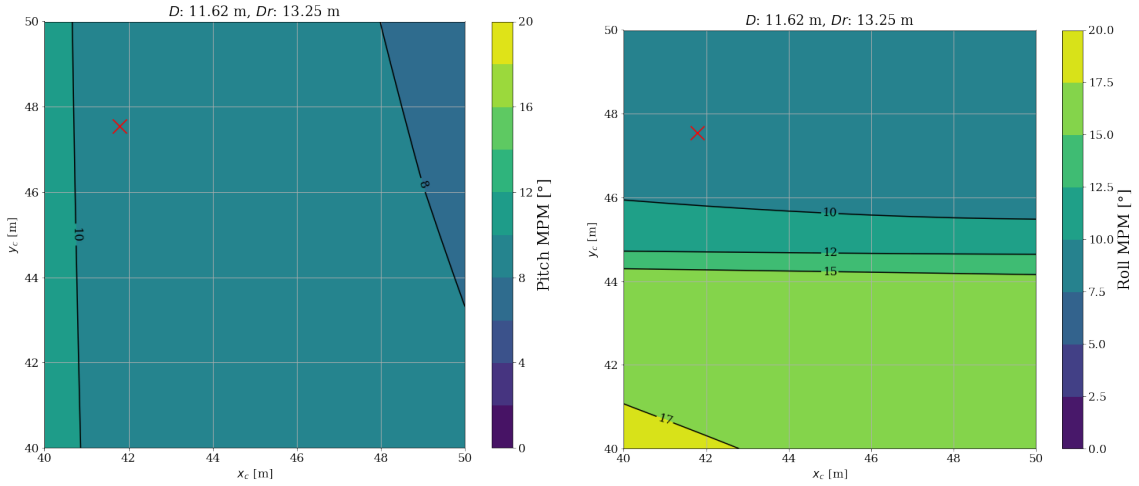

(a) MPM Pitch as a function of x_c and y_c for D = m and Dr = m.

(b) MPM Roll as a function of x_c and y_c for D = m and Dr = m.

Figure 46: MPM Pitch as a function of x_c and y_c for D = m and Dr = m.

The third solution is presented in Figures 47a and 47b. The contour plots reveal that only the roll inequality constraint was active at the solution. A look at Figure 47a reveals the solution is not close to exceeding a MPM pitch rotation of 10°. A review of Figure 47b shows that a unit decrease in either x_c or y_c would result in the roll constraint being exceeded. This solution is found to be the most successful optimization run returning the lowest weight.

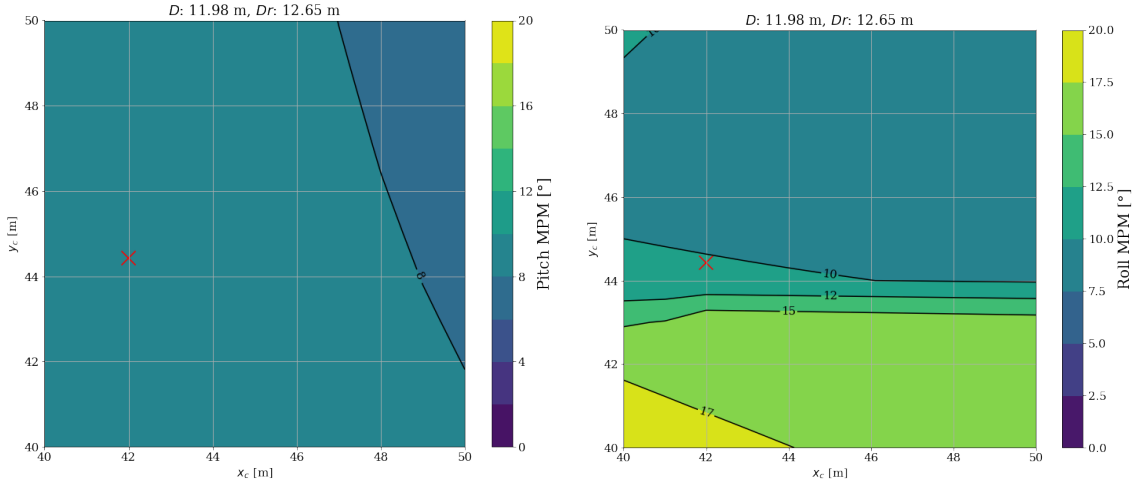

(a) MPM Pitch as a function of x_c and y_c for D = m and Dr = m.

(b) MPM Roll as a function of x_c and y_c for D = m and Dr = m.

Figure 47: MPM Pitch as a function of x_c and y_c for D = m and Dr = m.

9 Analysis

In order to add context to the results and to draw a conclusion on the future feasibility of the MUFP two comparisons are made. Firstly, a review of the scaling properties of the 5 MW and a 10 MW reference turbine is presented. Secondly, the best optimization solution is compared against a single turbine 10 MW semi-submersible.

9.1 Turbine Scaling

As a first point of reference, a review of the NREL 5 MW and DTU 10 MW reference turbine's physical properties is presented in Table 10. The DTU 10 MW reference turbine is itself an upscaled version of the NREL 5 MW reference. The DTU 10 MW turbine is scaled assuming geometrical similarities according to the scaling laws outlined in Equations (2) to (4). The scaling factor used between the turbines is $sf = \sqrt{\frac{10}{5}}$. Due to the method's tendency to overestimate nacelle masses, the nacelle and hub masses were scaled from the Vestas V-164 8MW using $sf = \sqrt{\frac{178.2}{164}}$ corresponding to the differences in rotor diameter [53].

From Table 10 it can be seen that the rated thrust force scales at the same rate as the rated power. The rotor diameter of the 10 MW reference wind turbine is 42% longer than the 5 MW turbine's rotor diameter, while the hub height is 32% higher. A comparison of the turbine massess reveals that the 10 MW turbine offers an improvement in power output per unit weight, contrary to what is expected by the scaling laws in Equations (2) to (4).

Table 10: Comparison of 5 MW and 10 MW reference turbine properties.[38; 53]

Parameter		NREL 5MW	DTU 10 MW	Scaling Factor
Rated Power	MW	5	10	2
Rated Thrust Force	kN	750	1500	2
Rotor Diameter	m	126	178.3	1.42
Hub Height	m	90	119	1.32
Rotor Mass	t	110	229	2.1
Nacelle Mass	t	240	446	1.85
Tower Mass	t	347.5	628.4	1.81
Total Mass	t	697.5	1305.1	1.87

9.2 Concept Comparison

The dimensions and motion characteristics of the semi-submersible are sourced externally. The dimensions of the 10 MW semi-submersible are scaled from the NREL 5MW WindFloat concept [51]. The rough geometry of the semi-submersible can be seen in Figure 48.

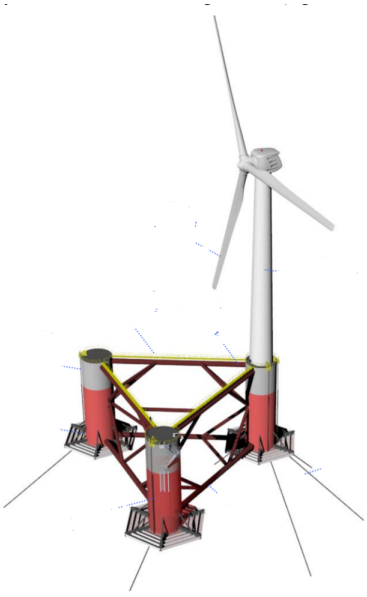

Figure 48: Visualisation of NREL Windfloat [52].

The dimensions of the 10 MW WindFloat can be seen in Table 11 next to the MUFP dimensions found in the optimization. Before any direct comparison between the concepts is made, it is necessary to comment on the methodology used to dimension the WindFloat. The 5 MW WindFloat concept developed by NREL is the product of extensive research including hydrodynamic simulation, structural studies and model test data [52]. As a result, the up-scaled model included in Table 11 will have embedded concessions for ULS, SLS, FLS and ALS requirements whose considerations are far beyond the scope of this report. Therefore any comparisons made are only valid in so far as the frequency domain approach and assumptions made in the report permit.

Table 11: Comparison of floater dimensions.

Floater	Units	WindFloat	MUFP
Draft	[m]	19.15	11.98
Column Diameter	[m]	12.8	12.65
Number of columns	[-]	3	3
Column Separation	[m]	67.75	47.49/44.44
Total Mass	[t]	7708	5624
Displacement	[m3]	7520	5486
COG from SWL	[m]	(0, 0, 4.9)	(0,0,11.96)
COB from SWL	[m]	(0, 0, -9.576)	(0,0,-7.49)
Hub location from SWL	[m]	(27.6, 0, 119)	(-13.99,± 71.05,85)

The reference concept is scaled assuming the floater remains geometrically similar and is then subject to a number of stability checks to ensure the scaled floater remains sea-worthy. Beyond this, the scaled floaters undergo coupled dynamic analysis through a range of operating conditions and sea-states, including decay tests, static wind tests and finally

turbulent wind tests. The turbulent wind tests include uni-directional wind and wave [51].

The test case most comparable to the methodology of this report is the turbulent wind test at rated wind speed. For these tests, the WindFloat concept returned a mean pitch rotation of 10.4° with a sea-state defined by the JONSWAP spectrum with parameters $H_s = 4.1$ m and $T_p = 10.2$ s. It can therefore be said that the WindFloat would not be positioned within the borders of the pitch constraint used in this report.

The draft of the WindFloat is found to be 60% larger than the draft found in the optimization. As a result, the concept's displaced volume and weight are considerably larger than that found in the MUFP optimization. A look at the column separations also reveals the upscaled WindFloat possesses column separations 20m larger than those found in this report.

The optimized MUFP's dimensions and weight are considerably smaller than the WindFloat concept. The reasons for this can be attributed to both the physical properties of the floater and differences in methodology.

Firstly, the MUFP designed in this report uses a hub height of 85m. This is compared to the 119m hub height of the 10 MW turbine used in the WindFloat concept. It was revealed in the comparison between the 5 MW and 10 MW reference turbines that the thrust force generated by two 5 MW turbines is equal to that of a single 10 MW turbine. Therefore the WindFloat would experience a pitching moment due to aerodynamic loading 40% greater than that generated on the MUFP.

Another physical discrepancy in the models is that the WindFloat reference report included the design and consideration of a mooring system [51]. The influence of a mooring system has not been investigated in this report. As a result, the coupling terms and dynamics caused by a fully designed mooring system will not have been captured on the MUFP.

In addition to the physical differences, discrepancies in methodological approach are also present. The WindFloat underwent high fidelity SIMO-RIFLEX-AeroDyn modelling able to simulate the influence of the pitch controller, second order wave loading and non-linear responses. This is in contrast to the frequency domain approach used to optimize the MUFP.

In order to quantify the difference between the methodologies, the dimensions of the WindFloat platform were input into the optimization problem while updating the floater hub height to 119m and the sea state to $H_s = 4.1$ m and $T_p = 10.2$ s. The optimization function calculated a MPM pitch rotation in a 3 hour time series being equal to 2.8°, this is a 7.6° reduction on the mean rotation found during the 10 MW WindFloat turbulent wind tests. This large difference suggests the current optimization function requires further improvements before its results can be deemed reliable. Suggestions for future improvements to the model will be discussed in Section 11.

10 Conclusion

The report summarises the development of a robust data pipeline able to calculate a MUFP's response statistics to environmental loading based on four design variables. The data pipeline is developed with careful consideration to ensure its compatibility with gradient based optimizers. The value of the report is providing a low fidelity tool capable of quickly traversing a design space to land on realistic substructure dimensions.

The optimization was run successfully three times. Of these three optimizations, two optimizations landed in approximately the same region, while the third landed in a less optimal local minimum. It is believed that the two solutions positioned similarly are located at the global minimum. The third optimization solution's design variable combination places the MUFP's roll natural frequency above the JONSWAP spectrum, this was found to create a local minimum away from the global minimum.

A comparison against an up-scaled 10 MW WindFloat found that the optimized MUFP solution had a 27.0% reduction in weight, a 29.9% reduction in column separation and a 37.4 % reduction in draft. The column diameters were found to be approximately equal. Although, physical properties such as the 28.6 % reduction in the turbine's pitching moment arm would benefit the MUFP design, a control calculation was run on the optimization function using the up-scaled 10 MW WindFloat dimensions. The returned response statistics revealed the calculation process outlined in this report was underestimating the floater's motions.

Although large progress has been made in developing the optimization function, the physical significance of its optimum is still limited. The desired outcome of a design optimization is to find a global minimum based on trade-offs between input variables. For this to occur, an accurate estimate of the significance of each variable is necessary. In this report, the column thickness is arbitrarily set at 0.07 m. As a result, any trade-offs in steel mass as a result of unit increases in column diameter or draft lack real significance. In addition to this, the constraints included in the optimization do not account for other limiting factors found in SLS, ALS and FLS design philosophies.

For these reasons this report is unable to quantitatively conclude on the feasibility and cost effectiveness of MUFPs. However, observations found in the development process can be discussed. The advantages of constructing a MUFP is based on the scaling properties of wind energy, platform motion characteristics and operation and maintenance interfaces.

The predicted mass scaling of wind turbines is currently not being followed. A review of a 5 MW and 10 MW reference turbines seen in Table 10 shows the 10 MW reference turbine offers a better rated power to weight ratio. Innovations in wind turbine engineering have allowed turbine components to be built larger, lighter and more efficiently than before. As a result, the assumption that wind turbines remain geometrically similar as they scale is not valid.

The improvements made in wind turbine engineering have made it more cost effective to build fewer larger turbines, rather than many smaller turbines. This is because costs associated with installation, operation and maintenance only scale marginally for increases in turbine capacity, while these costs scale directly with the number of turbines.

However, the law of diminishing returns states that technological advancements will begin

to plateau as a single factor of production is incrementally increased. That is to say that the design improvements made to the rotors, for example, will begin to return smaller improvements per unit resource as time goes on. As it stands, with the rapid development of larger turbines, the industry is not in this phase. However, once improvements do plateau, and developers look to further maximise their yield on renewable energy projects, the MUFPs can offer a viable new approach.

11 Further Work

The workload associated with building a model from zero was found to be significant. There are therefore considerable improvements to be made to improve the detail of the optimization. Maintaining the objective of developing a low fidelity model, the recommendations for further work are as follows.

- Calculate the bracing thicknesses based on its buckling criteria and internal loads.
- Calculate the column thicknesses based on the buckling criteria and pressure.
- Improve the accuracy of the hydrodynamic coefficients by modelling the floater bracing using Morrison elements
- Expand the loading conditions to include a larger range of environmental load combinations.
- Including platform flexibility and fatigue limit state constraints.

A substantial amount of work was conducted in implementing the first suggestion for further work. However because the calculation process was unable to be validated, and because of time constraints, the work was not included in the model. The theory and findings will be presented here for the information of anyone continuing this line of work.

11.1 Internal Force Calculation

The next section outlines the work completed towards implementing a function for the calculation of internal forces acting on the bracing. The calculated internal forces can then be used in the development of more accurate bracing dimensioning function.

11.1.1 Dynamic Loads

Commonly implemented internal load estimates used in platform optimization use design scenarios in which a floaters buoyancy is largely produced by a single pontoon [47]. An estimate for the loads transferred along the bracing can then be derived as a proportion of the floaters buoyancy or weight. This report aimed to include a more accurate calculation of internal forces.

It is known that the internal forces transferred along the structure are dependent on the frequency of excitation. Phenomena such as the frequency dependent split-force loading detailed in Section 5.4 are an example of this.

The calculation process considers each column's motion and hydrodynamic loading individually. By applying Newton's second law, the external forces acting on the column can be equated to the rate of momentum change, as seen in Equations (140) and (141). Any deficit between the two will equal the internal forces acting on the column through the floater's bracing.

$$\sum F = m_c \cdot \ddot{x} \tag{140}$$

$$\sum M = I_c \cdot \ddot{\omega} \tag{141}$$

11.1.2 Column Acceleration

The MUFP's acceleration RAO's are calculated by multiplying the floaters rigid body's displacement RAOs, as seen in Figure 27, by frequency squared, (Equation (142)). The acceleration of a single column can then be mapped against the rigid body acceleration as a function of the floaters dimensions.

$$H_{F\ddot{X}} = -H_{FX} \cdot \omega^2 \tag{142}$$

As an example, the floater's rigid body displacement in pitch will incur both a column displacement in pitch and a significant displacement in heave. A visualisation of this can be seen in Figure 49, where x_c denotes the translation of a single column.

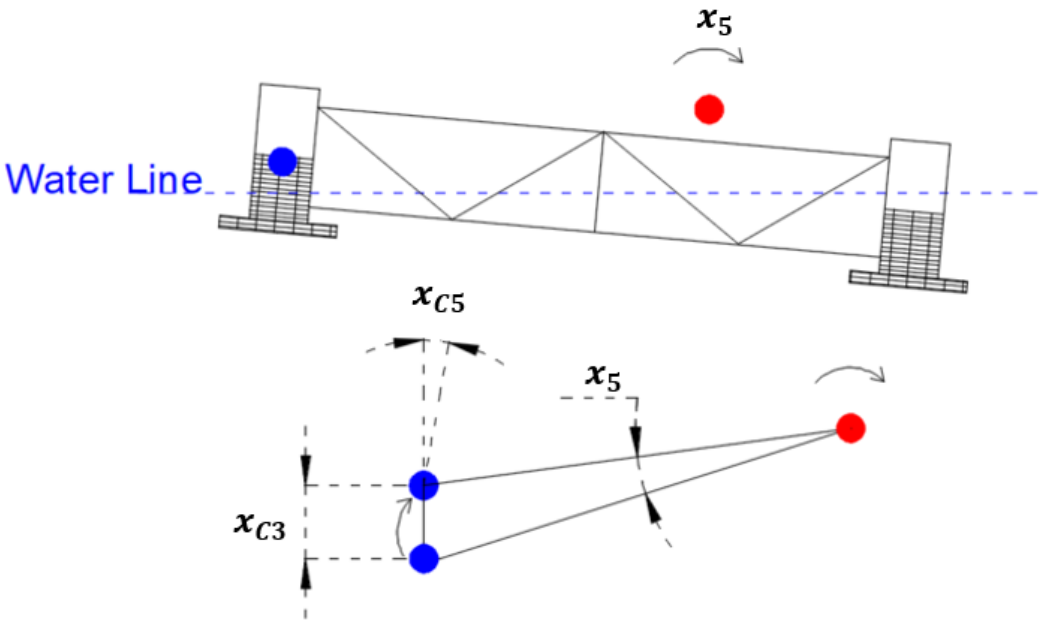

Figure 49: Visualisation of column acceleration being mapped against rigid body acceleration. Blue dot represents column CoM, red dot represents floater CoM.

The mapping of each of the three columns is summarised in Table 12. These equations chart the rigid body motions to that of a single column. A small angles assumption is taken reducing $L \cdot \sin x$ to $L \cdot x$ and setting $L \cdot \cos x = 0$.

Table 12: Column motions as a function of the rigid body motions.

	Front Column	**Left Column**	**Right Column**
$x_{c1} =$	x_1	$x_1 - L_{lcy} \cdot x_6$	$x_1 + L_{rcy} \cdot x_6$
$x_{c2} =$	$x_2 - L_{fcx} \cdot x_6$	$x_2 + L_{lcx} \cdot x_6$	$x_2 + L_{rcx} \cdot x_6$
$x_{c3} =$	$x_3 + L_{fcx} \cdot x_5$	$x_3 + L_{lcx} \cdot x_4 - L_{lcy} \cdot x_5$	$x_3 - L \cdot x_4 - L_{rcy} \cdot x_5$
$x_{c4} =$	x_4	x_4	x_4
$x_{c5} =$	x_5	x_5	x_5
$x_{c6} =$	x_6	x_6	x_6

The transformed column acceleration RAOs in surge, heave and pitch can be seen in Figure 50. It can be seen that the magnitude of surge and pitch acceleration remain unchanged. While, more notably, the heave response now holds peaks at the surge, heave and pitch natural frequencies. This is a results of the mass coupling between surge and pitch and in mapping between rigid body pitch and column heave.

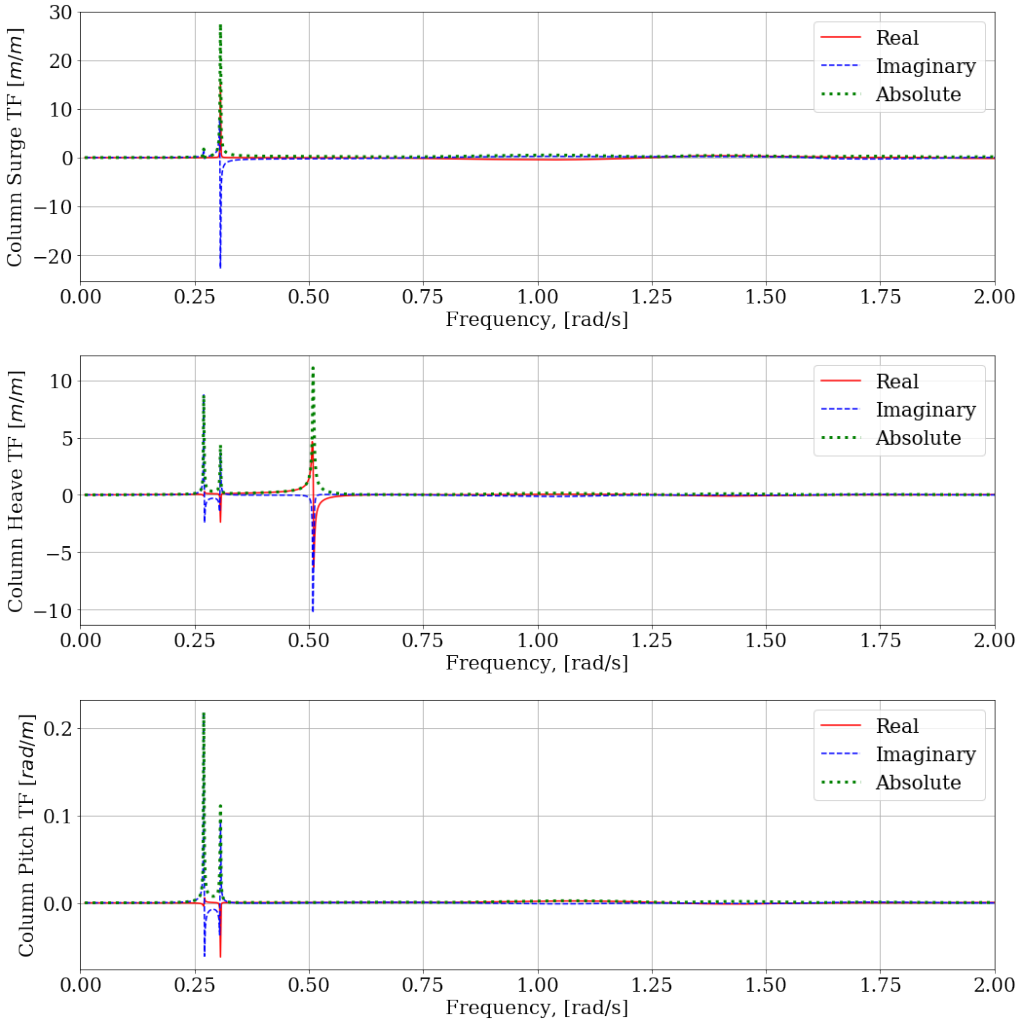

Figure 50: Front column acceleration RAOs in surge, heave and pitch.

Each columns acceleration as a function of frequency is now known for all degrees of freedom. The forces acting on each of the columns will now be reviewed.

11.1.3 Column Forces

The forces acting on each column can be categorised as gravitational loads, buoyancy loads hydrostatic stiffness, added mass, potential damping, wave excitation and internal loading. In this model it is assumed the gravitational loads and the buoyancy loads cancel out. The sum of the forces acting on a column can therefore be equated to the remaining terms, as seen in Equation (143).

$$\sum F = \underbrace{-A\ddot{x} - B\dot{x} + F_{exc}}_{\text{Included in panel pressure}} - Cx + F_{int} \tag{143}$$

The hydrodynamic terms in Equation (143) can found from the potential flow solver HydroD, the theory of which is explained in Section 4.1. The HydroD output contains the pressure force acting on each panel, p_k, the normal vector out of the fluid $\overrightarrow{\boldsymbol{n}_k}$, along with the panel's area and coordinates. The pressure values include the influence of added mass, damping and excitation forces on the system.

The potential flow force acting on the floater can be computed using Equation (144). Where r_k is the moment arm to the column centre of mass in the x, y and z direction. The pressure panels acting on a single column can be found by filtering the panels based on their coordinate location. The sum of forces acting on a column can therefore be seen as shown in Equation (145).

$$\boldsymbol{F}_p = -A\ddot{x} - B\dot{x} + F_{exc} = \begin{bmatrix} \Sigma_{k=1}^{k=N} p_k \overrightarrow{\boldsymbol{n}_k} A_k \\ \Sigma_{k=1}^{k=N} p_k \boldsymbol{r}_k \times \overrightarrow{\boldsymbol{n}_k} A_k \end{bmatrix} \tag{144}$$

$$\sum F = \boldsymbol{F}_p - Cx + F_{int} \tag{145}$$

An extract showing the forces acting on the x_c = 60 m, y_c = 80m, D_c = 12m and Dr = 14m floater's front column is shown in Figure 51. It can be seen that the forces acting on a single column also possess the frequency dependent forces caused by the relationship between wave length and column separation. The loading in y is found to be minuscule and can be explained through machine error, while the loading in heave shows a similar trend to that of the rigid body heave motion.

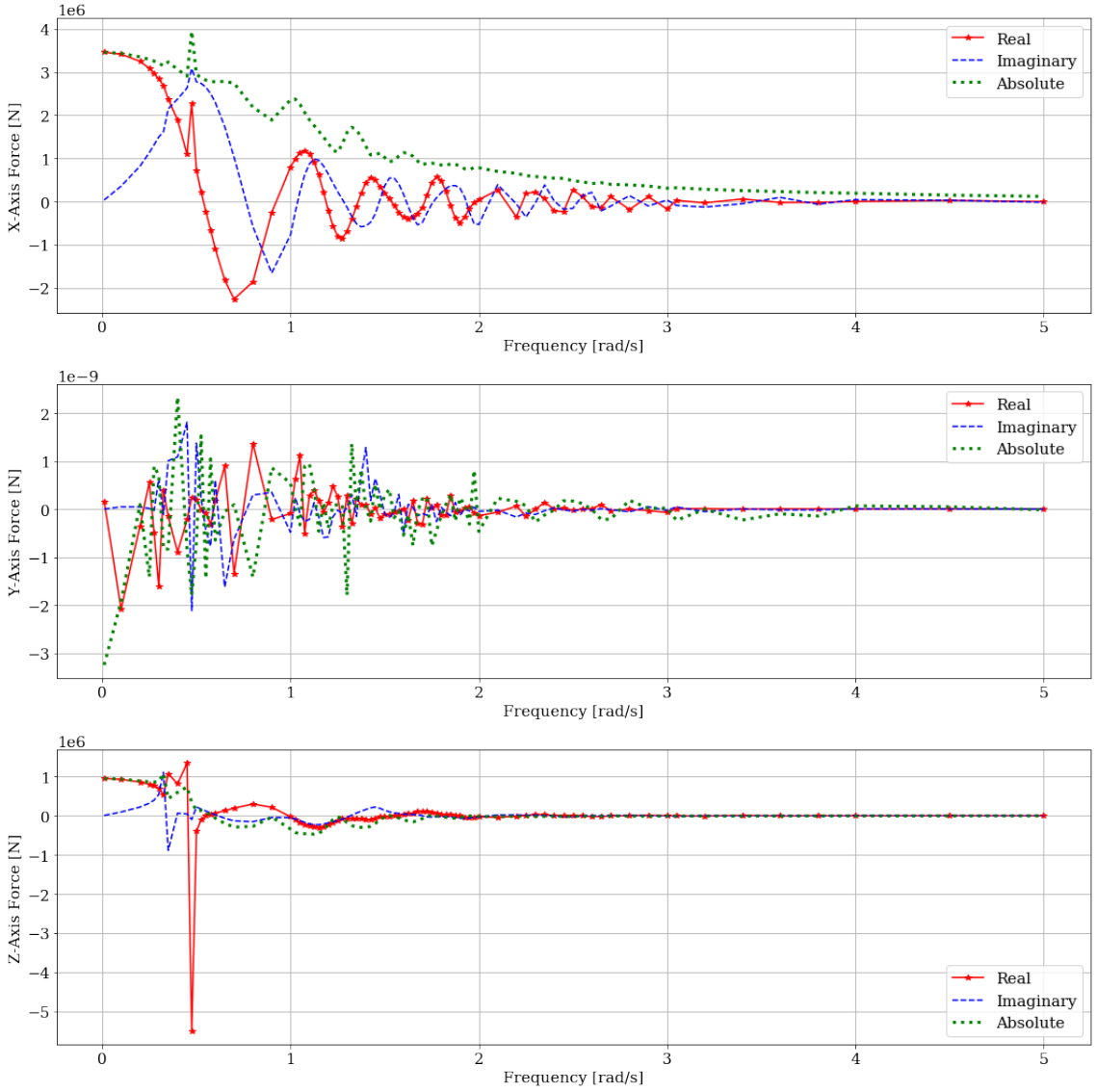

Figure 51: Force acting on front column calculated using potential flow theory.

11.1.4 Internal Force Transfer Functions

With the known mass, moment of inertia, column acceleration and external loading, Equation (146) can be derived from Equation (140) and Equation (145) giving the internal forces action on the column through the bracing.

$$F_{int} = \boldsymbol{M}\ddot{x} - \boldsymbol{F}_p + \boldsymbol{C}x \tag{146}$$

11.1.5 Validation Test Case

The validation of the calculation process follows two parts. The first is a data scraping validation and the second is a full internal load validation.

The first validation is conducted by running a HydroD simulation with a fixed model. The omission of floater movements, and therefore radiation data, means that the panel pressure does not include the influence of added mass or damping. Therefore the panel pressure calculated in the HydroD simulation will consist entirely of the wave excitation forces. The validation method consists of reconstructing the wave excitation functions directly from the extracted panel pressures.

The reconstructed wave excitation function is calculated using Equation (144). The results of this calculation procedure can be seen in Figure 52 for the 0 degree wave heading. It can be seen that strong agreement is shown between the two methods. A small discrepancy can be seen in the sway plot which leads to a more noticeable error in the roll plot. The reason for this difference is not known, however considering the magnitude of both of these excitations, it can be concluded that the influence on the system will be negligible. The same validation process using the 90 degree head angle can be found in Figure 57 in Section 11.1.5. From this plot it is clear that the error does not carry into other head angles.

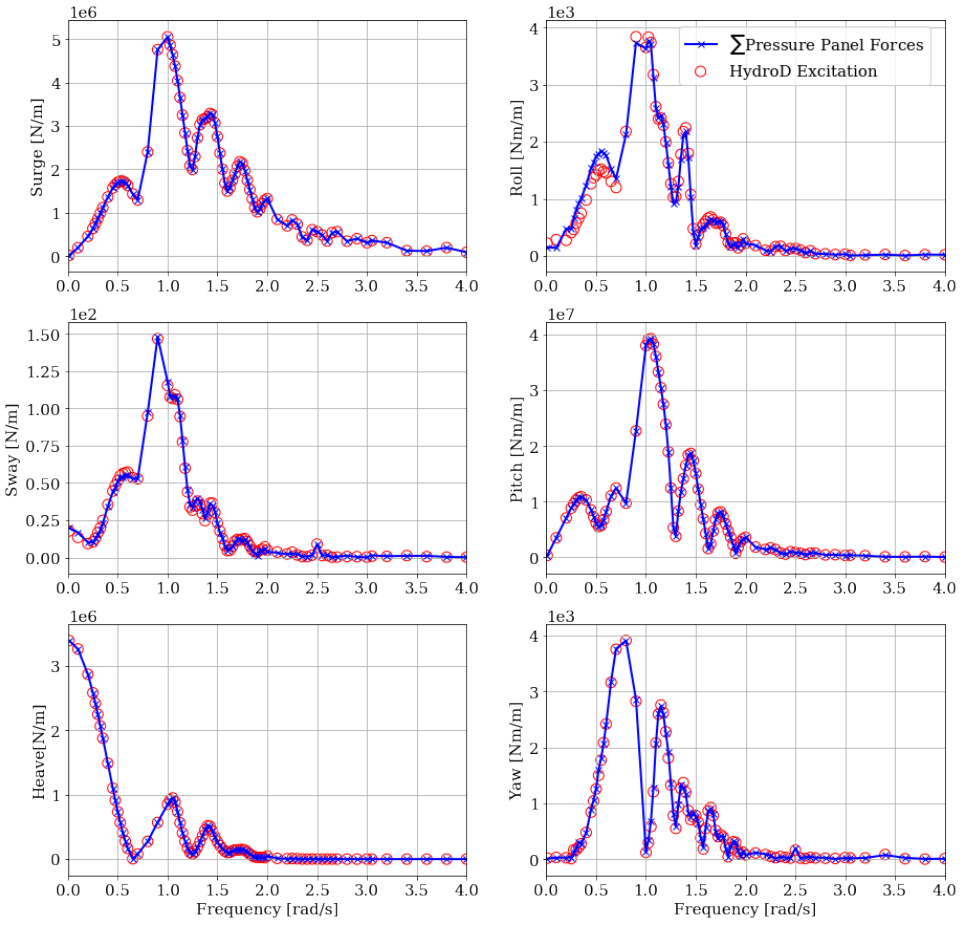

Figure 52: A comparison between the HydroD wave excitation function and the reconstructed wave excitation function using the HydroD panel pressure. Data uses a 0 degree wave heading.

The second validation process is aimed at the internal load calculation process. In order to validate this, a test case is run in HydroD including sectional loads. Sectional loads are a feature of HydroD which returns the internal loads of a structure. The feature calculates this by integrating load and mass forces up to an input cut plane.

The validation procedure requires a mass distribution model in order to calculate the inertial forces acting on the system. To save time constructing this, a simplified model is used. The validation model replaces the mass of the tower and turbines with additional ballasting while also changing the density of the ballasting the density of steel. The mass distribution used for the validation model is summarised in Table 13.

Table 13: Mass distribution of internal force validation test case

Component	x	y	z	Mass [kg]
Front Ballast	0	0.00	-13.80	1.07×10^6
Back Left Ballast	-60	-40.00	-13.80	1.07×10^6
Back Right Ballast	-60	40.00	-13.80	1.07×10^6
Front Column	0	0.00	-0.50	5.80×10^5
Back Left Column	-60	-40.00	-0.50	5.80×10^5
Back Right Column	-60	40.00	-0.50	5.80×10^5
Front Heave Plate	0	0.00	-13.00	3.81×10^5
Back Left Heave Plate	-60	-40.00	-13.00	3.81×10^5
Back Right Heave Plate	-60	40.00	-13.00	3.81×10^5
Left RNA	-60	-71.05	85.00	0.00
Right RNA	-60	71.05	85.00	0.00
Left Tower	-60	-53.50	36.96	0.00
Right Tower	-60	53.50	36.96	0.00

The mass distribution is built up in GeniE. This is done by modelling all three columns rather than reflecting it down the x-axis as done previously and by adding density and thickness to each of the model plates. Using this method the finite element model export contains both the geometric data for the panel model and the mass distribution necessary to calculate the internal loading.

The finite element model is imported into HydroD and analysed similarly to the previous simulations. The differences in the simulations are that the mass distribution data is now imported directly from GeniE rather than input as a point mass. A visualisation of each of the cut planes, as provided by HydroD, is shown in Figure 53. By allocating the sectional loads accordingly, the inertial and potential loading on each of the three columns is isolated. It is important to bear in mind that the results to the simulation are calculated about the HydroD global coordinate system, in this case this is positioned at the SWL in-line with the floaters centre of gravity.

The calculation process detailed in Section 11.1.1 is then followed for the front column. The inertial terms of the Equation (146) required the construction of a mass matrix for an individual column. For the floater as a whole, the assumption that $I << M \cdot r^2$ holds true is valid, however because of the the reduction in distance and scale, the continuous mass distribution needs to be considered. The mass matrix is built using analytical formulae.

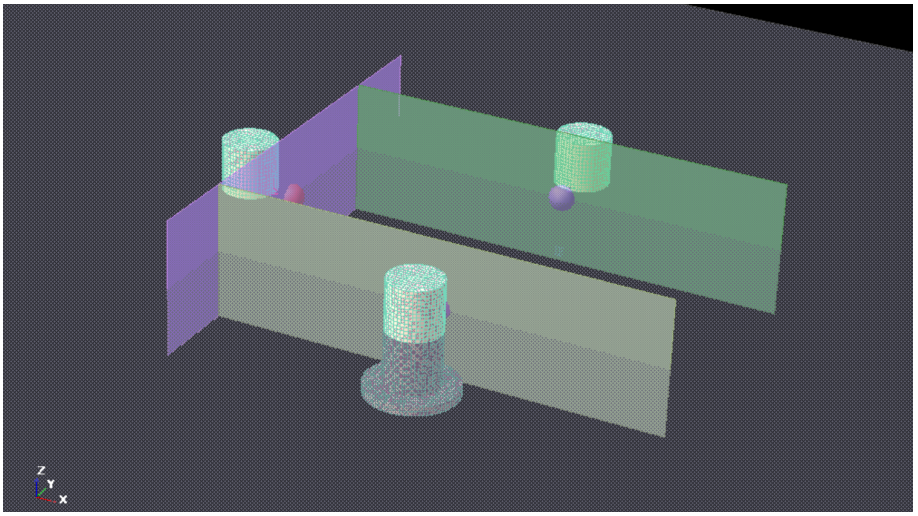

Figure 53: Visualisation of sectional load positioning taken from HydroD.

The column is deconstructed into 6 individual parts. The column top, the column, the heave top, the heave column, the ballast and the heave bottom. A visualisation of this can be seen in Figure 54. The moments of inertia for each component can calculated using the formulae shown in Table 14. The component's contribution to the columns moment of inertia about the SWL can then be calculated by applying the parallel axis theorem and summing the results. The mass matrix also holds two coupling terms as a result of the coordinate system being taken about the SWL rather than the column centre of gravity. Therefore the $\boldsymbol{M}_{0,4}$ and $\boldsymbol{M}_{1,3}$ and their mirror terms are equal to $-m_c \cdot z_g$ and $m_c \cdot z_g$ respectively.

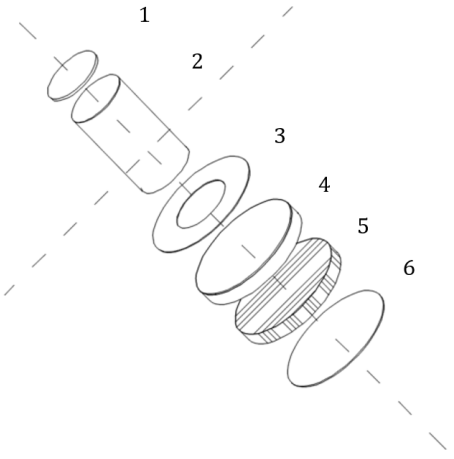

Figure 54: A single column broken down into individual plate components.

Table 14: Analytical formulae for component moment of inertia.

Component	Izz $[kg/m^2]$	Ixx/Iyy $[kg/m^2]$
1	$\frac{1}{2}m_i r_c^2$	$\frac{1}{4}m_i r_c^2$
2	$m_i r_c^2$	$\frac{m_i}{12}(3 \cdot (r_c^2 + r_h^2) + h^2)$
3	$\frac{1}{2}m_i(r_c^2 + r_h^2)$	$\frac{1}{2}m_i(r_c^2 + r_h^2)$
4	$m_i r_h^2$	$\frac{m_i}{12}(3 \cdot (r_c^2 + r_h^2) + h^2)$
5	$\frac{1}{2}m_i r_h^2$	$\frac{1}{4}m_i r_c^2$
6	$\frac{1}{2}m_i r_h^2$	$\frac{1}{4}m_i r_c^2$

The stiffness term in the calculation process also needs a constructed stiffness matrix. This is calculated by assigning the floaters artificial stiffness in surge, sway and yaw to the column in full, while the columns hydrostatic stiffness in heave, roll and pitch are calculated as shown in Section 5.3.2 using the geometry and displaced water of a single column.

These calculations leave the internal force component of Equation (146) as the only unknown variable. The transfer function of the internal force and moments acting along the axis are calculated and shown in Figure 55. The y-axis limits have been shrunk to better capture agreement outside of the natural frequency response. It can be seen that the two calculations return similar trends and magnitudes however also show regions of disagreement.

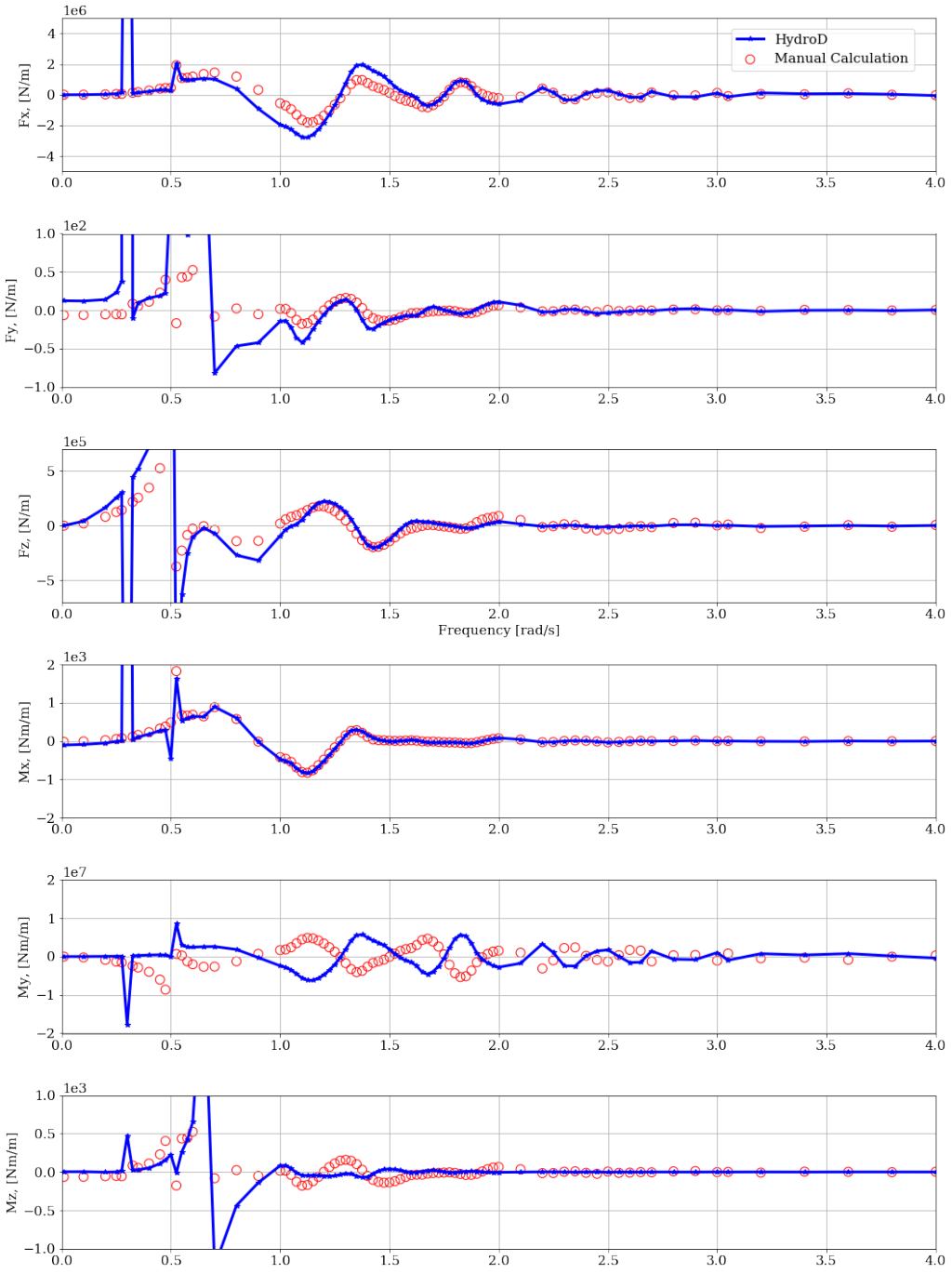

Figure 55: Comparison of the internal forces acting on the front column as calculated manually and by HydroD sectional loads. The real component is plotted.

In order to troubleshoot the reason for this difference, the individual components of Equation (146) are plotted against the sectional load output of HydroD. These plots can be seen in Figure 56. What is striking in the first three force plots is that the HydroD sectional load forces follow the panel pressure forces very closely showing little influence of either the inertial loads or the stiffness. However this is not always the case. An interesting region to

examine is the 0 rad/s to 1.5 rad/s region of the F_z plots. Here the sectional loads start by following the inertial load component of the equation, before transitioning to the stiffness component before settling on the pressure panel forces. In the low frequency region where the inertial loads dominate, the pressure panels and stiffness components are equal and opposite, it is therefore expected that the inertial loads is the only internal force acting.

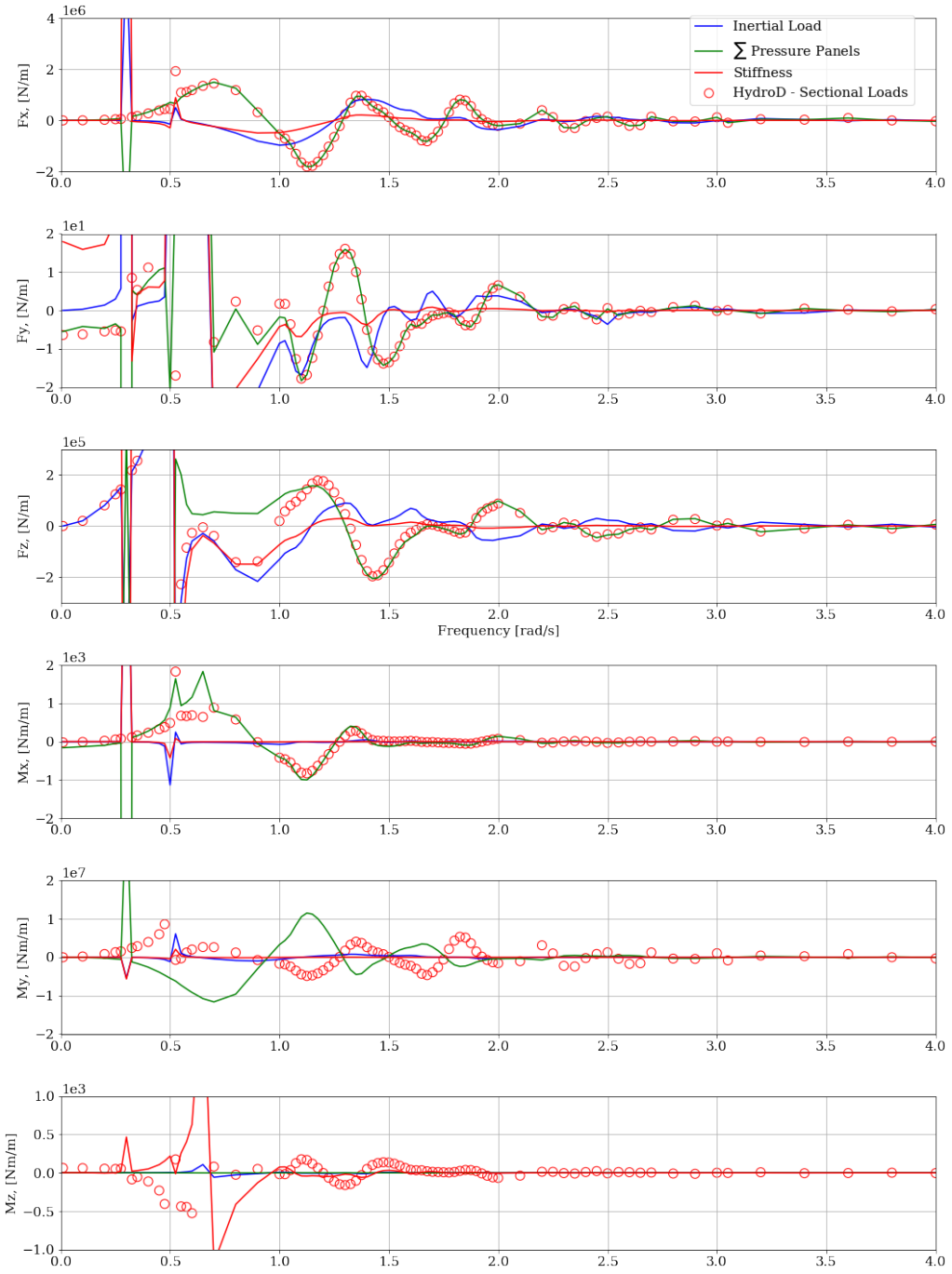

Figure 56: HydroD sectional loads plotted alongside the individual terms in Equation (146)

The graphs displayed corresponds to the front column under head-on loading conditions. The five other plots showing the other columns under the same loading conditions along with all three columns under side-on wave loading can also be found in Section 11.1.5.

Unfortunately, this function was not validated in this report. The theory has been included in hope it will help future students endeavouring to undertake a similar task.

References

[1] Colin Walsh, Wind Europe(2019). *Offshore wind in Europe, Key trends and statistics 2019*. Retrieved from: https://windeurope.org/wp-content/uploads/files/about-wind/statistics/WindEurope-Annual-Offshore-Statistics-2019.pdf

[2] IRENA (2019), Future of wind: Deployment, investment, technology, grid integration and socio-economic aspects (A Global Energy Transformation paper), International Renewable Energy Agency, Abu Dhabi

[3] IRENA (2020), Renewable Power Generation Costs in 2019, International Renewable Energy Agency, Abu Dhabi.

[4] Unknown, Pelagic power. Retrieved from: http://www.pelagicpower.no/about.html, Date Accessed 10/11/2020

[5] Unknown, Hexicon A.B. Retrieved from: https://www.hexicon.eu/hexicon/, Date Accessed: 10/11/2020

[6] Unknown, EnBW Energie. Retrieved From: https://www.enbw.com/renewable-energy/wind-energy/our-offshore-wind-farms/nezzy2-floating-wind-turbine/, Date Accessed: 10/11/2020

[7] M. Hansen (2015). *Aerodynamics of Wind Turbines, Third Edition*

[8] J. Jonkman et al, (2009). *Definition of a 5-MW Reference Wind Turbine for Offshore System Development* NREL, Golden, CO.

[9] E. Bachynski (2020). *Aerodynamics for Wind Turbines*. Course: Integrated Dynamic Analysis of Wind Turbines, NTNU

[10] E. Smith H. Klick (2007) *Explaining NIMBY Opposition to Wind Power*

[11] A. Arapogianni and A. Genachte (EWEA) (2013) *Deep water: The next step for offshore wind energy.* Retrieved from: www.ewea.org/report/deep-water EWEA

[12] Unknown, *Hywind Scotland* Equinor. Retrieved from: https://www.equinor.com/content/dam/statoil/documents/newsroom-additional-documents/news-attachments/brochure-hywind-a4.pdf , Date Accessed: 13/11/2020

[13] Unknown, *WindFloat Atlantic* https://www.edp.com/en/innovation/windfloat, Date Accessed:09/08/2021

[14] Adnan Durakovic (2021) *World's Largest Floating Wind Farm Takes Final Shape* Retrieved from: https://www.offshorewind.biz/2021/07/05/worlds-largest-floating-wind-farm-takes-final-shape/ Date Accessed: 09/08/2021

[15] P. Connolly et al, (2019) *Comparison of pilot-scale floating offshore wind farms with shared moorings* Ocean Engineering.

[16] M. Chow (2019) *Mooring System Design for Wind Farm In Very Deep Water* Masters Thesis, NTNU.

[17] K. Ma, Y. Luo, T. Kwan et al (2019) *Mooring System Engineering for Offshore Structures*

[18] Unknown, *Concept*, Retrieved from: https://www.eolink.fr/en/concept. Date Accessed: 15/11/2020

[19] Unkown, EnBW Energie *Nezzy*^{2} Retrieved from: https://www.enbw.com/renewable-energy/wind-energy/our-offshore-wind-farms/nezzy2-floating-wind-turbine/. Date Accessed: 15/11/2020

[20] N. Barltrop (1993).*Multiple unit floating offshore wind farm (MUFOW).* Wind Engineering,17(4):183–188,

[21] N. Papandroulakis (2017) *Aquaculture perspective of multi-use sites in the open ocean: The untapped potential for marine resources in the anthropocene* The EU-Project "TROPOS"

[22] P. Mayorga et al. (2018) *Study of a hybrid renewable energy platform: W2Power* Proceedings of the ASME 2018 37th International Conference on Ocean, Offshore and Arctic Engineering

[23] Unknown, Vestas *Multirotor fact sheet* Retrieved from:https://www.vestas.com/ /media/files/multirotor fact sheet.pdf, Date Accessed: 08/12/2020

[24] M. van der Laan et al. (2019) *Power curve and wake analyses of the Vestas multi-rotor demonstrator* Wind Energy Science

[25] P. Jamieson et al. (2012) *Multi-Rotors; A Solution to 20 MW and Beyond?* Energy Procedia

[26] Y. Bae et al. (2014) *Coupled dynamic analysis of multiple wind turbines on a large single floater* Ocean Engineering

[27] I. Udoh et al. (2020) *Optimizing floating offshore multi-wind-turbine design: A parametricstudy on tower inclination and column spacing* Proceedings of the Annual Offshore Technology Conference

[28] J. Ayotte (2015) *Dynamic positioning of a semi-submersible, multi-turbine wind power platform*

[29] Unknown, EnerOcean *W2Power* Retrieved from:https://enerocean.com/w2power/, Date Accessed: 08/12/2020

[30] D McPhee (2018) *Swedes hope to get troubled Dounreay floating wind project 'back on track'* Retrieved from: https://www.energyvoice.com/renewables-energy-transition/185940/swedish-firm-still-hopeful-of-getting-troubled-dounreay-floating-wind-project-back-on-track/. Accessed on: 08/12/2020

[31] Unknown, WunderHexicon. *MULTIPLAT2* Retrieved from: https://www.wunderhexicon.es/projectsMULTIPLAT2 ,Accessed on: 08/12/2020

[32] Unknown, *Dounreay Trì Floating Wind Demonstration Project* Retrieved from:http://www.marine.gov.scot/ml/dounreay-tri-floating-wind-demonstration-project , Accessed on: 08/12/2020

[33] A. Lee (2019) *Shell and CoensHexicon deal to build floating wind off Korea* Retrived from: https://www.rechargenews.com/wind/shell-and-coenshexicon-deal-to-build-floating-wind-off-korea/2-1-628976 , Accessed on: 09/12/2020

[34] A. Siegfriedsen, EnBW (2020) *Research project : Nezzy^2 floating offshore wind turbine* Retrieved from: https://www.enbw.com/media/erneuerbare-energien/images/press-release_enbw-and-aerodyn-test-model-for-floating-wind-turbines.pdf Accessed on: 09/12/2020

[35] Unknown, EnBW *Research project : Nezzy^2 floating offshore wind turbine* Retrieved from: https://www.enbw.com/renewable-energy/wind-energy/our-offshore-wind-farms/nezzy2-floating-wind-turbine/ Accessed on: 09/12/2020

[36] O. Faltinsen (1993) *Sea Loads on Ships and Offshore Structures*

[37] H. Baltscheffsky, Hexicon A.B (2020) *Floating windfarms: Yield estimation software from Hexicon validated by DNV GL* Retrieved from: https://news.cision.com/hexicon-ab/r/floating-windfarms–yield-estimation-software-from-hexicon-validated-by-dnv-gl,c3027742 Accessed on:12/12/2020

[38] J. Jonkman et al, (2009). *Definition of a 5-MW Reference Wind Turbine for Offshore System Development* NREL, Golden, CO.

[39] DNV GL (2018) *Floating wind turbine structures (DNVGL-ST-0119)* Available at: https://rules.dnvgl.com/docs/pdf/DNVGL/ST/2018-07/DNVGL-ST-0119.pdf. Accessed on: 09/08/2021.

[40] Naess, A., Moan, T. (2012). Random Environmental Processes. In Stochastic Dynamics of Marine Structures (pp. 191-208). Cambridge: Cambridge University Press. doi:10.1017/CBO9781139021364.009

[41] Naess, A., Moan, T. (2012). *Response Spectrum. In Stochastic Dynamics of Marine Structures (pp. 209-232).* Cambridge: Cambridge University Press. doi:10.1017/CBO9781139021364.010

[42] Naess, A., Moan, T. (2012). Response Statistics. In Stochastic Dynamics of Marine Structures (pp. 233-251). Cambridge: Cambridge University Press. doi:10.1017/CBO9781139021364.011

[43] Kraft D (1988) A software package for sequential quadratic programming. Tech. Rep. DFVLR-FB 88-28, DLR German Aerospace Center — Institute for Flight Mechanics, Koln, Germany.

[44] Joaquim R. R. A. Martins & A Ning (2020) *Engineering Design Optimization.*

[45] Lin Li, Zhen Gao, Torgeir Moan (2013). *JOINT ENVIRONMENTAL DATA AT FIVE EUROPEAN OFFSHORE SITES FOR DESIGN OF COMBINED WIND AND WAVE ENERGY DEVICES.* Proceedings of the ASME 2013 32nd International Conference on Ocean, Offshore and Arctic Engineering

[46] C. Tracy *Parametric design of floating wind turbines.* Master's thesis, Massachusetts Institute of Technology

[47] M. Karimi at al. (2017) *A multi-objective design optimization approach for floating offshore wind turbine support structures* Journal of Ocean Engineering and Marine Energy

[48] E. Bachynski (2014), *Design and Dynamic Analysis of Tension Leg Platform Wind Turbines*, NTNU

[49] D.Roddier et al. (2011) Modeling of an oscillating water column on the floating foundation WindFloat, Proceedings of the International Conference on Offshore Mechanics and Arctic Engineering

[50] W. Xue (2016) *Design, numerical modelling and analysis of a spar floater supporting the DTU 10MW wind turbine*, Master's Thesis NTNU

[51] T. Islam (2016) *Design, Numerical Modeling and Analysis of a Semi-submersible Floater Supporting the DTU 10MW wind turbine*, Master's Thesis NTNU

[52] D. Roddier, C. Cermelli A. Weinstein (2016) *WINDFLOAT: A FLOATING FOUNDATION FOR OFFSHORE WIND TURBINES PART I: DESIGN BASIS AND QUALIFICATION PROCESS*, Proceedings of the ASME 2009 28th International Conference on Ocean, Offshore and Arctic Engineering

[53] C Bak et al. *Description of the DTU 10 MW reference wind turbine.* In: DTU Wind Energy Report-I-0092 (2013).

.1 Internal Force Validation Plots

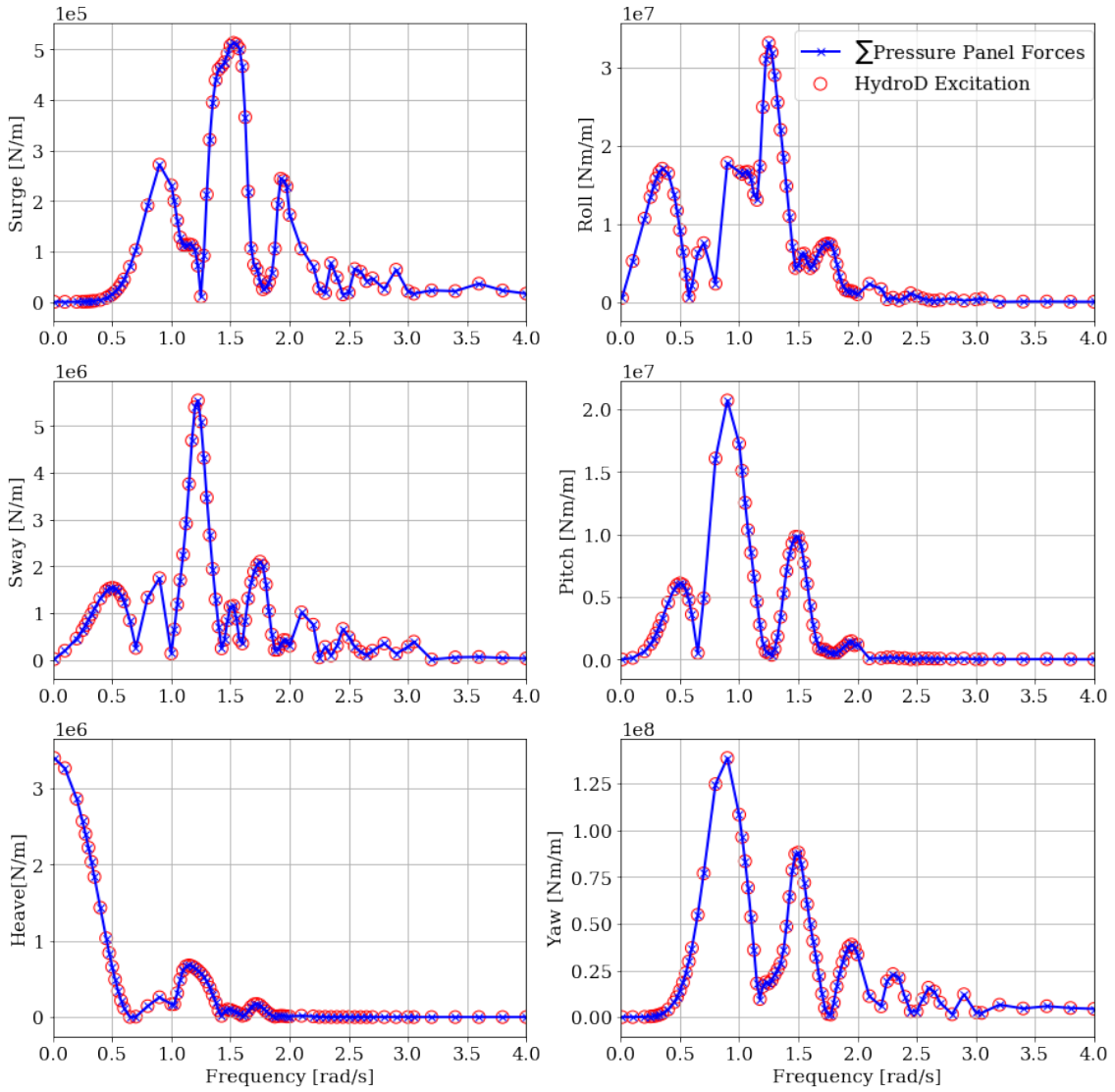

Figure 57: A comparison between the HydroD wave excitation function and the reconstructed wave excitation function using the HydroD panel pressure. Data uses a 90 degree wave heading.

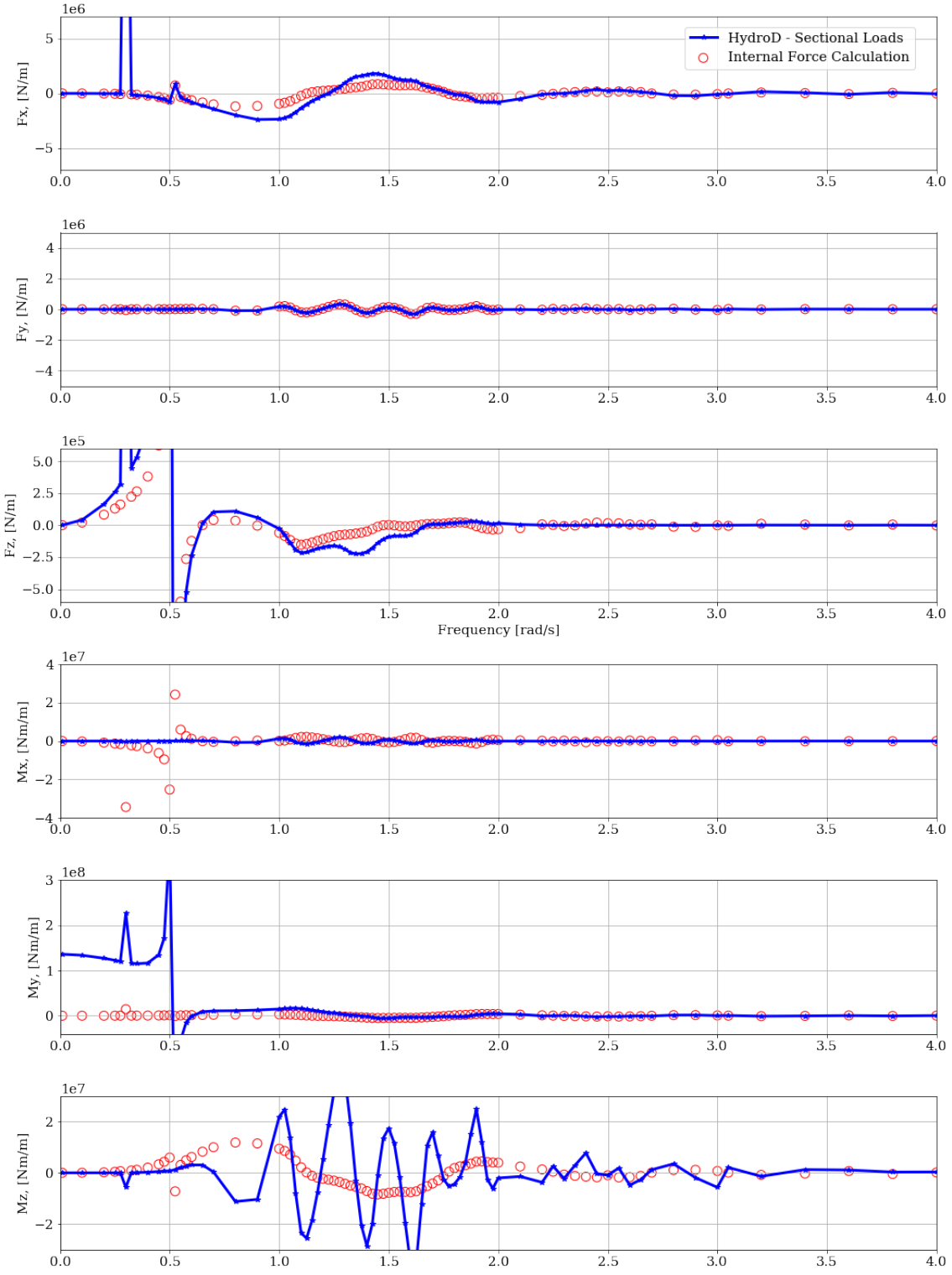

Figure 58: Internal Force Comparison: Left Column under 0 degree loading.

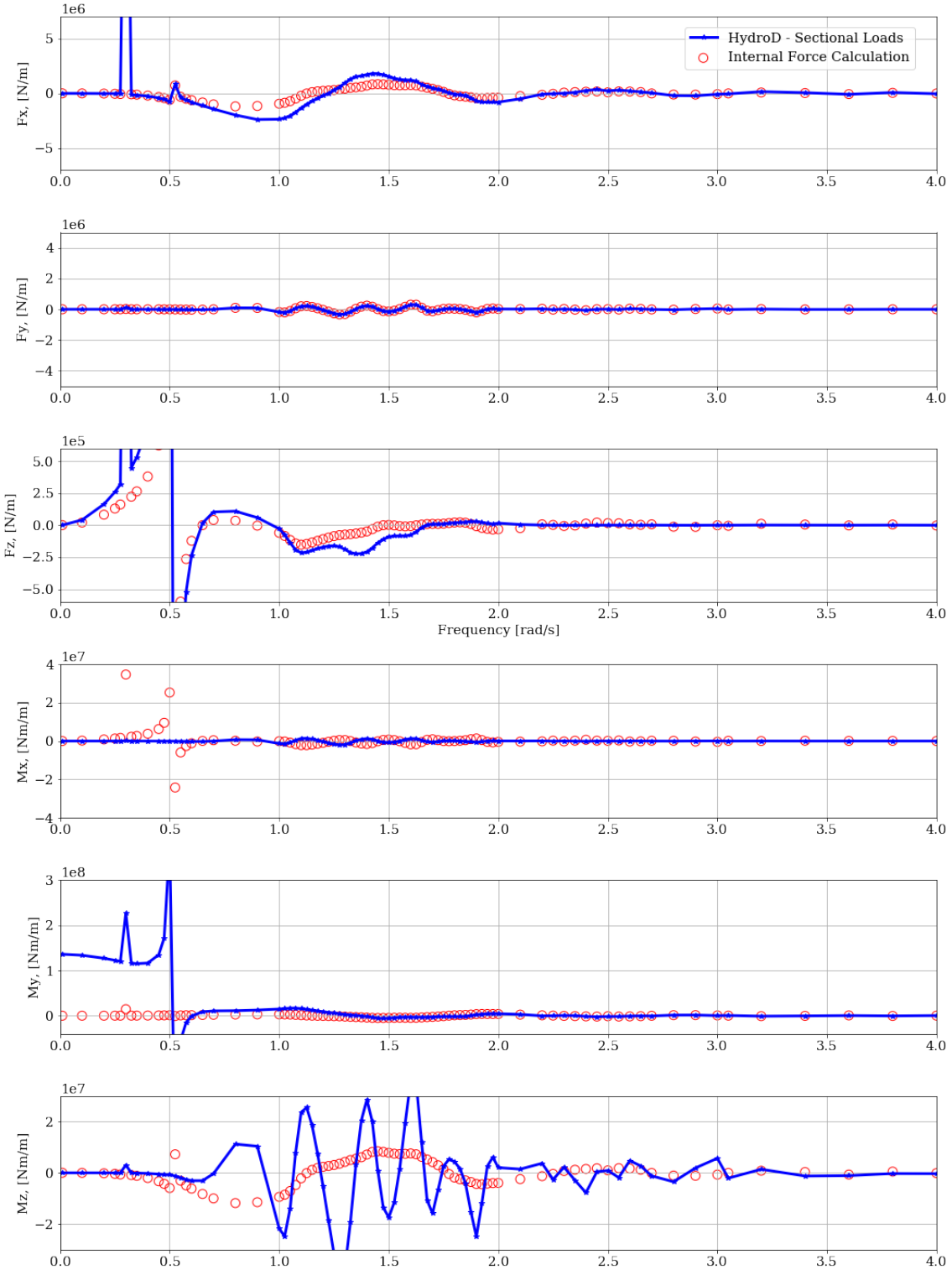

Figure 59: Internal Force Comparison: Right Column under 0 degree loading.

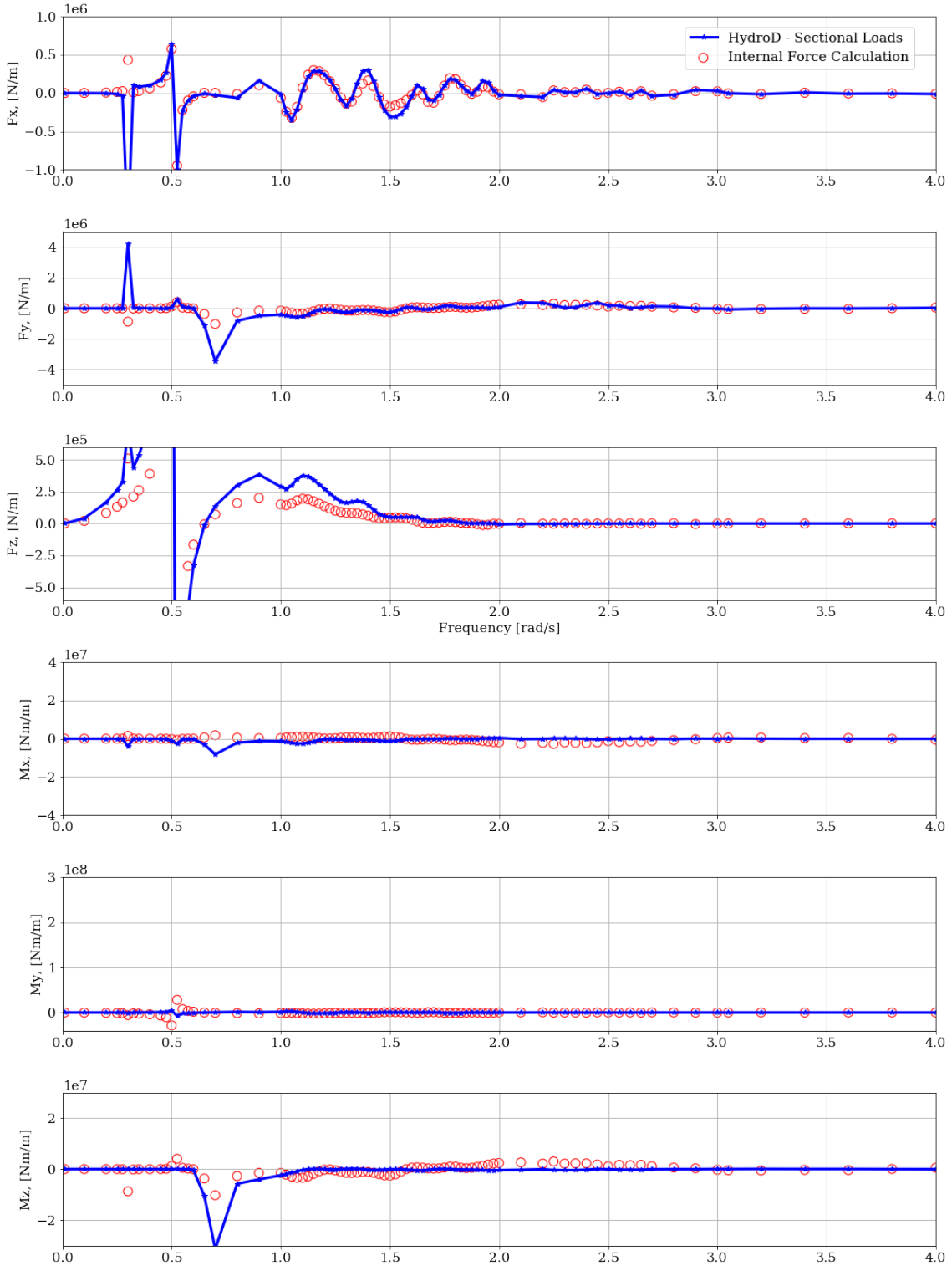

Figure 60: Internal Force Comparison: Front Column under 90 degree loading.

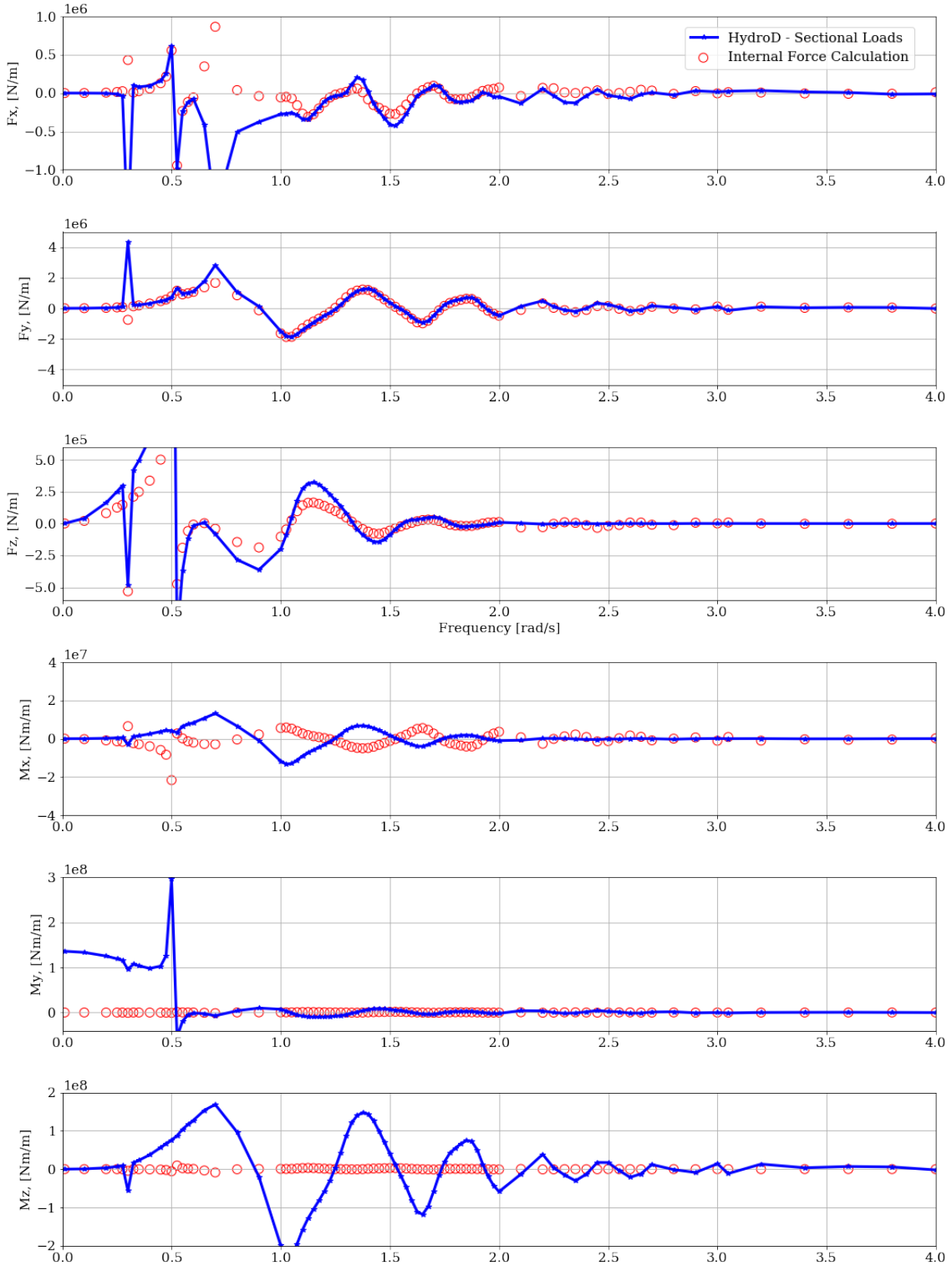

Figure 61: Internal Force Comparison: Left Column under 90 degree loading.

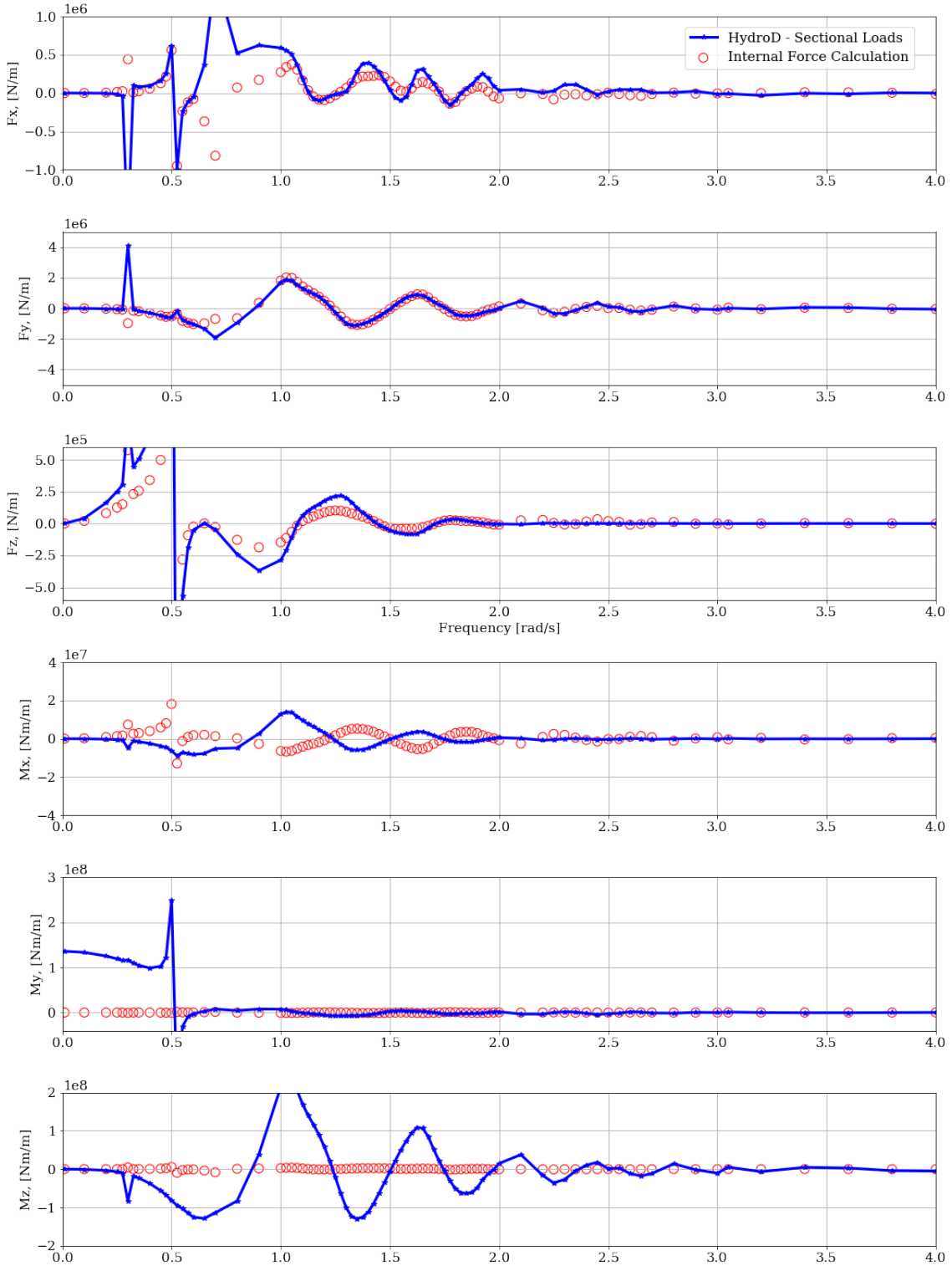

Figure 62: Internal Force Comparison: Right Column under 90 degree loading.